A Cryogenic Molecular Ion-Neutral Hybrid Trap

Inauguraldissertation

zur

Erlangung der Würde eines Doktors der Philosophie

vorgelegt der

Philosophisch-Naturwissenschaftlichen Fakultät

der Universität Basel

von

Claudio von Planta

aus Allschwil (BL)

Basel, 2020

Genehmigt von der Philosophisch-Naturwissenschaftlichen Fakultät
auf Antrag von

Prof. Dr. Stefan Willitsch und Dr. Brianna Heazlewood

Basel, den 23.06.2020

Prof. Dr. Martin Spiess
Dekan

Abstract

A hybrid trap was developed to confine neutral molecules and molecular ions. We demonstrated the long-term trapping of Stark-decelerated OH radicals in the $X\ ^2\Pi_{3/2}\ (v = 0,\ J = 3/2,\ M_J = 3/2,\ f)$ state in a permanent magnetic trap. The trap environment was cryogenically cooled to a temperature of 17 K in order to efficiently suppress black-body-radiation-induced pumping of the molecules out of trappable quantum states and collisions with residual background gas molecules which usually limit the trap lifetimes. The cold molecules were kept confined on timescales approaching minutes, an improvement of up to two orders of magnitude compared to room-temperature experiments, at translational temperatures on the order of 25 mK.

A cryogenic ion trap was built and laser cooled Ca^+ ions were confined. This ion trap can be used to confine sympathetically cooled molecular ions such as N_2^+ or H_2O^+.

Furthermore, a mechanism to superimpose both trap centers by moving the permanent magnets from the magnetic trap over the ion trap was developed. Both traps were characterized and their functionality was proven. The challenges of laser-cooling in the strong magnetic field gradients were discussed.

The present results pave the way for investigations of cold collisions and reactions with very small reaction rates between molecular ions and neutral molecules, for new avenues for the production of ultracold molecules via sympathetic cooling and for the realization of new forms of hybrid matter with co-trapped atoms or ions.

Contents

Chapter 1

Introduction

The field of cold molecules and cold molecular ions offers a large variety of applications. With translational temperatures in the regime of millikelvin (mK) and thus low velocities (on the order of tens of m/s as compared to hundreds of m/s at room temperature), they experience a low Doppler-shift. Therefore, they give rise to very interesting systems for spectroscopic precision measurements [1, 2, 3]. Cold molecules and ions which are spatially confined in traps lay the foundations for quantum information processing and quantum-logic-assisted spectroscopy [4, 5, 6]. The main motivation for this thesis is the study of inelastic and reactive molecular collisions at ultralow collision energies [7, 8, 9, 10, 11]. At such low temperatures (below 1 mK), the collisions between the particles are characterized by few partial waves and reaction cross sections are very sensitive to the collision energy. Thus, they can be used to probe potential energy surfaces of a system and to study the dynamics of collisions. Quantum mechanical effects such as tunneling and reactive resonances become dominant factors in the chemical reactivity and can be studied in detail [12, 13, 14, 15, 16].

The methods for the production of cold molecules reach from methods such as Stark deceleration [17, 18] and Zeeman deceleration [19, 20] over velocity selection [21], sympathetic cooling with laser-cooled atomic species and more recently even direct laser cooling [22, 23]. However, the latter is only applicable for a limited amount of molecular species that offer closed optical cycles. Cold molecules were also formed indirectly by photoassociation [24] and magnetic association via Feshbach resonances [25].

Collisions of neutral molecules and molecular ions have been studied e.g. by combining a molecular beam with a linear Paul trap to study the reaction [26]

$$H_2O + N_2H^+ \rightarrow N_2 + H_3O^+.$$

The work in this thesis, however, focuses on the development of a novel type of hybrid trap, combining a linear Paul trap to confine sympathetically cooled molecular ions with a magnetic trap to confine neutral molecules. This setup will allow for the first time the simultaneous trapping of neutral molecules and molecular ions in the mK regime. The advantage of a hybrid trap system over, e.g., a Stark decelerator combined with an ion trap [27] lies in the interaction times, since the neutral molecules and molecular ions can be overlapped on the order of up to a minute. Even if a decelerator could be operated at 250 Hz, which would be the upper limit in our setup, the hybrid trap experiment would offer about a factor of 25 more collisions over measurement time. Details on this estimation are shown in sec. 4.3.

Chapter 2 presents the development of the cryogenic magnetic trap, enabling trapping times on the order of tens of seconds. Internally cold molecules were produced via dissociation of water molecules using a pulsed valve [28] together with a pinhole discharge assembly [29]. The OH molecule (hydroxyl) has already been Stark decelerated and trapped in a magnetic trap [30]. Combined with simple detection by laser-induced fluorescence (LIF), it is a suitable neutral molecule for the development of such a system. The hydroxyl radical is also an important molecule in atmospheric chemistry as it acts as a key oxidant in the lower atmosphere [31]. It has been detected in the interstellar medium and is considered to be an important reactant in the chemistry in the gas phase of interstellar clouds [32, 33, 34].

As the trap depths of magnetic traps are relatively shallow (< 200 mK for OH in the $X\ ^2\Pi_{3/2}\ (v = 0,\ J = 3/2,\ M_J = 3/2,\ f)$ state), OH molecules were translationally cooled using a 124 stage Stark decelerator [18] in order to load them into the magnetic trap built from two PrFeB magnets with a remanence of 1.64 T under cryogenic conditions. As the dipolar molecules can be pumped into non-trappable states by the interaction with ambient black-body radiation (BBR) [35], the trap assembly was cooled down to temperatures around 17 K and shielded from room-temperature BBR. This allowed to increase the trapping times by a factor of $\approx$57 to around 40 s as compared to about 0.7 s under room temperature. The details are presented in sec. 2.7.2.

The second part of the hybrid trap, the cryogenic ion trap, is presented in chapter 3. A thin wire ion trap was designed, developed and used to trap Ca^+ ions. A beam of Ca atoms was provided by resistive heating of a tube filled with Ca powder and the Ca atoms were ionized via resonance-enhanced multiphoton ionization (REMPI)

[36, 37].

Chapter 4 presents the combination of both traps which will allow for hybrid trapping of neutral molecules and molecular ions. The holder of the permanent magnets from the magnetic trap can be moved, using a cryogenic motor. This allows the trap centers of the ion trap and the magnetic trap to be superimposed. The challenge of laser-cooling in the strong magnetic field gradients from the magnetic trap is discussed by developing a trajectory simulation including a laser-cooling model via the 8-level optical Bloch equations (OBE) in the Ca^+ system [38, 39].

The reaction rates of molecular ion-neutral molecule reactions are planned to be extracted by observing the fluorescence of the ion Coulomb crystal over time. Ionic reaction products will be trapped in the ion trap and change the shape of the crystal over time. Reaction products lighter than Ca accumulate close to the ion trap center and heavier products are trapped outside of the Ca^+ ions [26, 27, 40, 41].

Chapter 2

Cryogenic Trapping of Neutral Molecules

This chapter covers in detail the design of the cryogenic magnetic trap and shows the experimental apparatus starting from the cold radical source to the trapping region and finishes with the results on long-term trapping of OH radicals. Cold OH radicals are generated by dissociation of water and collisional cooling in a supersonic expansion. They are translationally cooled by Stark deceleration and finally trapped and detected by laser-induced fluorescence (LIF). The neutral trap consists of a cryogenic permanent magnetic trap to confine neutral molecules with a magnetic moment. Therefore, the molecule of choice was the OH radical since it can be Stark decelerated and magnetically trapped in its $X\ ^2\Pi_{3/2}\ (v = 0,\ J = 3/2,\ M_J = 3/2,\ f)$ state.

The trap environment is cryogenically cooled to a temperature of 17 K to suppress black-body-radiation-induced pumping of the molecules out of trappable quantum states and collisions with residual background gas which usually limit the trap lifetime. The cold molecules are thus confined on timescales of tens of seconds, an improvement of up to two orders of magnitude compared to room-temperature experiments, at translational temperatures of approximately 25 mK.

2.1 Trapping of Neutral Molecules

The last two decades brought an immense progress in the generation of translationally cold molecules [17, 42, 43, 44, 45, 46]. The applications range from spectroscopic precision measurements for the exploration of physics beyond the Standard Model [3, 47, 48, 49, 50, 51, 52, 53], experiments on collisions and chemical reactions

at very low temperatures [10, 13, 54, 55, 56, 57, 58, 59, 60], and new approaches to quantum simulation [61, 62] and quantum information [63, 64]. Most of them share the necessity for long interaction times of cold molecules with either radiation or other particles in traps over long periods of time. Trapping of cold molecules was achieved with various methods. Cold polar molecules generated by Stark deceleration [65, 66] or by velocity selection followed by Sisyphus cooling have been stored in electrostatic traps [35, 67, 68, 69, 70]. Paramagnetic molecules were decelerated to low velocities [71], generated using cryogenic-buffer gas cooling [72] or produced by photodissociation [73] and have been confined in electromagnetic [72, 74], permanent magnetic [73, 75, 76, 77, 78, 79, 80] and recently superconducting magnetic traps [81]. Furthermore, cold molecules formed by photoassociation [82] or magnetoassociation [83] were optically trapped. Recently, the first magneto-optical traps (MOT) for molecules have been developed [84, 85].

For neutral atoms in atom traps and ions in ion traps trapping-times on the order of minutes are very common [43, 86]. The commonly reached trap lifetimes of cold polar molecules range from milliseconds to a few seconds. A few exceptions reached the regime of trapping-times of tens of seconds [67, 69, 70, 87].
There are several reasons for these limits in the trap lifetimes of trapped neutral molecules. Even under the ultrahigh-vacuum conditions of typical experiments, collisions of trapped molecules with background-gas molecules occur on timescales of seconds. They usually transfer enough kinetic energy to the confined molecules leading to ejection from the trap. Furthermore, reactive collisions with background molecules decrease density from the trap [88]. Another strongly limiting effect for trapped polar molecules is the interaction with the ambient black-body radiation (BBR) field. Trapped molecules can be pumped into quantum states which are not magnetically or electrically trappable and therefore lead to the loss of their confinement [35]. These limits on the trap lifetime represent a severe obstacle for several applications of cold molecules. Precision spectroscopic measurements require long interaction times of the radiation with the molecules [42, 51, 89]. As the vast majority of all chemical reactions have cross sections far below the collision limit, they require long contact times between the collision partners to obtain a significant reaction yield. Therefore, studies of reactions with trapped molecules have so far been limited to fast processes [54]. Similarly, many applications in quantum science also require long trapping and coherence times of the particles. The capability to store and coherently manipulate cold ions for minutes has been

one of the main reasons for the impressive success of ion-trap based approaches to quantum computing [90].

To achieve long trapping times exceeding previous room-temperature studies, we developed a cryogenic magnetic trap to confine Stark-decelerated molecules. The cryogenic environment efficiently reduces the intensity of the ambient BBR field and further improves the vacuum conditions enabling an improvement of the trapping-times. The trap lifetime achieved is similar to the one reported in previous cryogenic trapping experiments of molecules loaded from buffer-gas [87] or velocity-selection sources [67, 69, 70]. A model to estimate the effect of the interaction with ambient BBR on the trapping times was developed (sec. 2.5.2). With Stark deceleration being one of the most important techniques for the generation of cold polar molecules [17], the presented results (sec. 2.7.2) lay the foundations for new experiments using trapped cold molecules in precision spectroscopy, in studies of slow chemical processes at low energies and in the quantum technologies.

2.2 The OH Radical

To be able to discuss the LIF detection for OH radicals, we need to discuss their electronic structure. The OH molecule has 9 electrons. The electronic ground state has a configuration of $(1s\sigma)^2(2s\sigma)^2(2p\sigma)^2(2p\pi)^3$. It is an open shell radical with one free electron in a $(2p\pi)$ orbital. The projections of the total electronic orbital angular momentum $\mathbf{L}$ and the total electron spin angular momentum $\mathbf{S}$ onto the internuclear axis are $\Lambda = \pm 1$ and $\Sigma = \pm 1/2$ which results in the term symbol X $^2\Pi$. The first electronic excited state has an electron configuration of $(1s\sigma)^2(2s\sigma)^2(2p\sigma)^1(2p\pi)^4$ with one electron in the $(2p\sigma)$ orbital. Thus we have $\Lambda = 0$ and $\Sigma = \pm 1/2$ which leads to the A $^2\Sigma^+$ term. Figure 2.2.1 shows a molecular-orbital (MO) diagram for OH, in which the configuration leading to the X $^2\Pi$ term is highlighted in blue and for A $^2\Sigma^+$ in red, respectively. In the transition from X to A, an electron from the $2p\sigma$ MO is excited to the $2p\pi$ MO. To discuss the rotational structure of OH, we need to discuss the coupling of angular momenta in diatomic molecules. Therefore the Hund's coupling scheme for cases a) for the electronic ground state X $^2\Pi$ term and b) for the electronic first excited state A $^2\Sigma^+$ will be discussed.

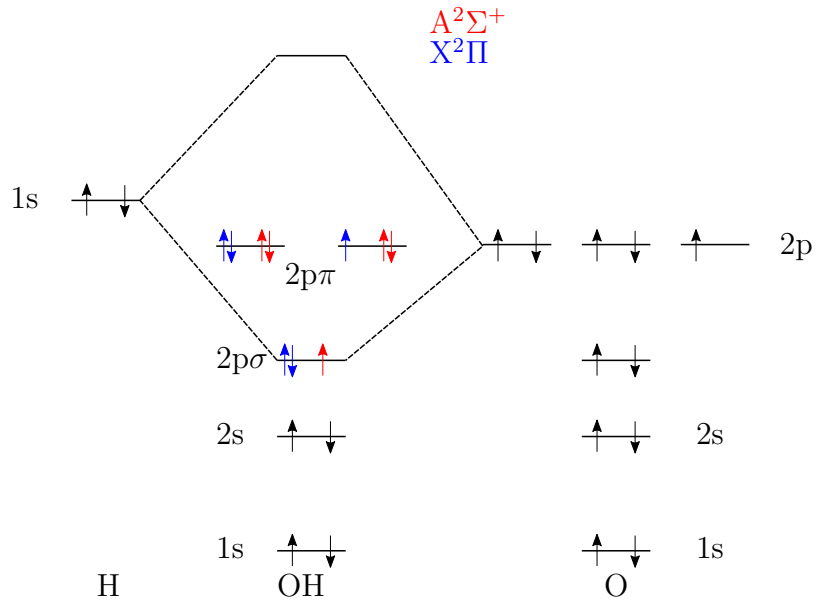

Fig. 2.2.1: **Molecular-Orbital (MO) Diagram for OH.** The configuration $(1s\sigma)^2(2s\sigma)^2(2p\sigma)^2(2p\pi)^3$ leading to the $X\ ^2\Pi$ term is highlighted in blue arrows. The first electronic excited state with the configuration $(1s\sigma)^2(2s\sigma)^2(2p\sigma)^1(2p\pi)^4$ leads to the A $^2\Sigma^+$ term, highlighted by red arrows. The arrow's directions represent the relative signs in the electron spin quantum numbers m_S.

2.2.1 The X $^2\Pi$ State

The best description of the OH molecule in the $X\ ^2\Pi$ ground state in low rotational states is given by the Hund's case a) coupling scheme [91, 92]. The total electron spin angular momentum **S** is coupled to **L** by strong spin-orbit interactions, both being strongly coupled to the internuclear axis [93]. The strongly coupled angular momenta are the sum of the projections of **L** and **S** leading to the spin-orbit manifolds $\mathbf{\Omega} = \mathbf{\Lambda} + \mathbf{\Sigma}$. In the case of OH, this results in $\Omega = \pm 1/2,\ \pm 3/2$. The final term symbol is then commonly written as $^{2|\Sigma|+1}|\Lambda|_{|\Omega|}$ which gives the terms $^2\Pi_{3/2}$ and $^2\Pi_{1/2}$ in our case, also referred as the F_1 and F_2 manifolds. The spin-orbit interaction is described by the Hamiltonian $\hat{H}_{\mathrm{SO}} = A_{\mathrm{SO}}\mathbf{L}\cdot\mathbf{S}$, where A_{SO} is the spin-orbit coupling constant. Since A_{SO} is negative for OH, $^2\Pi_{3/2}$ is lower in energy than $^2\Pi_{1/2}$ [94, 95].

The total angular momentum **J** is then given by adding the angular momentum of the rotation of the nuclei **R** and **Ω**. The rotational structure is then determined by the rotational and spin-orbit Hamiltonian [95]

$$\hat{H}_{\mathrm{rot}} = B_v\left(\mathbf{J}-\mathbf{L}-\mathbf{S}\right)^2 + A_v\mathbf{L}\cdot\mathbf{S}\ , \tag{2.2.1}$$

where B_v is the rotational constant and A_v the spin-orbit coupling constant for a given vibrational quantum number v, which are 18.515 cm^{-1} and -139.73 cm^{-1} for OH in the vibrational ground state [96]. Since a diatomic molecule is classified as a symmetric top, the rotational wave function can be written as [94]

$$|J\Omega M_J\rangle = \sqrt{\frac{2J+1}{8\pi^2}} D^{(J)}_{M\Omega}(\phi,\theta,\chi)^* \ , \tag{2.2.2}$$

with the projection of the total angular momentum $\mathbf{J}$ on the laboratory $\hat{Z}$-axis M_J. $D^{(J)}_{M\Omega}(\phi,\theta,\chi)^*$ is a rotation matrix element which describes the molecular rotation using the Euler angles ϕ, θ and χ. Symmetrized wave functions with well defined parity are constructed from linear combinations of $|J\Omega M_J\rangle$ as

$$|J\Omega M_J\epsilon\rangle = \frac{1}{\sqrt{2}}\left(|J\Omega M_J\rangle\, \epsilon\, |J-\Omega M_J\rangle\right) \ , \tag{2.2.3}$$

with $\epsilon = \pm$ and the total parity of the wave function being

$$p = \epsilon(-1)^{J-S} \ . \tag{2.2.4}$$

The eigenfunctions of $\hat{H}_{\mathrm{rot}}$ can then be evaluated as [97]

$$\left|^2\Pi_{3/2}, JM_J\epsilon\right\rangle = c_1(J)\,|J,\Omega=1/2,M_J\epsilon\rangle + c_2(J)\,|J,\Omega=3/2,M_J\epsilon\rangle \tag{2.2.5}$$

$$\left|^2\Pi_{1/2}, JM_J\epsilon\right\rangle = -c_2(J)\,|J,\Omega=1/2,M_J\epsilon\rangle + c_1(J)\,|J,\Omega=3/2,M_J\epsilon\rangle \ , \tag{2.2.6}$$

with the mixing coefficients $c_1(J)$ and $c_2(J)$

$$c_1(J) = \sqrt{\frac{X+Y-2}{2X}}, \tag{2.2.7}$$

$$c_2(J) = \sqrt{\frac{X-Y+2}{2X}} \tag{2.2.8}$$

with X and Y given by

$$X = \sqrt{4\left(J+\frac{1}{2}\right)^2 + Y(Y-4)}, \tag{2.2.9}$$

$$Y = \frac{A_v}{B_v}. \tag{2.2.10}$$

The mixing coefficients for OH in the X $^2\Pi J = 3/2$ state are $c_1 = 0.174$ and $c_2 = 0.98$ [97]. So far rotational levels which only differ in parity are degenerate. However, the

gyroscopic effect of **J** on **S** and **L** leads to a mixing between the the ground state X $^2\Pi$ and the first excited electronic state A $^2\Sigma^+$, called the Λ-doubling. For OH, this leads to a splitting between the functions with opposite parity of 0.056 cm^{-1} [98]. A schematic energy level diagram can be found in fig. 2.3.6, where the dipole allowed transitions are discussed. This figure also uses another notation for the parities: wave functions with $(-1)^{J-1/2}$ parity are assigned a label e and the ones with a parity of $-(-1)^{J-1/2}$ are labeled f for half-integer values of J [99].

2.2.2 The A $^2\Sigma^+$ State

The first excited electronic state A $^2\Sigma^+$ is best described as Hund's case b). In this case, while **L** is strongly coupled to the internuclear axis, **S** is not. The rotation **R** and the electronic orbital angular momenta **L** are first coupled to give $\mathbf{N} = \mathbf{\Lambda} + \mathbf{R}$. The total angular momentum is then given by $\mathbf{J} = \mathbf{N} + \mathbf{S}$ [94, 95].
The Hamiltonian in this case can be written as

$$\hat{H}_{\text{rot}} = B_v \mathbf{N}^2 + \frac{\gamma_v}{2}\left(\mathbf{J}^2 - \mathbf{S}^2 - \mathbf{N}^2\right) \tag{2.2.11}$$

which includes the spin-rotation interaction in the second term. The strength of this interaction scales with γ_v, which itself depends on the vibrational quantum number v.
The resulting energy levels are given by [94, 95]

$$F_1(N) = B_v N(N+1) + \frac{\gamma_v}{2} N \ , \tag{2.2.12}$$

$$F_2(N) = B_v N(N+1) - \frac{\gamma_v}{2}(N+1) \ . \tag{2.2.13}$$

A resulting energy level diagram is shown in in fig. 2.3.6.

2.3 Cold OH Radical Source

This section discusses the source of internally and externally cold OH radicals. A schematic of the source is shown in fig. 2.3.1. A molecular beam of internally cold OH radicals was generated using a Nijmegen pulsed valve (NPV)[28] together with a pinhole discharge assembly (1) [29]. The beam of OH radicals was then translationally cooled, using a 124-stage Stark decelerator (2) [18]. The molecules were detected by measuring laser-induced fluorescence (LIF), where the molecules are excited via a pulsed dye laser with a wavelength of 282 nm (3). The LIF from the interaction region (4) was detected by a photomultiplier tube (PMT). The section will end with experimental results on a cold OH radical beam, which can be loaded into the magnetic trap. The coordinate system shown in fig 2.3.1 originates in the interaction point (4) and will be used throughout this thesis.

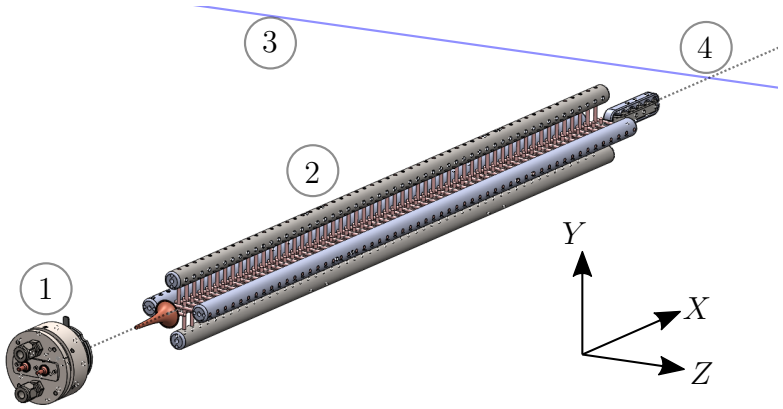

Fig. 2.3.1: **Schematic of the Cold OH radical Source.** The source consists of a Nijmegen pulsed valve (NPV) combined with a pinhole-discharge unit (1), to produce internally cold OH radicals, followed by a 124-stage Stark decelerator (2) to slow down the molecules. The molecules are excited, using a pulsed dye laser at 282 nm (3) and the laser-induced fluorescence (LIF) from the interaction region (4) is collected by a photomultiplier tube (PMT). The coordinate system originates in the interaction point (4).

2.3.1 Internally Cold Radicals: Valve

All methods to produce a OH radical beam have a pulsed valve in common, but they deviate in the generation of the radicals, which has so far been achieved various methods such as photolysis [100, 101], radiofrequency discharge [102] and DC-discharge [103].

The valve used for the presented experiments was built and characterized in this

group by Ludger Ploenes and Dominik Haas and utilizes a DC-discharge method for radical generation, since it was shown to be a simple and cost-effective technique by Lewandowski et al. [104]. A detailed description of the valve parameters can be found in [29, 105]. The valve is able to create short pulses of few tens of μs duration [28]. The opening of the valve leads to the expansion of roughly one percent of H_2O vapor seeded in Kr carrier gas with a stagnation pressure of about 2.0 - 2.5 bars into vacuum. The expanding molecular beam is passing electrodes, which are used to produce an electric discharge pulse at a voltage difference of about 900 V. The water molecules are dissociated and internally cooled by collisions with the seeding gas in the process of the supersonic expansion [106]. This method produces a molecular beam of OH with a ground state population (X $^2\Pi\,(v = 0)$) of over 99%, a mean velocity between 420 m/s - 500 m/s, a velocity spread (full width at half maximum, FWHM) of about 13% and a density on the order of 8×10^9 cm^{-3} at about 100 mm distance from the valve [29, 105].

2.3.2 Translationally Cold Radicals: Stark Deceleration

Before we can start the discussion about the Stark deceleration, we start with a short derivation of the first order matrix elements for the Stark effect, which describes the interaction of the permanent electric dipole moment with an electric field. This derivation will be carried out for the Hund's case a) coupling scheme which applies to the electronic ground state of the OH radical to be decelerated in our experiments.

2.3.2.1 The Stark Effect

In short, the interaction V between the permanent electric dipole moment $\boldsymbol{\mu}_\mathrm{e}$ and an external electric field $\mathbf{E}$ can be expressed as $V = -\boldsymbol{\mu}_\mathrm{e} \cdot \mathbf{E}$. Usually, the electric field vector $\mathbf{E}$ is defined in the laboratory frame $(\hat{X}, \hat{Y}, \hat{Z})$ and the dipole moment $\boldsymbol{\mu}_\mathrm{e}$ has a defined orientation in the body-fixed molecular frame $(\hat{x}, \hat{y}, \hat{z})$. Thus, it can be helpful to define these vectors as rank one irreducible spherical tensor operators leading to the Hamiltonian [94]

$$H_\mathrm{Stark} = -\boldsymbol{\mu}_\mathrm{e} \cdot \mathbf{E} = \sum_{p=-1}^{1} T_p^1(\boldsymbol{\mu}_\mathrm{e}) T_p^1(\mathbf{E})(1, p), \tag{2.3.1}$$

where $T(\boldsymbol{\mu})$ and $T(\mathbf{E})$ are defined in the space-fixed laboratory frame. The spherical tensor basis connects to the space fixed frame as

$$\begin{aligned} T_1^1(\boldsymbol{\mu}) &= -\frac{1}{\sqrt{2}}(\mu_X + i\mu_Y) \\ T_0^1(\boldsymbol{\mu}) &= \mu_Z \\ T_{-1}^1(\boldsymbol{\mu}) &= \frac{1}{\sqrt{2}}(\mu_X - i\mu_Y) \ . \end{aligned} \tag{2.3.2}$$

Let the space-fixed coordinate system be chosen such that $\mathbf{E}$ is directed along $\hat{Z}$, so $\mathbf{E} = E\hat{Z}$. This simplifies H_{Stark} to

$$H_{\text{Stark}} = -T_0^1(\boldsymbol{\mu}_{\text{e}})E \ , \tag{2.3.3}$$

where $T_0^1(\boldsymbol{\mu}_{\text{e}})$ is the projection of the dipole moment on the $\hat{Z}$-axis. As $\boldsymbol{\mu}_{\text{e}}$ is defined in the molecular coordinate system, it rotates with the molecule. Using the Wigner rotation matrices, we can transform from the laboratory frame to the molecular frame as [95]

$$T_0^1(\boldsymbol{\mu}_{\text{e}}) = \sum_{q=-1}^{1} D_{0,q}^{(1)}(\phi,\theta,\chi)^* \, T_q^1(\boldsymbol{\mu}_{\text{e}}) \ , \tag{2.3.4}$$

where ϕ, θ and χ are the Euler angles, which define the orientation of $\hat{X}, \hat{Y}$ and $\hat{Z}$ relative to $\hat{x}, \hat{y}$ and $\hat{z}$. Using eqns. (2.3.3), (2.3.4) and (2.2.2) as well as the properties of the Wigner rotation matrices [95], we can calculate the Stark matrix elements:

$$\begin{aligned} &\langle J\Omega M_J | \, H_{\text{Stark}} \, | J'\Omega' M_J' \rangle = \frac{E}{8\pi^2}\sqrt{(2J+1)(2J'+1)} \sum_{q=-1}^{1} T_q^1(\boldsymbol{\mu}_{\text{e}}) \int d\omega D_{M\Omega}^{(J)*} D_{0q}^{(1)*} D_{M'\Omega'}^{(J')} \\ &= -\frac{E}{8\pi^2}\sqrt{(2J+1)(2J'+1)} \sum_{q=-1}^{1} T_q^1(\boldsymbol{\mu}_{\text{e}})(-1)^{M'-\Omega'-q} \int d\omega D_{-M-\Omega}^{(J)} D_{0-q}^{(1)*} D_{M'\Omega'}^{(J')} \\ &= -E\sqrt{(2J+1)(2J'+1)} \sum_{q=-1}^{1} T_q^1(\boldsymbol{\mu}_{\text{e}})(-1)^{M'-\Omega'-q} \begin{pmatrix} J' & 1 & J \\ -M_J' & 0 & M_J \end{pmatrix} \begin{pmatrix} J' & 1 & J \\ -\Omega' & -q & \Omega \end{pmatrix} \ . \end{aligned} \tag{2.3.5}$$

Since the dipole moment of a diatomic molecule as well as $\boldsymbol{\Omega}$ are directed along the internuclear axis, only $q = 0$ remains in eq. (2.3.5) and we get

$$\langle J\Omega M_J | \, H_{\text{Stark}} \, | J'\Omega' M_J' \rangle =$$

$$- E\sqrt{(2J+1)(2J'+1)}\mu_{e,z}(-1)^{M'-\Omega'} \begin{pmatrix} J' & 1 & J \\ -M'_J & 0 & M_J \end{pmatrix} \begin{pmatrix} J' & 1 & J \\ -\Omega' & 0 & \Omega \end{pmatrix} . \quad (2.3.6)$$

From the properties of the Wigner 3-J symbols [95] we can directly extract the selection rules as

$$J = J' \pm 1,\ J = J' \quad (2.3.7)$$

$$M_J = M'_J, \quad (2.3.8)$$

$$\Omega = \Omega' . \quad (2.3.9)$$

As the energy splitting between the rotational levels in OH is relatively large, the $J = J' \pm 1$ case can be neglected. Further applying the selection rules, we can write eq. (2.3.6) as

$$\langle J\Omega M_J | H_{\text{Stark}} | J'\Omega' M'_J \rangle = -\mu_{e,z} E \frac{M_J \Omega}{J(J+1)} . \quad (2.3.10)$$

Using the symmetrized, parity adapted basis as defined in eq. 2.2.3, the non-vanishing matrix elements are given by

$$Q = \langle J\Omega M_J \pm | H_{\text{Stark}} | J'\Omega' M'_J \mp \rangle = \langle J\Omega M_J | H_{\text{Stark}} | J'\Omega' M'_J \rangle , \quad (2.3.11)$$

which couple states of opposite parity [17]. Finally, we can set up the first order Stark matrix in the parity adapted basis, including the Λ-doubling energy for the upper doublet E_Λ as

$$\begin{pmatrix} 0 & Q \\ Q & E_\Lambda \end{pmatrix}$$

and obtain the Stark energy form the eigenvalues as

$$E_{\text{Stark}} = \frac{E_\Lambda}{2} \pm \sqrt{\left(\frac{E_\Lambda}{2}\right)^2 + \left(\mu_{\text{e}} E \frac{M_J \Omega_{\text{eff}}}{J(J+1)}\right)^2}, \quad (2.3.12)$$

where Ω_{eff} denotes the effective value of the Ω quantum number, which is ± 1.46 for OH in the $X^2\Pi_{3/2}, J = 3/2$ state and deviates from $\pm 3/2$ due to mixing between the $X^2\Pi_{3/2}$ and $X^2\Pi_{1/2}$ spin-orbit manifolds [17, 97]. Fig. 2.3.2 shows the Stark energy shift in dependence of the electric field for OH in the $X^2\Pi_{3/2}, J = 3/2$ state, using Ω_{eff}. It illustrates the non-linear behavior for low electric field strengths E around

a few kV cm^{-1} and the change to the linear regime for higher E. From this graph, one can directly see that E_{Stark} decreases with higher E for positive values of $M_J\Omega$, while it increases for negative values of $M_J\Omega$. The first case is called a high-field seeking state and the latter a low-field seeking state.

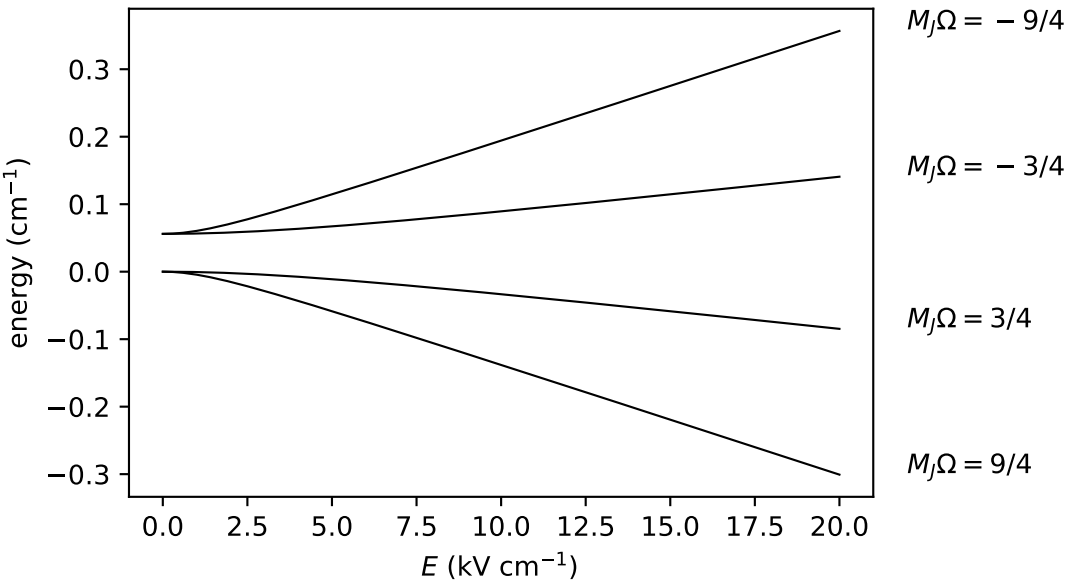

Fig. 2.3.2: **Stark Shift for the OH Radical.** The Stark shift for the OH radical in the $X^2\Pi_{3/2}(J = 3/2)$ state is shown. For low electric field strengths E around a few kV cm^{-1}, the shift is clearly non-linear which changes for higher E.

2.3.2.2 Stark Deceleration

To reduce the kinetic energy of the internally cold package of OH radicals, we use a Stark decelerator. In a Stark decelerator, a force is exerted on the molecule which is described by

$$\mathbf{F}(\mathbf{X}) = -\nabla E_{\text{Stark}}(\mathbf{X}) \ , \tag{2.3.13}$$

thus an inhomogeneous electric field is required. The gradient in the electric field is generated by a pair of opposing electrodes to which voltages with opposite polarities are applied. To remove enough energy to reach low velocities of the decelerated package, an array of such electrodes is used. Fig. 2.3.3 shows the schematics of a decelerator. To ensure a net removal of energy, the decelerator is switched between two configurations in a time-varying sequence: Configuration 1 is switched on when the particle enters the decelerator. As soon as the particle reaches a desired position along the decelerator, configuration 2 is switched on. This cycle is repeated until the molecular package exits the decelerator. Since the geometry of the decelerator

is periodic, where each electrode pair is separated by distance L, which is 5.5 mm in our case, it is convenient to define the position between two electrodes by a so-called phase angle ϕ_0, as illustrated in fig. 2.3.3, defined by

$$\phi_0 = \pi \frac{X}{L} \ , \tag{2.3.14}$$

where $X = 0$ lies in the center between the last and the next electrode pair.

When the potentials in the decelerator are switched at a constant phase angle $\phi_0 = 0$, the molecule is decelerated and accelerated by the same amount over one switching cycle and its velocity is unchanged as visible in the Stark energy shift in fig. 2.3.3. Switching the electric fields at a constant frequency leads to the so-called guiding mode. The longitudinal velocity remains constant and the ensemble of molecules are focused along the transversal axes. The switching sequence will only match perfectly for a molecule with a well defined initial position and velocity, where the phase angle remains constant, referred to as the synchronous molecule [92]. With positive phase angles, a molecule in a low-field seeker state can be decelerated over several switching cycles, losing kinetic energy at every switching cycle.
The potential energies can be described as Fourier series with relative phase shifts of $\pi/2$. The loss of kinetic energy for the synchronous molecule over a switching cycle $\Delta W(\phi_0)$ can be expressed as

$$\Delta W(\phi_0) = W(\phi_0 + \pi) - W(\phi_0) = 2a_1 \sin\phi \ , \tag{2.3.15}$$

where $W(\phi_0)$ is the Stark potential at position ϕ_0 and a_1 is the second coefficient in the Fourier series [107]. It can be approximated as $a_1 \approx (W(3\pi/2) - W(\pi/2))/2$ which is about 0.07 cm^{-1} for our decelerator operated at voltages of ± 10 kV, the voltage used throughout this thesis [105]. The average force acting on a decelerated particle can now be approximated as

$$F(\phi_0) = \frac{-\Delta W(\phi_0)}{L} = \frac{-2a_1 \sin\phi}{L} \ . \tag{2.3.16}$$

In reality, most of the molecules won't be perfectly synchronous with the decelerator's switching sequence as every source of molecules has some position and velocity spread. We therefore set up the equation of motion for a non-synchronous molecule

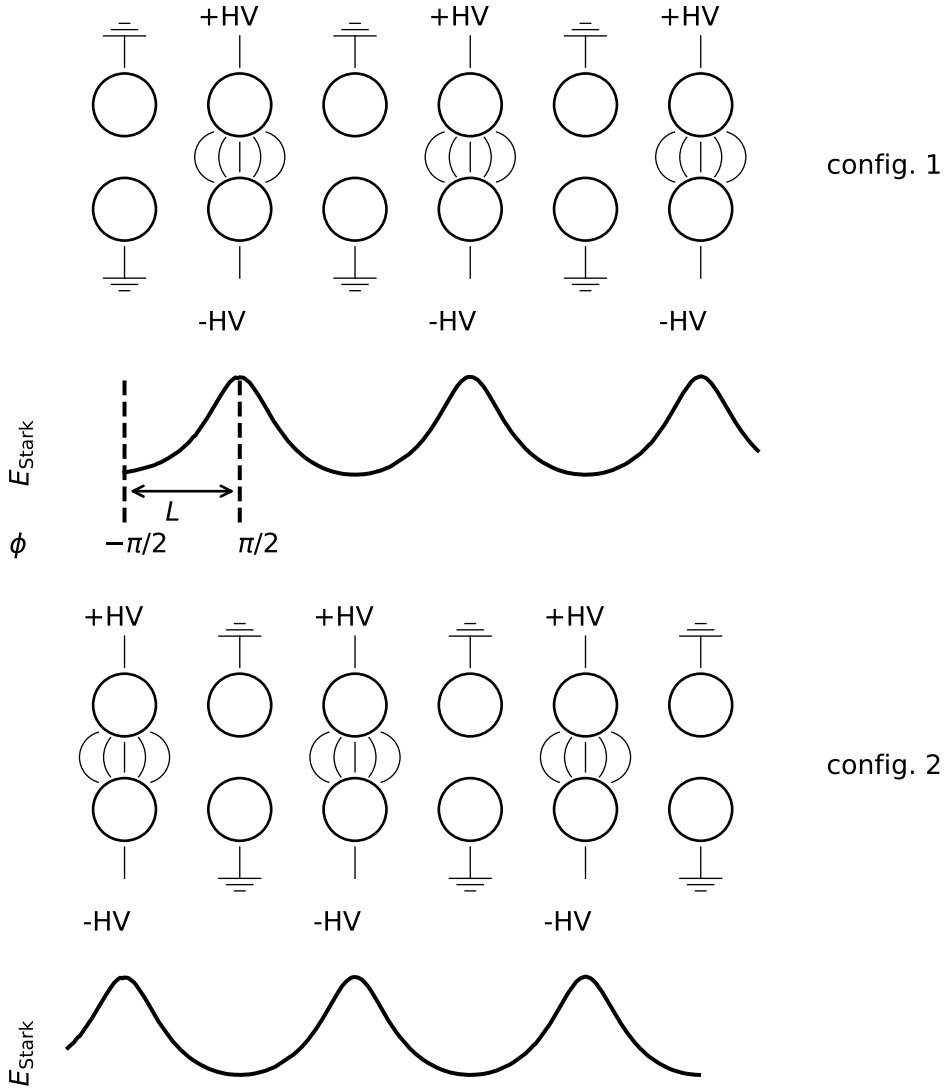

Fig. 2.3.3: **Stark Decelerator Operation.** The circles are schematics for the Stark decelerator electrodes. While the even (odd) pairs are grounded, high voltage (HV) of opposite polarity is applied to the odd (even) pairs. The upper half shows configuration 1, the lower half configuration 2. By switching between these configurations, the kinetic energy of the molecule can be continuously decreased. The Stark energy shift E_{Stark} is schematically shown below each configuration. The phase angle ϕ_0 is given below config. 1, using the definition from[17].

with an offset in phase angle of $\Delta\phi$ as

$$\frac{mL}{\pi}\frac{\mathrm{d}^2\Delta\phi}{\mathrm{d}t^2} = F(\phi_0+\Delta\phi) - F(\phi_0) = \frac{-2a_1}{L}(\sin(\phi_0+\Delta\phi) - \sin(\phi_0)) \ . \qquad (2.3.17)$$

Fig. 2.3.4 shows the phase space stability diagram for a phase angle $\phi_0 = 55.468°$ which is a result from integrating the equation of motion from eq. 2.3.17 for different

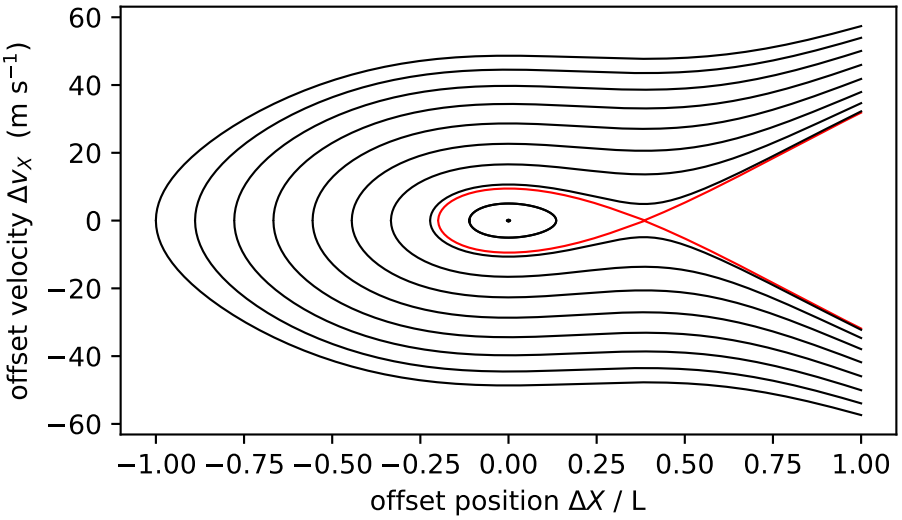

Fig. 2.3.4: **Phase Space Stability.** The equations of motion for an OH radical in our Stark decelerator operated at a phase angle of $\phi_0 = 55.468°$ were solved and their trajectories are shown. The red line shows the boundary of phase-stable confinement of molecules in the decelerator, the so-called the separatrix. Molecules inside this separatrix can be efficiently confined and decelerated.

initial conditions[1] . The red line shows the boundary of phase-stable confinement of molecules in the decelerator, the so-called the separatrix. Molecules inside this separatrix can be efficiently confined and decelerated, whereas molecules outside are lost over time. The separatrix is calculated from the maximum offset velocity Δv_X which is still trapped by the potential, given by

$$\Delta v_X = \pm\sqrt{\frac{4a_1}{\pi m}(\cos(\phi_0 + \Delta\phi) + \cos(\phi_0) + \sin(\phi_0)(\Delta\phi - \pi + 2\phi_0)} \ , \qquad (2.3.18)$$

where a derivation can be found e.g. in the thesis of D. Haas [105]. Given some initial velocity, the final velocity of a molecule is therefore determined by the phase angle and the number of deceleration stages.

Since the number of deceleration stages remains constant for our Stark decelerator, we have to increase the phase angle ϕ_0 for the synchronous molecule, to reach lower velocities. Fig. 2.3.5 shows separatrices for several ϕ_0. The phase space volume for stable trajectories is reduced for higher ϕ_0 meaning that for lower final velocities, the density in the decelerated packages will be reduced.

[1]This phase angle leads to a final velocity of 29 m/s with an initial velocity of 425 m/s and was later 2.7 used as loading velocity for the trap.

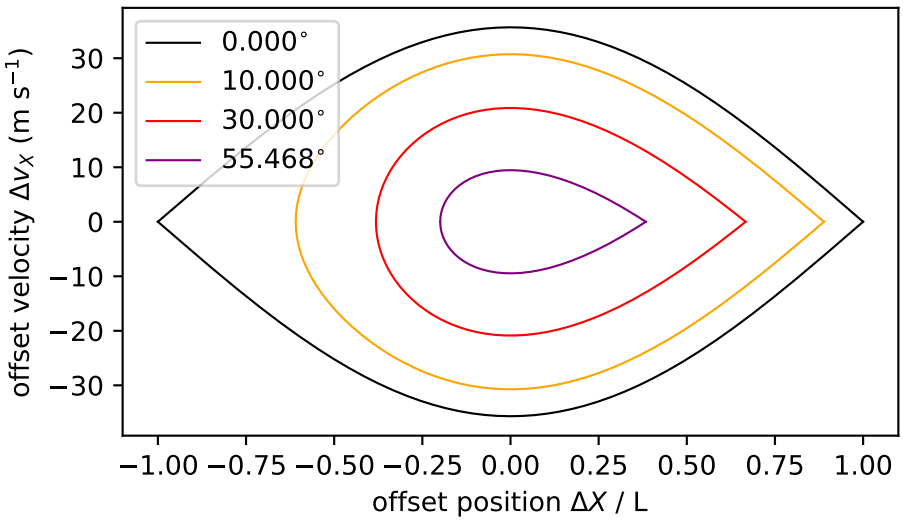

Fig. 2.3.5: **Phase Space Acceptance.** The phase stable regions shown for several phase angles ϕ_0. The stable phase-space volume decreases as ϕ_0 increases.

2.3.3 Detection of Radicals

This section covers the detection of the OH radicals. We start with the discussion about the molecular electronic transitions in our laser LIF measurements. We present the methods for reduction of background stray light. Furthermore, the raw data as collected on the oscilloscope is shown and the methods we use to produce the integrated LIF-time-of-flight (TOF) curves are presented. The signal quality in terms of photons from the LIF signal and photons from scattered light in the background is quantified. Finally, LIF-TOF measurements of internally and translationally cold OH radicals with final velocities of 29 m/s are shown.

2.3.3.1 Laser Induced Fluorescence

OH radicals are typically detected via resonance enhanced multi-photon ionization (REMPI) or LIF. While REMPI provides a higher sensitivity, it suffers from low transition probabilities and has a more complicated implementation [108, 109]. Thus our method of choice was LIF.

The OH radicals are excited from the $X^2\Pi(v = 0)$ ground state to the first electronically excited state $A^2\Sigma^+(v = 1)$ at a wavelength of 282 nm [96], where v is the vibrational quantum number, and the fluorescence from the transition $A^2\Sigma^+(v = 1) - X^2\Pi(v = 1)$ at a wavelength of 313 nm is collected on a PMT. Due to the difference in wavelength, the signal fluorescence can be distinguished from the excitation laser in the background. The selection rules for dipole allowed transitions are given by [96]

$$\Delta J = 0, \pm 1 \ , \tag{2.3.19}$$

$$\Delta N = 0, \pm 1, \pm 2 \tag{2.3.20}$$

as well as changing of the parity $+ \leftrightarrow -$. These are commonly labeled by

$$\Delta N_{F'F''}(N'') \ , \tag{2.3.21}$$

using O, P, Q, R and S to label transitions with $\Delta N = -2, -1, 0, +1, +2$. The N quantum number of the ground state is denoted by N'', F' and F'' denote the ρ-doublet in the excited A state and the Ω manifold in the ground state. For transitions with $F' = F''$, only one subscript is used. Fig. 2.3.6 shows schematics of the first four rotational levels in both spin-orbit manifolds of the $X^2\Pi(v = 0)$ ground state and the first electronically excited state $A^2\Sigma^+(v = 1)$ with some selected dipole allowed

transitions. In the experiments the ground state OH is excited via the $Q_1(1)$ and $Q_{21}(1)$ branches at 282 nm.

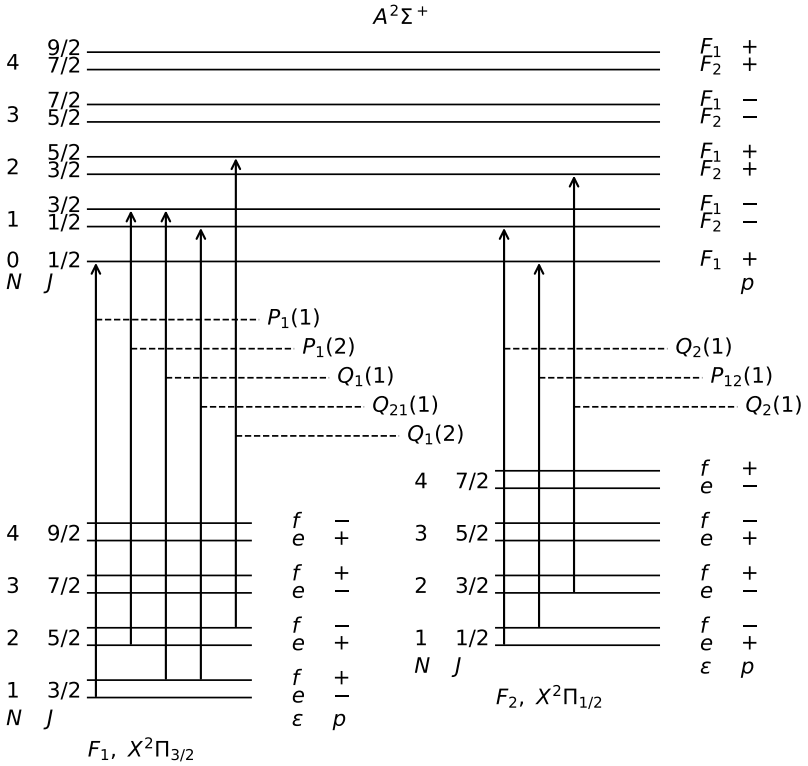

Fig. 2.3.6: **OH Electronic Structure and Dipole Allowed Transitions.** A schematic energy level diagram is shown. In includes the first four rotational levels in both spin-orbit manifolds of the $X^2\Pi(v = 0)$ ground state and the first electronically excited state $A^2\Sigma^+(v = 1)$ with some selected dipole allowed transitions.

2.3.3.2 Detection Laser Setup

To generate laser light at 282 nm, producing pulses of 10 ns duration and an energy of 10 mJ/pulse, a dye laser (Fine Adjustment, Pulsare) with a Rhodamine 6G dye was pumped by the second harmonic (532 nm) of a Nd:YAG laser (Continuum, Surelite II) and was finally frequency-doubled. We found that the OH $X - A$ transition was already saturated at a pulse energy of about 1.5 mJ/pulse. The wavelength of the laser was calibrated with a wavelength meter (High Finesse, WS-7) and a lens ($\varnothing = 50.8$ mm, $f = 50$ mm) was used to collect the fluorescence onto a PMT (Electron Tubes, B2/RFI 9813 QB, C638AFN1).

2.3.3.3 Stray Light Suppression

To reduce stray light at 282 nm in the measured signal from the PMT, combinations of optical filters are used. To maximize the signal-to-noise ratio, we required a filter combination which has a high transmission at 313 nm (fluorescence) and suppresses radiation above and below. If not stated otherwise, the experimental data are measured with a combination of a bandpass filter (Semrock, FF01-315/15-25) and one dichroic long pass mirror (Omega Optical, 305Alp Version 1), which results in a transmission at a wavelength of 313 nm of about 70% and less than 0.2% at a wavelength of 282 nm. The transmissions data is shown in fig. 2.3.7.

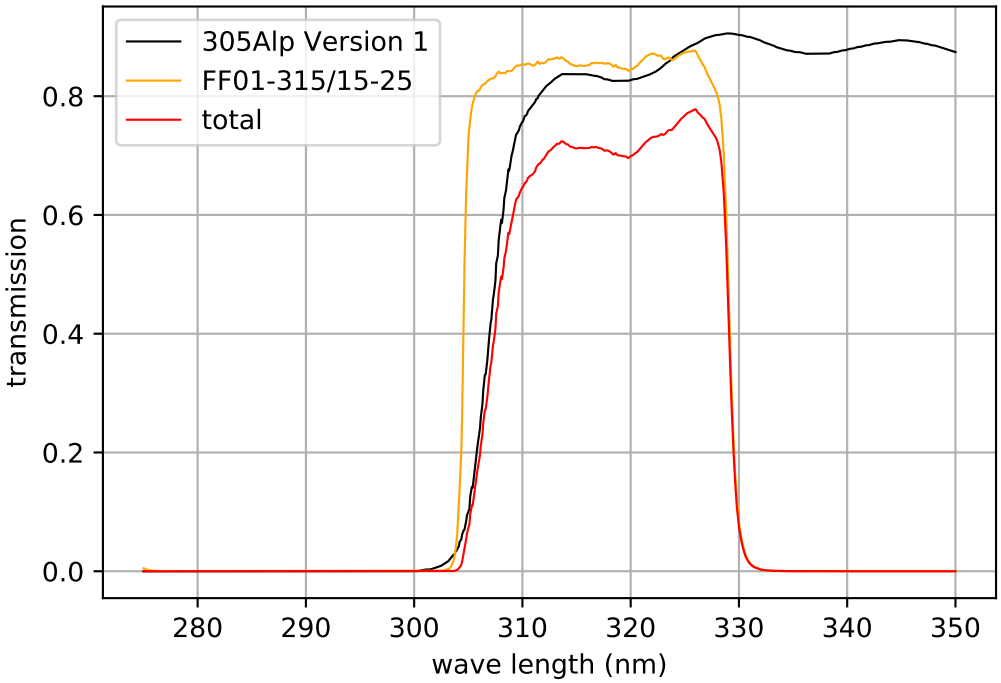

Fig. 2.3.7: **Neutral-Density Filter Characteristics.** The transmission data of the filter combination in this thesis is shown. We used a combination of one bandpass filter (Semrock, FF01-315/15-25) and one dichroic long pass mirror (Omega Optical, 305Alp Version 1), which results in a transmission of about 70% at a wavelength of 313 nm and less than 0.2% at a wavelength of 282 nm.

2.3.3.4 Integrated LIF-TOF

For every TOF measurement of OH radicals in this thesis, the data was handled the same way. The LIF signal from the PMT was preprocessed on the oscilloscope by averaging several (usually 5-10) LIF traces. The time window usually had a width of

2.1 μs. Fig. 2.3.8 shows the preprocessed data, composed of 10 averaged LIF traces as black dots. The OH radicals were guided through the decelerator a a velocity of 425 m/s and the LIF was collected 11.5 mm after the decelerator. The red vertical lines are the boundaries of the integration window. The average of the data points within this window gives the integrated LIF-TOF value for a certain setting during a scan. The highest peak before the time window starts comes from the stray light caused by scattered photons of the pulsed dye laser with a wavelength of 282 nm. In order to reduce the contribution of time-independent noise, the cut-off was chosen accordingly.

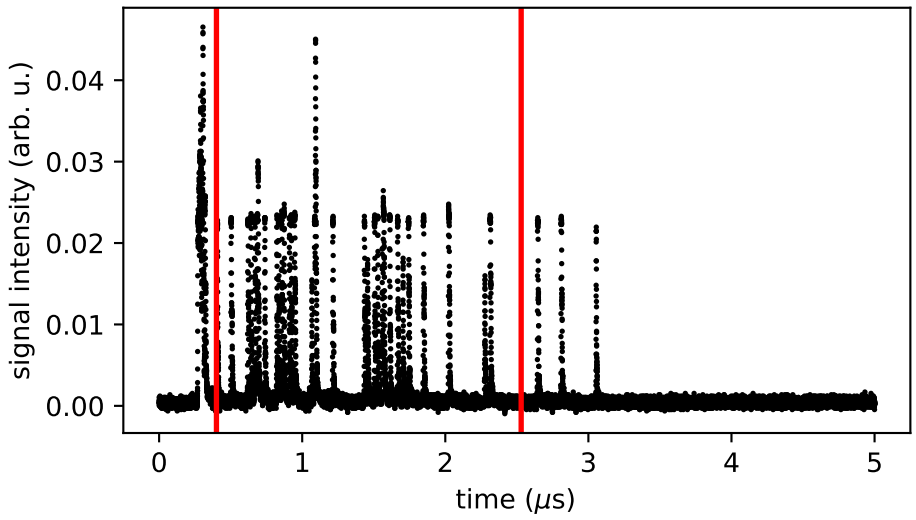

Fig. 2.3.8: **Averaged LIF Trace.** The LIF of OH was recorded and averaged 10 times during a delay scan. The red vertical lines are the boundaries of the integration window. The average of the data points within this window gives the integrated LIF-TOF value for a certain setting during a scan.

2.3.3.5 Photon Counting

For low signal, single photons are distinguishable. By smoothing the signal and defining a signal height of a photon, the number of photons in this time window can be extracted. As this method does not suffer from fluctuations of the offset in the signal, it can lead to lower fluctuations and smaller errors on the signal. Graph a) in fig. 2.3.9 shows the averaged LIF signal from before, divided by the signal height of a single photon, within the integration window as black dots. The red dots show which peak was counted as a photon. Even one double count was found, which can occur when two photons arrive very close in time. The total number of photons in

this case was 28, which gives 2.8 photons per shot. Graph b) in fig. 2.3.9 shows the same data for the background measurement, where the discharge pulse was switched off. It shows a total of 2 photons resulting in 0.2 photons from the background per shot.

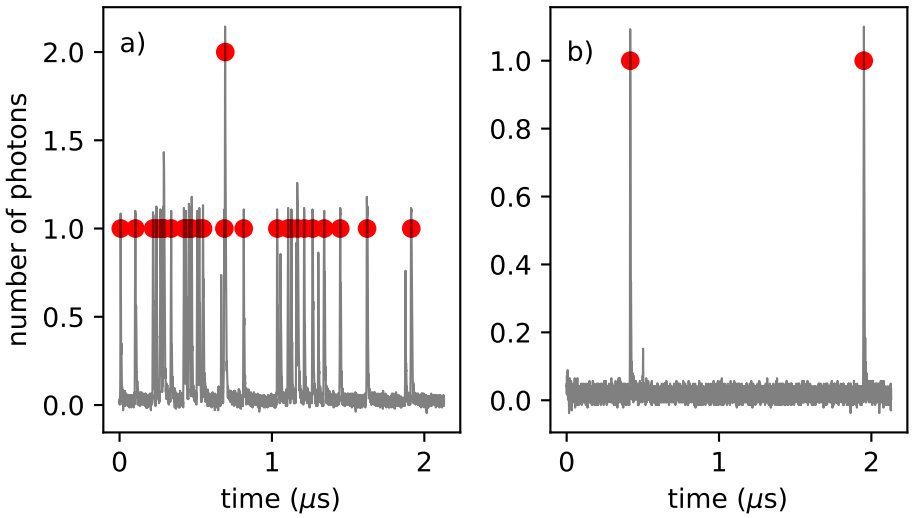

Fig. 2.3.9: **Photon Counting.** The averaged LIF signal from 10 traces within the integration window is shown. After smoothing the single photon peaks could be identified and are labeled with red dots. Graph a) shows the signal with a total of 28 photons, resulting in 2.8 photons per shot. Graph b) shows the corresponding data for the background measurement, where the discharge pulse was switched off. It shows a total of 2 photons resulting in 0.2 photons from the background per shot.

To extract the lifetime of the measured transition in our LIF traces, several measurements can be combined. A histogram of the photon arrival times in the traces can be made. Fig 2.3.10 shows the resulting LIF trace. The arrival times of 4677 photons were combined into 50 bins. As an offset correction, the number of photons in a time window in front of the laser peak, namely 0-0.2 μs were collected and subtracted. The graph in fig. 2.3.10 shows the offset corrected number of photons in each bin against the center time of the temporal bins. The data fits very well to an exponential decay with a $1/e$ lifetime of 717 ns, represented by the red dashed line in fig. 2.3.10. This is in agreement with the value of 717 ns from ref. [110] and serves as a verification for the detection of OH radicals. The error bars are given as the standard deviation for Poisson counting, namely $\sqrt{n}$ where n is the number of photons.

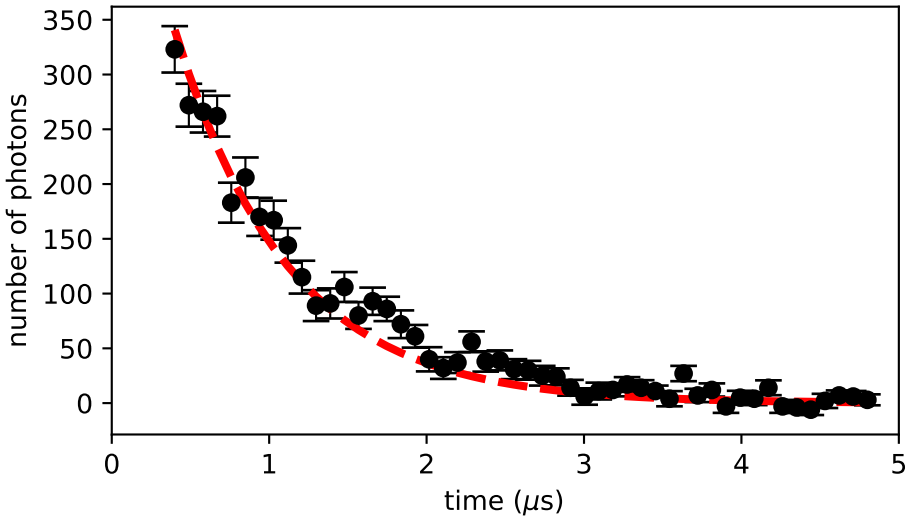

Fig. 2.3.10: **LIF Trace.** The arrival times of 4677 photons were combined into 50 bins. As an offset correction, the number of photons in a time window in front of the laser peak, namely 0-0.2 μs were collected and subtracted. The red dashed line shows an exponential fit with a lifetime of 717 nm. The error bars are given as $\sqrt{n}$ where n is the number of photons.

2.3.4 Results

As our the signal levels were limited by the small detection efficiency due to the small apertures in the cryogenic shields (see sec. 2.5.2.1), we had to produce an internally and translationally cold package of OH radicals with the optimized density. Thus, a repeatable triggering scheme was required, starting with opening the valve and finishing with the collection of LIF data on our computer. Therefore, software (HyT-Control) was developed in the context of this work and is discussed in sec.2.6. The OH package was probed on the decelerator axis, 11.5 mm after the decelerator exit. Figure 2.3.11 shows three traces of integrated LIF-TOF curves of decelerated OH packages with phase angles of 0° (guiding, a)), 53.69° (b)) and 55.468° (c)) and corresponding final longitudinal velocities of 425 m/s, 81 m/s and 29 m/s. The delay in these traces is the time after the start of the DC-discharge pulse in the valve. The intensities were normalized to the highest peak in the guiding signal.

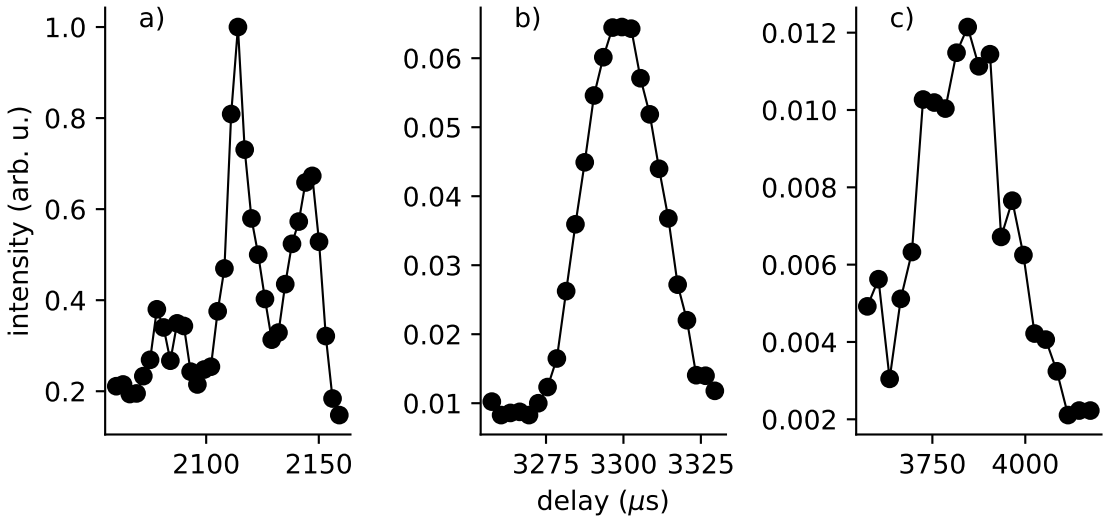

Fig. 2.3.11: **Stark Deceleration of OH.** Integrated LIF-TOF signals of Stark decelerated OH. The selected initial velocity was 425 m/s. Graph a) shows a guiding signal, meaning a phase angle of 0°. Graph b) shows the signal for 81 m/s final velocity at a phase angle of 53.69°. Graph c) shows the measurement for a phase angle 55.468°, resulting in a final velocity of 29 m/s which is the loading velocity our trap was designed for. The black lines connect to dots, to guide the eye. The intensities were normalized to the highest peak in the guiding signal.

Graph a) shows the guiding signal with 3 pronounced peaks. These correspond to three phase-stable packages guided through the decelerator. Graph b) shows the signal of a decelerated package with a final longitudinal velocity of 81 m/s. Graph c) shows the signal for a final velocity of 29 m/s which is the loading velocity for which the trap was designed. As a result, we obtain a cold OH package with peak intensities of around 1% compared to the guiding peak. The spatial width of the package was limited by the decelerator geometry as well as the narrower phase-space acceptance of the decelerator for higher phase angles. The peak densities were calculated by D. Haas [105] and amount to 8×10^7 cm^{-3} for guiding and around 5×10^6 cm^{-3} in packages with 29 m/s final longitudinal velocity. As one can see in the LIF-TOF signals, the OH packages became broader in arrival time for higher phase angles.

2.4 Magnetic Trap for Neutral Molecules

In this section we will discuss the process of developing our neutral trap setup of the hybrid trap. We therefore start with a short introduction about magnetic trapping of molecules, followed by the initial conditions as given by D. Haas who designed the basic structure of the trap and the loading region which consists of two permanent magnets in anti-Helmholtz configuration and four wires to help shaping the potential. This potential is used for the last deceleration pulse in the trap region. We will then continue discussing the implementation of this basic design in a real application including the design of the high voltage setup as well as the cryogenic setup. The main goal is to trap neutral molecules as long as possible to allow measurements of slow reactions. Therefore, we need to reduce the loss of trapped molecules which has its biggest contributions from pumping the molecules out of their trappable states due to interaction with black-body-radiation (BBR) and from collisions with particles in the background gas. Both mechanisms can be reduced by cryogenic cooling of the trap assembly and thus reducing the amount of room temperature BBR illuminating the trapped molecule cloud as well as improving vacuum conditions leading to lower loss rates from collisions with particles from the background.

2.4.1 Magnetic Trapping: Concepts

In order to confine a particle in space, a spatially dependent force is required pushing this particle towards the trap center. Since OH possesses a magnetic moment, we can use an inhomogeneous magnetic field to trap the molecules. The interaction of the magnetic moment with the inhomogeneous magnetic field leads to a position-dependent shift in potential energy. We will briefly discuss the first order Zeeman effect which describes the interaction of the magnetic moment with the inhomogeneous magnetic field. The section ends with the basic design of our magnetic trap with resulting trapping potentials.

2.4.1.1 The Zeeman Effect for OH

Similar to the Stark effect (sec. 2.3.2.1), the interaction of the magnetic moment $\boldsymbol{\mu}_\mathrm{m}$ with an external magnetic field $\mathbf{B}$ is described by the Hamiltonian

$$H_\mathrm{Ze} = -\boldsymbol{\mu}_\mathrm{m} \cdot \mathbf{B} = \frac{\mu_\mathrm{B}}{\hbar} \left(\mathbf{L} + gs\mathbf{S}\right) \cdot \mathbf{B} \tag{2.4.1}$$

$$\approx \frac{\mu_\mathrm{B}}{\hbar} \left(L_z + g_\mathrm{s} S_z\right) \mathbf{B} \ , \tag{2.4.2}$$

where $\boldsymbol{\mu}_\mathrm{m}$ is assumed to lie along the internuclear axis z, g_s is the free electron g-factor ($g_\mathrm{s} \approx 2.00232$) and μ_B the Bohr magneton. The derivation of the matrix elements in the parity-adapted basis works analogous to the derivation of the Stark effect. With the same assumption that the rotational spacing is very large ($J = J'$), we calculate the first order correction to the energy as the matrix elements of H_Ze for Hund's case a) in the the parity-adapted basis:

$$\begin{aligned}
&\langle \Lambda\Sigma J\Omega M_J\epsilon |\, H_\mathrm{Ze} \,| \Lambda\Sigma J\Omega' M_J'\epsilon' \rangle \\
&= (2J+1)(-1)^{M_J-\Omega} \begin{pmatrix} J & 1 & J \\ -M_J & 0 & M_J \end{pmatrix} \begin{pmatrix} J & 1 & J \\ -\Omega & 0 & \Omega \end{pmatrix} \mu_\mathrm{B} B(\Lambda + g_\mathrm{S}\Sigma)\delta_{\epsilon\epsilon'} \\
&= \mu_\mathrm{B} B \frac{M_J\Omega(\Lambda + g_\mathrm{S}\Sigma)}{J(J+1)} \delta_{\epsilon\epsilon'} \ .
\end{aligned} \tag{2.4.3}$$

Fig. 2.4.1 shows a graph of the Zeeman energy shift for OH in the $X^2\Pi_{3/2}$ state for both Λ doublets, which scales linearly with the magnetic field strength B. Only the positive M_J states are magnetic low-field seekers, i.e. trappable. The high-field seekers will not be trapped. Thus 50% of the Stark-decelerated molecules ($M_J = \pm 3/2$) cannot be trapped by the static magnetic fields and are lost.

2.4.1.2 Trap Potential for Two Bar Magnets

To produce the required magnetic field to trap the molecules, we used two Ni-coated bar magnets with a size of 3, 4 and 6 mm in X, Y and Z in the configuration as shown in fig.2.4.3, generating a quadrupolar magnetic field. Similar trap designs have been reported in, e.g., [73, 111, 112]. We employed PrFeB as material for the magnets instead of the more widely used NdFeB because the latter exhibits a decreased magnetization level at cryogenic temperatures due to a spin-reorientation transition [113]. By contrast, the remanence of the PrFeB magnets was specified to increase from 1.40 T at room temperature to 1.64 T under cryogenic conditions [114]. In this thesis, the analytical expression for bar magnets from [115] is used.

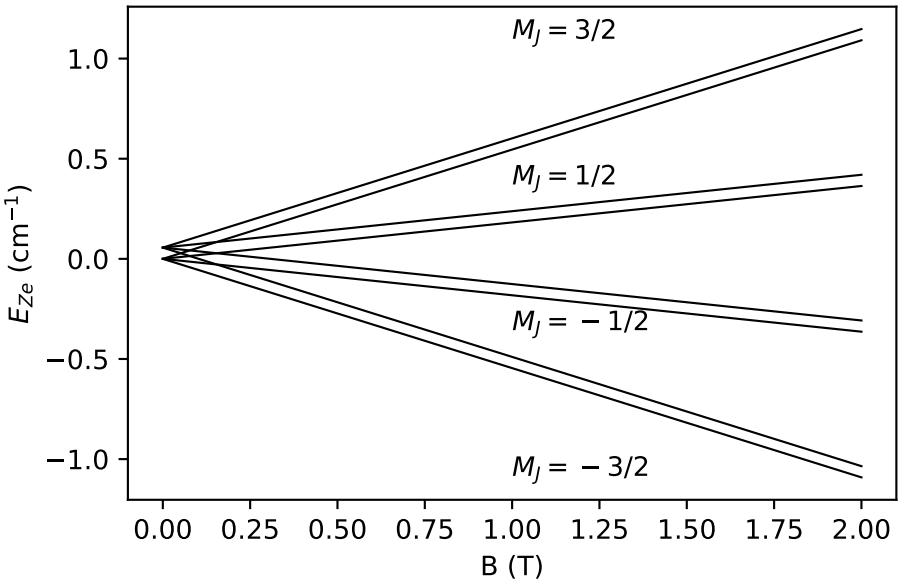

Fig. 2.4.1: **Zeeman Shift for OH.** The Zeeman energy for OH in the $X^2\Pi_{3/2}$ state is shown for both Λ doublets. The Zeeman effect does not couple states of different parity and scales linearly with the magnetic field strength B.

The resulting trapping potentials under cryogenic conditions for OH in the $X^2\Pi_{3/2}$, $M_J = 3/2$ ground state are shown in fig. 2.4.2, where the coordinate system from fig. 2.4.3 applies. In contrast to the X- and Z coordinate which are plotted well beyond the borders of the magnet, the Y coordinate is only plotted between the magnets. As the magnets have different extent along X and Z, the potentials are not symmetric in the XZ-plane. As a result trap depths along the X, Y and Z axes of 0.20 K (13.9 m/s), 0.47 K (21.7 m/s) and 0.19 K (13.3 m/s) are achieved.

2.4.2 The Design

The geometry of the neutral trap including a last deceleration stage was set by the numerical optimizations by Dominik Haas [105, 116]. In brief, Monte Carlo trajectory simulations were performed in which some experimental parameters such as phase angle and voltages on the electrodes were treated as optimization parameters. The resulting optimized geometry is illustrated in fig. 2.4.3 and the optimized experimental parameters with their trap-loading efficiencies are shown in tab. 2.4.1. The final experimental parameters were limited by the high voltage restrictions in the developed setup. The loading efficiency is defined as the fraction of molecules remaining in the trap after 0.1 s relative to the number of phase-space stable molecules leaving the decelerator.

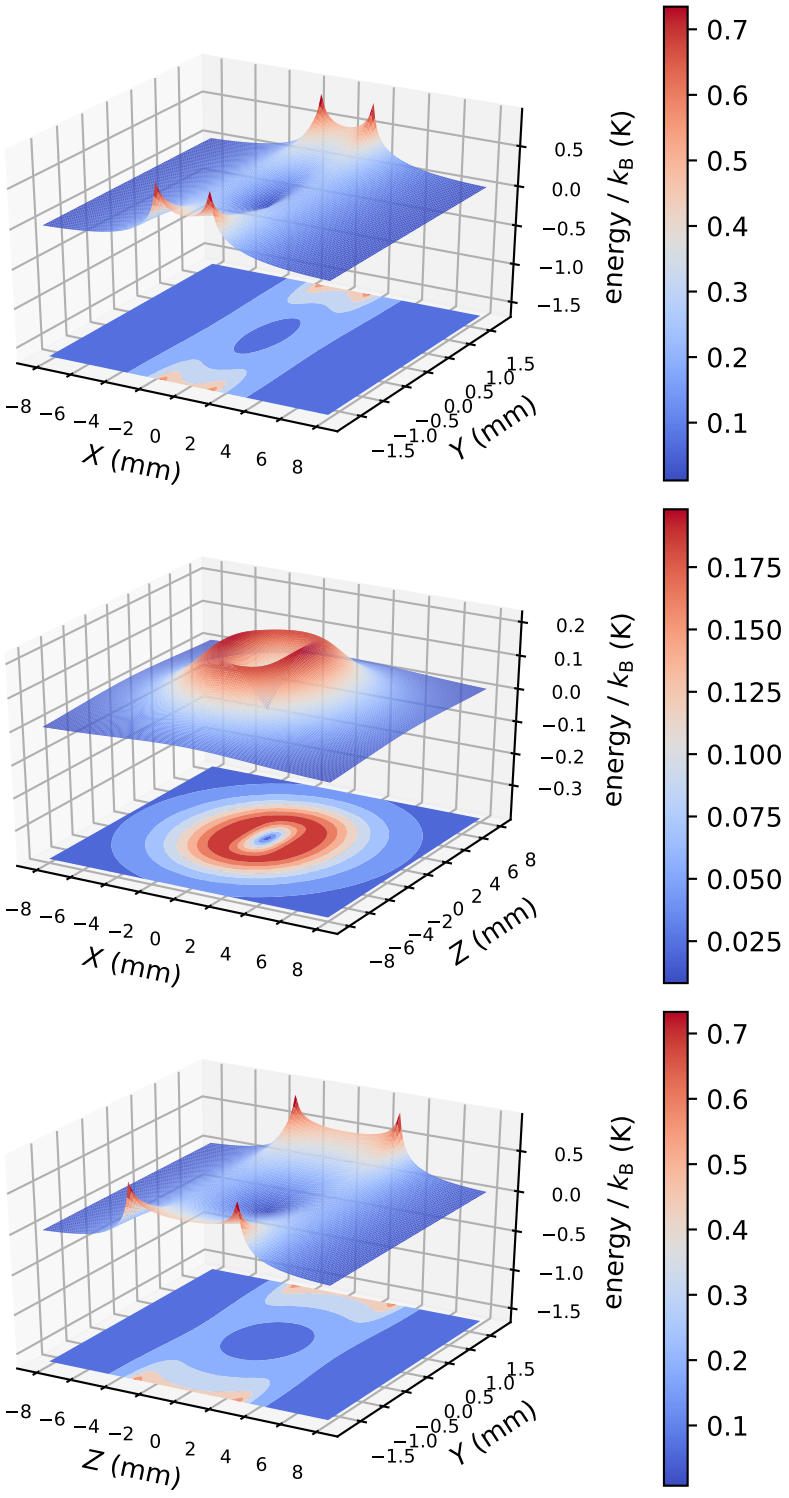

Fig. 2.4.2: **Trap Potentials for OH.** Trap potentials for OH in the $X^2\Pi_{3/2}$, $M_J = 3/2$ state, produced by the bar magnets with a remanence of 1.64 T. The coordinate system from fig. 2.4.3 applies.

The optimization procedure is based on a mesh-adaptive search algorithm [117, 118] and is described in the PhD thesis of Dominik Haas [105] and in [116]. This design includes a last deceleration stage consisting of the bar magnets and four wires as shown in fig. 2.4.3. The latter allows one to shape the stopping potential. These wires are arranged in a quadratic configuration with center-to-center distances of 2.0 mm. To produce a stopping pulse, a voltage V_f of 2.3 kV is applied to the front wires and a voltage V_r of 5.8 kV is applied to the rear wires as well as the bar magnets. The voltages were limited by the small size of the geometry and imperfections on the electrodes, which will be discussed later in this section.
Similar trap designs have been reported in [73, 111, 112]. A major advantage of this setup is the possibility of shaping the stopping potentials with more degrees of freedom as in e.g. [111]. This allows for loading the trap with molecules at higher velocities, since the final deceleration step occurs in close proximity to the trap center [75, 111]. Furthermore, using bar magnets instead of e.g. ring magnets allows the trap center to be closer to the decelerator.

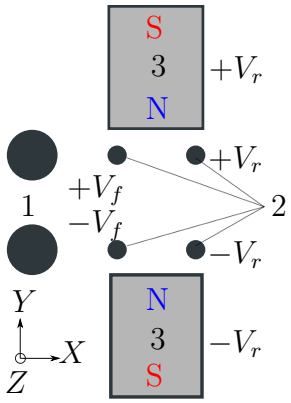

Fig. 2.4.3: **Schematic of the Magnetic Trap.** Illustration of the neutral trap showing 1: the last stage of the Stark decelerator, 2: the stopping wires and 3: the permanent bar magnets. The voltages are V_f for voltage on the front wires and V_r for voltage rear which is applied to the rear wires and the two bar magnets. The stopping wires are arranged in quadratic configuration with center to center distances of 2.0 mm and the magnets are spaced by 3.6 mm. The voltage V_f is 2.3 kV and V_r is 5.8 kV. The coordinate system originates in the center of the four wires (2).

Fig. 2.4.4 **a)** shows the stopping potentials expressed as Stark energies for OH in the $X^2\Pi_{3/2}$ ($J = 3/2$, $M_J = \pm 3/2$, f) state, obtained from eq. (2.3.12). This Stark energy shift allows the removal of a maximum energy of 0.76 cm^{-1} in the longitudinal direction along the center line through the trap ($y, z = 0$) using the experimental parameters set out in tab. 2.4.1. The Zeeman trapping potential E_Zm,

Tab. 2.4.1: Optimized loading efficiencies at room temperature with a remanece of the bar magnets of 1.4 T. V_r denotes the voltage applied to the magnets and the rear wires, V_f is the voltage on the front wires, phase ϕ (°) is the phase angle which was used to achieve the best efficiency and v_decel is the corresponding final velocity after Stark deceleration.

optimization range (kV)	V_r (kV)	V_f (kV)	phase ϕ (°)	v_decel (m/s)	efficiency (%)
10.5–9.5	10.5	4.4	55.276	38.2	16.8
9.5–8.5	9.4	4.1	55.309	36.6	15.7
8.5–7.5	8.2	3.4	55.371	33.7	14.9
7.5–6.5	7.4	2.9	55.412	31.8	13.4
6.5–5.5	6.5	1.9	55.452	29.7	11.7
experiment	5.8	2.3	55.468	28.8	9.9

given by eq. 2.4.3, for OH in the $X^2\Pi_{3/2}$ ($J = 3/2,\ M_J = +3/2,\ f$) state in between the two 1.64 T PrFeB magnets is shown in Fig. 2.4.4 **b)**.

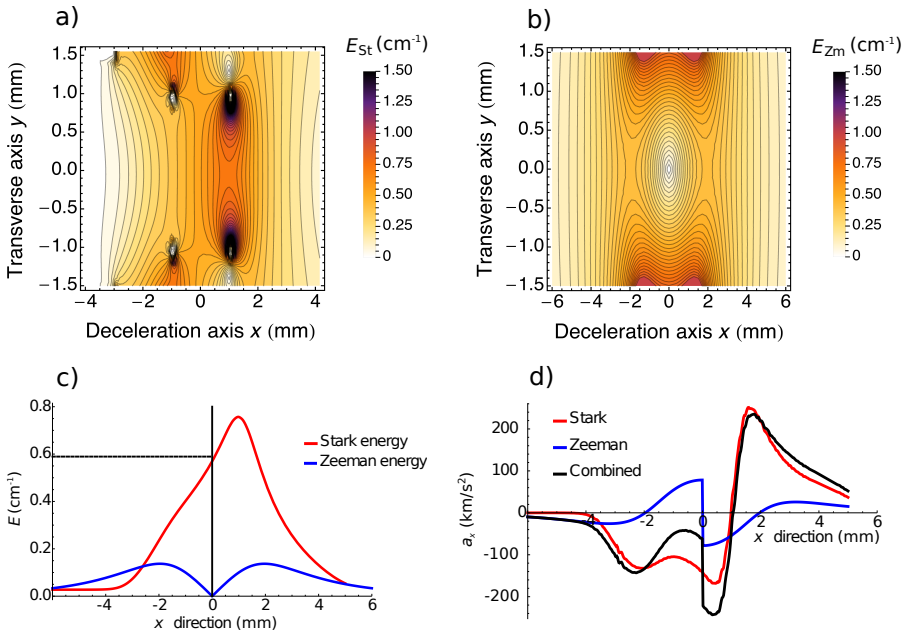

Fig. 2.4.4: **Stopping and Trapping Potentials. a)** Stark energies E_St for OH in the $J = 3/2,\ M_J = \pm 3/2,\ f$ state resulting from applying an electric potential of ±5.8 kV on the bar magnets and the rear stopping wires. The stopping wires closer to the decelerator exit are kept at ±2.3 kV. **b)** Zeeman energies E_Zm for OH in the $J = 3/2,\ M_J = +3/2,\ f$ state assuming a remanence of the permanent magnets of 1.64 T. **c)** Stark/Zeeman energy profile along the stopping direction ($y, z = 0$). The black vertical bar represents the trap center and the horizontal dashed line corresponds to the kinetic energy of the synchronous molecule at the decelerator exit. **d)** Longitudinal acceleration a_x for OH molecules according to the Stark and Zeeman energies from **c)**. All distances are given relative to the trap center. The Figure was reproduced from ref. [116].

2.4.3 Application of High Voltages

When designing a high voltage application in vacuum, the most important factors other than cleanliness are the choice of the materials for the insulators as well as the geometry of electrodes and insulators. A sub-optimal design can lead to several failures such as voltage breakdown or vacuum breakdown where in both cases the breakdown can permanently damage the electrodes or insulators [119, 120]. This subsection discusses some of the phenomena which can lead to failure and concludes with the impact on our design.

2.4.3.1 Voltage Breakdown

Voltage breakdown is the phenomenon when an electrical insulator becomes conductive by applying a high voltage. The minimum electric field to achieve this state is known as the dielectric strength. In order to apply high voltages, the electrodes are separated by insulators such as ceramics and have to be spaced at sufficient distances. A breakdown of the voltage can occur along the surface or through the material. Reasons for breakdown may be deposits of conductive surface films on the insulators or accumulation of surface charges. When testing prototypes of our trap, we have seen breakdown along surfaces as bright glows. Good vacuum conditions and thorough cleaning of the assembly may help prevent a formation of conducting films but breakdown through accumulation of surface charge can only be prevented by the right choice of material and geometry. Tab. 2.4.2 summarizes some of the properties of the insulator materials we chose. We expect electric fields of 3 kV mm^{-1} in our setup. The smallest parts were the wire holders for high voltage applications and were built of Macor®. The bigger parts were made of either AlN or Shapal™due to their high thermal conductivity, where the latter is much easier to manufacture. Generally, one should avoid gaps between the surfaces to allow for a

Tab. 2.4.2: Summary of some insulator materials showing their dielectric strength for AC and DC as well as their thermal conductivity. We expect electric fields of 3 kV mm^{-1} in our setup.

	Macor®	AlN	Shapal™	Al_2O_3
Diel. str. ac (kV mm^{-1})	45	17	-	16.7
Diel. str. dc (kV mm^{-1})	129	-	65	-
Thermal conductivity (W/mK)	1.46	140-180	92	18
References	[121]	[122]	[123]	[124]

uniform field throughout the body of the insulator [119]. When developing our high

voltage setup, our biggest problems were surface flashovers. These are primarily initiated by field emission from the cathode triple junction, the junction between vacuum, insulator and cathode. It has been shown that the shape of the insulators has a strong effect on surface flashover. For example, the poorest insulator performance is found in cones with slight negative angles from cathode to anode [125]. The most generally accepted mechanism for a surface flashover is the secondary electron emission avalanche (SEEA). Some electrons are emitted from the triple junction and produce secondary electrons on the surface of the insulator. These can produce even more electrons which will develop a SEEA [126].

2.4.3.2 Vacuum Breakdown

Vacuum is one of the best insulators. If the potential difference between two electrodes in vacuum exceeds a certain threshold, a transition in the vacuum from almost perfect insulation to almost perfect conduction occurs, which is known as vacuum breakdown leading to destructive arcing. Similar to the case of voltage breakdown, there must be a source of initiatory electrons or ions in the inter-electrode space or at their surface. Furthermore, there has to be an amplifying mechanism leading to an increase of electrons under the influence of the applied electric field leading to a growth in current. One can categorize the breakdown conditions in two classes. The first would be insufficient outgassing with pressures of 10^{-6} mbar and electric fields on the order of 1 to 10 kV mm^{-1}. The second class is a breakdown under almost perfect vacuum conditions, around 10^{-12} mbar, and high purity of the electrodes where electric fields above 10^{3} kV mm^{-1} can be applied before breakdown. As in the case of voltage breakdown, the electron emission from the cathode is the initiatory process [120]. In our case, we have typical working conditions of 10^{-11} to 10^{-7} mbar and apply electric fields of around 3.2 kV mm^{-1}. Hence, vacuum breakdown is in our case a smaller problem than surface flashover.

2.4.4 High Voltage Testing: Prototype

The high voltages on the stopping electrodes in the trap were switched using two fast MOSFET push-pull switches (HTS 301-03-GSM, HFB, Behlke Power Electronics) backed by two 0.5 µF capacitors (PPR200-504, Hivolt Capacitors Ltd.).[2]
When developing the last stopping stage for the neutral molecules where high electric fields (3 kV mm^{-1}) are applied, we first started with a simple design. Four wires were held by one polyetheretherketone (PEEK) part. A dielectric breakdown already occured at voltages of ±3 kV. We therefore decided to use Macor®as an insulator material instead, since it possesses a higher dielectric strength (129 kV mm^{-1} vs 23 kV mm^{-1}). Furthermore, the single holder was divided such that each pair of wires with same polarity is held by separate holders and spanned over ceramics ferrules (10)(zirconia). This first modification of the setup is shown in fig. 2.4.5. In fig. 2.4.3 the top pair of wires (1, 2) in fig. 2.4.5 with the same polarity is held by the holders (7). Wires (3) and (4) are retained with the holders (8). The magnets (5) and (6) are fixed in adapters made from stainless steel using screws. The stainless steel holders are pushed onto the magnet holder (9) by taking advantage of the repulsive force between the magnets. The voltages applied, when comparing to fig. 2.4.3, are given

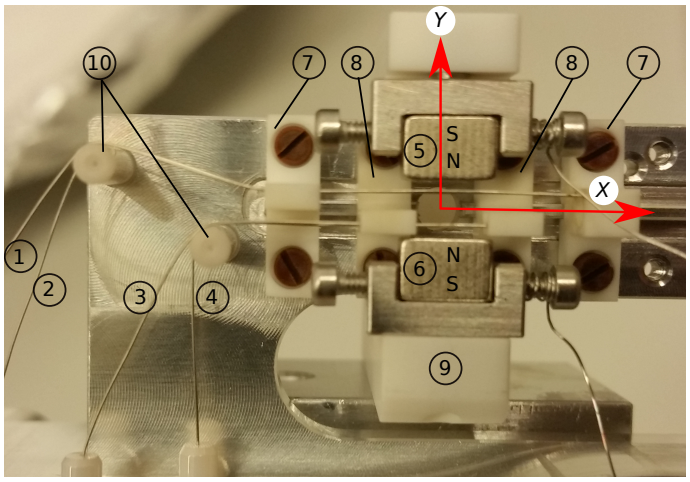

Fig. 2.4.5: **First Prototype.** Each pair of wires with same polarity is held by separate holders. In fig. 2.4.3 the top pair of wires (1,2) with the same polarity is held by the holders (7). Wires (3) and (4) are retained with the holders (8). The magnets (5) and (6) are fixed in adapters made from stainless steel using screws. The stainless steel holders are pushed onto the magnet holder (9) by taking advantage of the repulsive force between the magnets.

in table 2.4.3. Holding the wires of same polarity with separate holders increased the

[2]The high voltage-switching electronics used throughout this thesis are explained in [105].

Tab. 2.4.3: Voltages which are applied to the electrodes in fig. 2.4.5.

voltages	labels
V_f	(1)
$-V_\mathrm{f}$	(3)
V_r	(2), (5)
$-V_\mathrm{r}$	(4), (6)

surface distance over insulators from the closest electrodes with opposite polarity by a factor of 2. With electrical conditioning this prototype, we were able to reach the desired voltages of ±2.3 kV on the front wires (1, 3 in fig. 2.4.5) and ±5.8 kV on the back wires (2, 4 in fig. 2.4.5). However after a few days of operation, the insulators broke down. The problem however was not in the trap region anymore, but was shifted to the mounting of the wires, i.e. the ceramics ferrules (10).
The experience gained from this prototype lead to the development of the final setup which is discussed in the next section.

2.4.5 Final Magnetic Trap High Voltage Setup

The mechanism of breakdown in high voltage applications as described so far have finally influenced our design of the neutral trap including the last decelerator stage, i. e. the four stopping wires. Fig. 2.4.6 shows a technical drawing of the high voltage part and the magnetic trap. To minimize the electric field inside the insulators, we decided to hold the wires with opposite polarity in separate holders: the holders (4) for the bottom wires and holders (5) for the top ones. These holders (4 & 5) were made from Macor®due to its excellent dielectric strength (see tab. 2.4.2) to withstand the big differences in voltage. To span the wires, they were fixed with a knot at their right end and spanned over through holes in item (6). Item (6) was a solid assembly made of Shapal™, which ensures a large surface distance between the electrodes and from the electrodes to the copper body and the material allows for an efficient cooling. The magnet holder (7) was very bulky and was made from AlN (Ceramdis) for efficient cooling. The magnets (3) were placed in a stainless steel holder and were held in place simply by their magnetic repulsion. The high voltage for the magnets was supplied using a thin cable across the holder (7) and through the bottom of the base to the stainless steel magnet holders.
For measurement purposes, a LIF collection lens (8) was used (f = 6 mm). All high voltage cables were connected via Kapton-insulated cables, which can hold up to 30 kV DC (Vacom), to the electrical feedthroughs on the vacuum chamber.

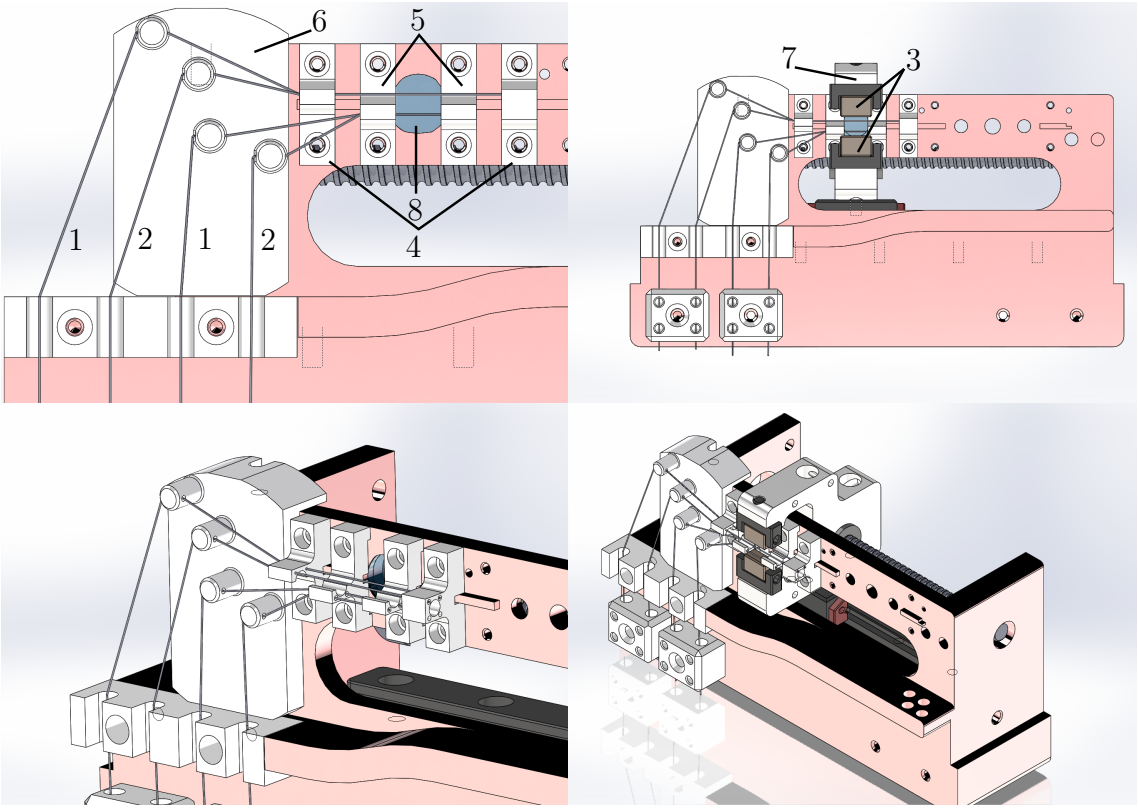

Fig. 2.4.6: **Neutral Trap Setup.** High voltages are applied to the front (1) and rear (2) wires as well as the trap magnets (3). The stopping wires are held using holders (4) and (5) as well as (6). (7) is the magnet holder and (8) a LIF collection lens.

2.5 Cryogenic Setup

To measure collisions of slow reactions, long interactions times between the ionic and neutral species are required. Trapping atomic and molecular ions as well as neutral atoms on timescales of minutes has already been demonstrated [26, 40, 41, 127] but trapping neutral molecules is a bigger challenge. Due to the additional degrees of freedom, it is difficult to find suitable molecular candidates for cooling and trapping. Another challenge is to achieve long trapping times.

The two strongest trapping-time-limiting mechanisms in our case are pumping into untrappable states due to interaction with ambient black-body-radiation (BBR) and collisions with background gas [35]. In order to reduce the effect of BBR on our trapping-times, the trap was enclosed in a two-layer cryogenic shield cooled by a closed-cycle refrigerator. The cold head of the refrigerator was suspended from a spring-loaded assembly and connected to the cryogenic shield with copper braids in order to isolate the trap from vibrations. Temperatures of 17 K at the inner shield

and of 53 K at the outer shield were thus obtained.
However, the trapped molecules will not be shielded completely from the room temperature BBR as we need laser access and the Stark-decelerated molecules need to be able to enter the trap. Additionally we need to be able to collect photons from the trap for LIF detection. This means our trap environment cannot be completely shielded from BBR but will be exposed to room-temperature BBR. This eventually leads to a trade-off between collection efficiency and room-temperature BBR shielding.
We have developed a model to estimate these effects which allowed to determine the size and positions of the apertures in the cryogenic shields. This section discusses the overall cryogenic design and will explain the model and connect the results to our final setup.

2.5.1 Cryo-Cooler and Connection to the Setup

In order to remove heat from the trap and reach ambient temperatures of 17 K, we used a two-stage closed-cycle refrigerator consisting of a cold head (DE-204SL, Sumitomo) with a helium compressor (HC-4E1, Sumitomo). The two-stage cold head had a cooling capacity of 16.2 W at a temperature of 80 K on the first stage and a cooling capacity of 3.0 W at 10 K on the second stage. The first step was designing the connection of the cryo head to some base for the trapping environment. Figure 2.5.1 shows a picture of the cryogenic setup.

Due to spatial limitations we chose six copper braidings (Rotima) with a total cross section of 48 mm^2 per stage. The first stage of the cryo-cooler was connected via copper braidings (1) to the first stage (53 K) adapter (2), which is connected to a feedthrough with XYZ-translation stage via an aluminium adapter (3). The second stage (17 K) was connected via adapter (4) and copper braidings (5) and the second stage adapter (6) to the second stage base (7). The second stage trap region was covered by copper shields (8) with apertures for laser access and loading of the traps.
The first and second stages were connected via PEEK spacers (96 mm^2 total cross section) to ensure minimal heat flow between these stages. In the cryogenic assembly, indium foil was clamped between larger interfaces to ensure optimal thermal conduction. Fig. 2.5.2 shows the temperature over time after switching on the cryo-cooler. The black curve shows the temperature of the outer cryogenic shield, measured on the first stage base (2), and the red curve shows the temperature of the inner cryo-

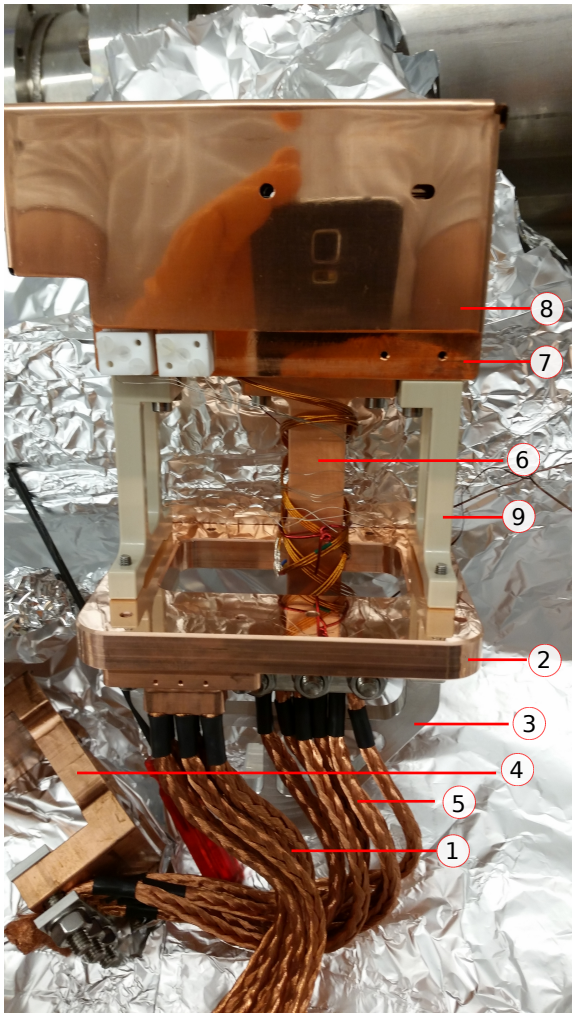

Fig. 2.5.1: **Cryogenic Assembly.** The first stage of the cryo-cooler was connected via copper braidings (1) to the first stage (53 K) adapter (2), which was connected to a feedthrough with XYZ-translation stage via an aluminium adapter (3). The second stage (17 K) was connected via adapter (4) and copper braidings (5) via the second stage adapter (6) to the second stage base (7). The second stage trap region was covered by copper shields (8) with apertures for laser access and loading of the traps. The first and second stages are held together by PEEK spacers to ensure minimal heat flow between these stages.

genic shield and the trap assembly, measured on the second stage base (7). Both temperatures were recorded using silicon diodes (DT-670B-CU, Lakeshore). The final temperatures were on the order of 53 K on the outer and 17 K on the inner stage, usually achieved within 12 hours. The complete cryogenic assembly was covered by another copper shield, connected to the first stage base plate (2). During this process, the pressures in the trap chamber decreased from around 1×10^{-8} mbar down to $< 1 \times 10^{-10}$ mbar.

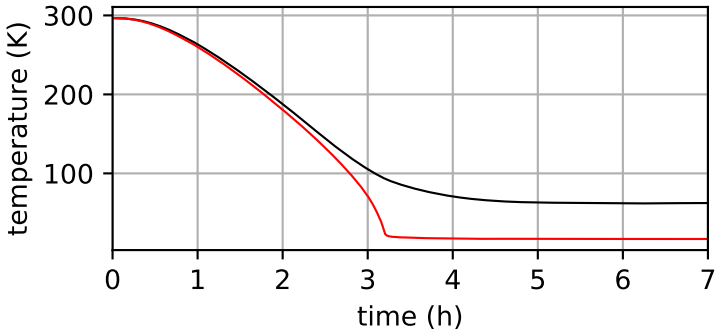

Fig. 2.5.2: **Cooling of the Assembly.** The temperature after starting the cryocooler was recorded. The black curve shows the temperature of the outer cryogenic shield and the red curve the temperature of the inner cryogenic shield and the trap assembly. The final temperatures were on the order of 53 K on the outer and 17 K on the inner stage, usually achieved within 12 hours.

2.5.2 Radiative Loss through BBR Pumping

In order to estimate the effect of pumping the OH molecules out of the trappable states on the trapping-times, we start by modeling an effective spectral density of BBR and continue by developing a rate equation model.

2.5.2.1 Effective Spectral Energy Density of BBR

The trap has three different temperature stages: the inner stage, the outer stage and ambient room temperature. The inner stage consists of the magnetic trap setup as shown in fig.2.4.6 with the cryogenic shields. The outer stage consists of the outer cryogenic shields. We assume that we have three temperatures T_{inner} or T_3, T_{outer} or T_2 and T_{rt} or T_1 for inner stage, outer stage and room temperature which amounted to about 17 K, 53 K and 295 K. The spectral energy density of BBR $\rho(\nu, T)$ emitted by these stages is described by

$$\rho(\nu, T) = \frac{8\pi h\nu^3}{c^3} \frac{1}{\mathrm{e}^{h\nu/k_\mathrm{B}T} - 1} \,, \tag{2.5.1}$$

where ν is the frequency of the light and T is the temperature of the emitting body. The final effective spectral energy density of BBR in the trap volume is modeled as a linear combination of the BBR intensities from each temperature stage, weighted by their solid angle contribution c_{T_i} that illuminates a cloud of molecules in the

center of the trap:

$$\rho_{\text{eff},T_1,T_2,T_3}(\nu) = \sum_{i=1}^{3} c_{T_i} \rho(\nu, T_i) \ , \tag{2.5.2}$$

where $T_{1,2,3}$ are the temperatures of the three stages. To calculate the solid angles we start with the opening angle. Fig. 2.5.3 illustrates the definition of the opening angle in our case. Solid angle contribution from room temperature BBR is limited by r_1, the radius of aperture 1 in the figure and the radius of the molecule cloud in the trap r_c. We have several apertures at each stage, all assumed to be circular, so for aperture j, the solid angle $\Omega_{1,j}$ for one opening for room temperature is given by

$$\Omega_{1,j} = 2\pi \left(1 - \cos(\theta_{1,j})\right) = 2\pi \left(1 - \frac{d_{1,j} \frac{1}{1+\frac{r_c}{r_{1,j}}}}{\sqrt{r_{1,j}^2 + \left(\frac{d_{1,j}}{1+\frac{r_c}{r_{1,j}}}\right)^2}} \right) \ . \tag{2.5.3}$$

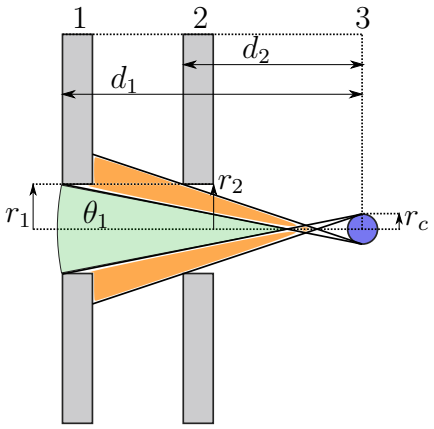

Fig. 2.5.3: **Definition of the Opening Angle.** The opening angle θ_1 is limited by the radii of two apertures r_1 and r_c and their distance d_1. The green area shows the contribution of room temperature illuminating the molecule cloud and the orange area shows the contribution of the outer cryogenic shield (1). Aperture (2) is the inner cryogenic shield and (3) is the molecule cloud. All the apertures are circular.

For the temperature stage 2, which is the outer cryogenic shield, we calculate the solid angle in an analogous way but subtract the solid angle of the room temperature part as illustrated in fig. 2.5.3 by the orange area. Subsequently, the solid angle contribution for stages 1 and 2 are calculated by summing up the solid angle for all

apertures and dividing by 4π which is the solid angle of a full sphere:

$$c_{T_i} = \frac{1}{4\pi} \sum_j \Omega_{i,j} \tag{2.5.4}$$

Finally, the solid angle contribution c_{T_3} of the inner cryogenic assembly is simply the residual, meaning

$$c_{T_3} = 1 - (c_{T_1} + c_{T_2}) \ . \tag{2.5.5}$$

The effective spectral energy density of BBR was calculated according to eq. 2.5.2 with the BBR spectral energy densities of the three temperature stages, scaled by their solid angle contributions. The resulting spectral energy densities are shown in fig. 2.5.4. Since the room temperature BBR has by far the highest spectral energy density over all frequencies of interest, it mostly determines the shape of the effective BBR curve. From the figure we also see that the spectral energy densities are high at frequencies where one can expect rotational transitions ($\Delta J = +1$) and transitions between the two different spin-orbit manifolds $\Delta F = +1$. The apertures in the cryogenic shields which allowed loading of the trap with decelerated molecular beam and their detection had a radius of 2.5 mm and the molecule cloud had an estimated radius of 0.67 mm which was determined from trajectory simulations. The apertures for the detection laser access had a radius of 1.0 mm. This leads to a total of $c_{T_1} = 7.15\%$, $c_{T_2} = 4.40\%$ and $c_{T_3} = 88.4\%$. We initially aimed for all radii in the cryogenic shields to be 1.0 mm, which would have resulted in $c_{T_1} = 2.25\%$, $c_{T_2} = 1.68\%$ and $c_{T_3} = 96.1\%$. This would have increased the BBR limited lifetime of the OH radicals in the trap by almost a factor of 4. We were, however, limited by low LIF signals, leading to a compromise between signal strength and BBR shielding. The real illumination of the trapped cloud, however, will be higher as this model assumes that photons hitting the surface of the cryogenic assembly will not be reflected by the copper surface.

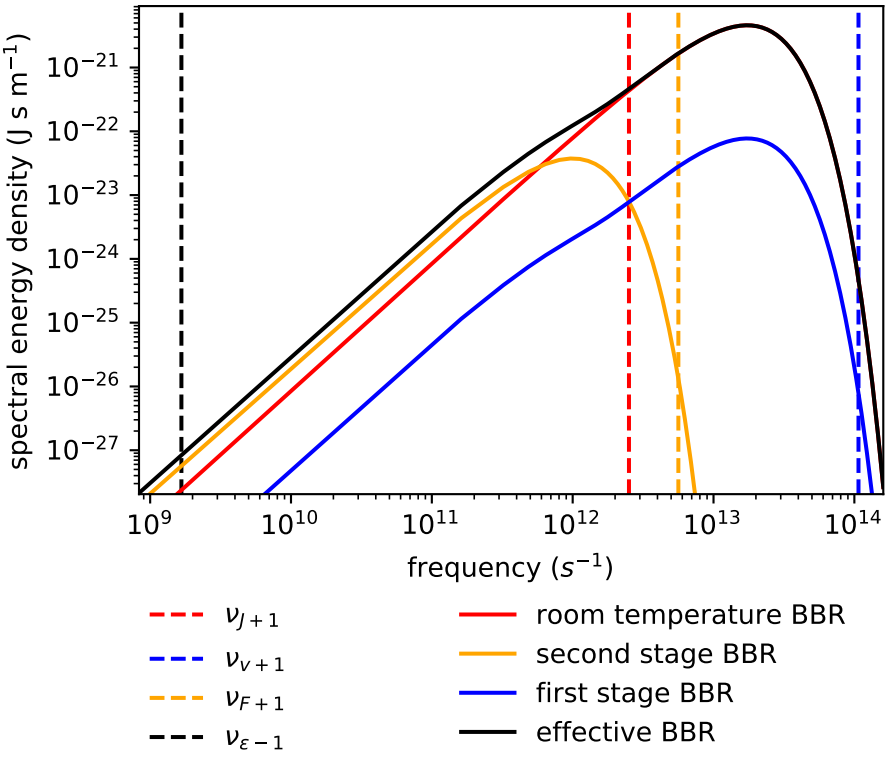

Fig. 2.5.4: **Effective Spectral Energy Density of BBR.** The effective spectral energy density intensity of BBR is shown as black solid line. The separate BBR spectral energy densities multiplied by the solid angle contribution c_{Ti} are shown for room temperature (solid red), the second stage of the decelerator (aperture (1) in fig. 2.5.3) in solid orange and for the first stage of the decelerator (aperture (2) in fig. 2.5.3) in solid blue. Additionally, transitions from the $|v = 0, J = 3/2, F = 1, M_J = 3/2, p = f\rangle$ ground state are indicated by dashed lines: $\epsilon = -1$ in black, $\Delta J = +1$ in red, $\Delta F = +1$ in orange and $\Delta v = +1$ in blue. The solid angle contributions were $c_{T_1} = 7.15\%$, $c_{T_2} = 4.40\%$ and $c_{T_3} = 88.4\%$.

2.5.2.2 Rate Equation Model

Using the effective spectral energy density of BBR, we set up a system of rate equations. We follow the Einstein rate equation model which allows three pumping mechanisms. The first mechanism is the absorption of a photon which leads to a change of population according to

$$\frac{\mathrm{d}n_1}{\mathrm{d}t} = -B_{12}\rho(\nu_{12})n_1 \tag{2.5.6}$$

where n_1 is the population of the energetically lower level, B_{12} is the Einstein coefficient for absorption and $\rho(\nu_{12})$ is the spectral energy density of BBR at the frequency of the transition. In the case of a two level system, we would have $\frac{\mathrm{d}n_2}{\mathrm{d}t} = -\frac{\mathrm{d}n_1}{\mathrm{d}t}$ if

the total population $n = n_1 + n_2$ has to be constant. The second mechanism is the opposite of absorption which would be the stimulated emission of a photon by another photon, described by

$$\frac{\mathrm{d}n_1}{\mathrm{d}t} = B_{21}\rho(\nu_{12})n_2 \ , \tag{2.5.7}$$

where B_{21} is the Einstein coefficient for stimulated emission. Finally an absorbed photon can also be emitted spontaneously, independent of the light intensity, described by

$$\frac{\mathrm{d}n_1}{\mathrm{d}t} = A_{21}n_2 \ , \tag{2.5.8}$$

where A_{21} is the Einstein coefficient for spontaneous emission. For a two level system, this gives a change of population in the lower state 1 of

$$\frac{\mathrm{d}n_1}{\mathrm{d}t} = -B_{12}\rho(\nu_{12})n_1 + \left(A_{21} + B_{21}\rho(\nu_{12})\right) n_2 \ . \tag{2.5.9}$$

2.5.2.3 Einstein Coefficients

To estimate the rate of BBR-induced trap loss, we started with a population of 1.0 in our decelerated and trapped state $|v = 0, J = 3/2, F = 1, M_J = 3/2, p = f\rangle$. Because the radiative transitions occurred in the magnetic field of the trap, Zeeman-state resolved Einstein coefficients were required. To obtain these, we used the averaged Einstein A coefficients reported by Brooke et al. [128] in the $|v, J, F, p\rangle$ basis, where v is the vibrational quantum number, J is the total angular momentum quantum number and F are the mixed spin-orbit manifolds Ω, where F_1 is mostly $\Omega = 3/2$ and F_2 is mostly $\Omega = 1/2$. We calculated the transition dipole moments between two rotational states J and J' as

$$\langle J' | \, \mu \, | J \rangle = \sqrt{A_{J'J} \frac{3\epsilon_0 h c^3 (2J'+1)}{16\pi^3 \nu^3}}, \tag{2.5.10}$$

where ν is the transition frequency. We applied the Wigner-Eckhart theorem to calculate the transition moments between different Zeeman states as [129]

$$\langle J' M_J' | \, \mu \, | J M_J \rangle = (-1)^{(J' - M_{J'})} \sum_q \begin{pmatrix} J' & 1 & J \\ -M_J' & q & M_J \end{pmatrix} \langle J' | \, \mu \, | J \rangle \, . \tag{2.5.11}$$

From this result, we calculated the M_J-resolved Einstein $A_{J'M'_JJM_J}$ coefficients according to eq. (2.5.10) where the degeneracy factor $(2J'+1)$ can now be neglected. Further, the Einstein B coefficients were calculated as

$$B_{J'M'_JJM_J} = A_{J'M'_JJM_J} \frac{c^3}{8\pi h \nu^3_{J'M'_JJM_J}} \ . \tag{2.5.12}$$

2.5.2.4 Numerical Solution of the Rate Equations

The rate equations for the population n_i of the i-th energy level are formulated as

$$\frac{\mathrm{d}n_i}{\mathrm{d}t} = \sum_{j>i} \left(A_{ji} + B_{ji}\rho_{T_1,T_2,T_3}(\nu_{ji})\right) n_j - \left(B_{ij}\rho_{T_1,T_2,T_3}(\nu_{ji}) + Z\right) n_i \ , \tag{2.5.13}$$

where $E_i < E_j$ and Z is a loss rate such as a background collision rate. The system of rate equations is solved according to

$$\mathbf{n}(t+\Delta t) = \mathbf{n}(t) + \frac{\mathrm{d}\mathbf{n}}{\mathrm{d}t}\Delta t. \tag{2.5.14}$$

At room temperature, all pumping rates are below 2.6 s^{-1}, half of them below 6×10^{-3} s^{-1}. Since these are low rates, the time steps for the solution of the rate equations can be chosen on the order of 0.01 s to 0.1 s. To verify numerical convergence, the rate equations are solved for a loss-free case ($Z = 0$) and the solutions were checked against the requirement of conservation of population over time. For our application, convergence of the solution was found by including all M_J states for J values up to $J_{\max} = \frac{11}{2}$ in the vibrational ground state. Zeeman energy shifts were neglected. In the loss-free case at room temperature (295 K), the steady-state populations have to match to a Boltzmann-distribution at 295 K as shown in fig. 2.5.5. In the cryogenic case where we use an effective BBR intensity as a linear combination of three different temperature BBR distributions, one is attempted to assign an effective temperature by fitting the equilibrated populations with a thermal Boltzmann distribution. This leads to an effective temperature of 66 K in our case. However, as a linear combination of the BBR distributions can not be described by a BBR distribution of another temperature, this result should be treated with caution.

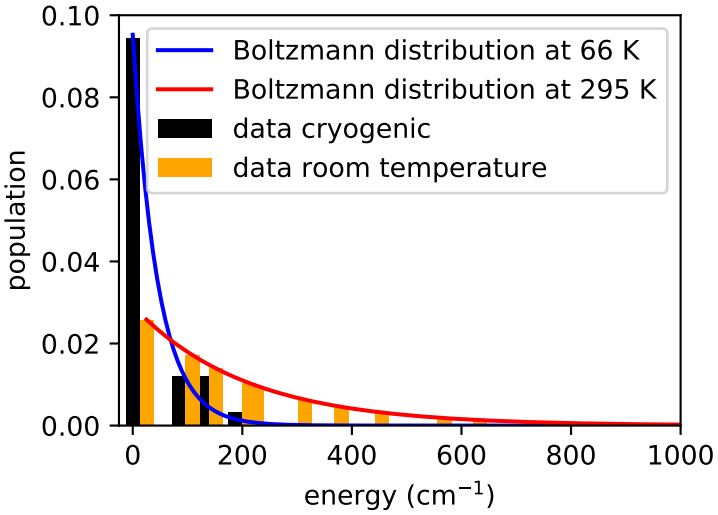

Fig. 2.5.5: **Populations.** The steady-state populations of the first few energy levels are shown for room temperature (orange data) and the cryogenic case (black data). In the room temperature case, these correspond exactly to a thermal Boltzmann distribution at 295 K (red line). In the cryogenic case in which we use an effective spectral energy density of BBR, it corresponds to a thermal distribution of 66(1) K (blue line).

2.5.2.5 Trap Loss: Results

With the rate equation model we can estimate the trap loss from our magnetic trap by radiative pumping of the states. Therefore, we consider all states with $m_J < 3/2$ as lost since most OH molecules with $M_J = 1/2$ can not be efficiently confined anymore due to their lower Zeeman shift. Furthermore, states with $M_J < 0$ are magnetic high-field seekers and can therefore not be confined in our magnetic trap. We introduce this effect simply by setting the populations of these states to zero in every time-step which is equivalent to a trap loss. Finally, we want to compare these loss rates to our experiment. We therefore look at the population of the states which are probed with our LIF-scheme, namely $|v = 0, J = 3/2, F = 1, M_J \geq 1/2\rangle$. The results for our trap are shown in fig. 2.5.6 where only the three most populated states are plotted. For the cryogenic case with temperatures of the three stages of 295 K, 53 K and 17 K we calculate a BBR-limited 1/e lifetime of 81.4 s. In the room temperature case we estimate a 1/e lifetime of 2.8 s, which is in agreement with the value calculated by Hoekstra *et al.* [35]. Finally, the dependence of the BBR-limited lifetimes in our setup on the radius of the apertures in the cryogenic shields for loading and detection of OH radicals is shown in fig. 2.5.7. The final radius of 2.5 mm leading to a lifetime of 81.4 s is indicated by the blue lines. The

black line shows the dependence of the BBR-limited lifetime on the radius of the apertures in the cryogenic shields. The red lines show the corresponding solid angle contributions c_{T_i}. A radius of 1.0 mm in the cryogenic shields would have increased the BBR limited lifetime by a factor of 4, but low signal levels were not allowing for such small radii.

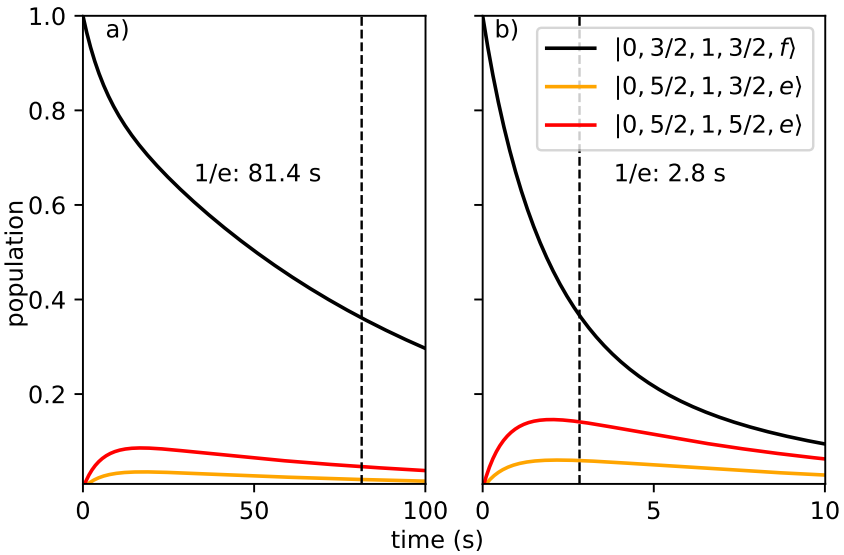

Fig. 2.5.6: **BBR Pumping.** Populations of the three most populated states in the $|v, J, F, M_J, p\rangle$ basis over time under **a)** cryogenic conditions and **b)** room temperature. The initially populated state was assumed to be $|0, 3/2, 1, 3/2, f\rangle$. The dashed lines indicate the 1/e lifetime for the sum of the states probed by LIF.

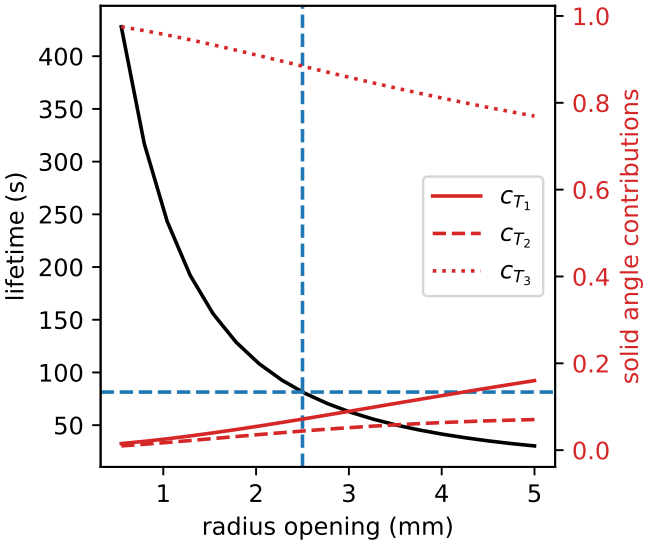

Fig. 2.5.7: **BBR Limited Lifetime vs. Aperture Radius in Cryogenic Shields.** The black line shows the dependence of the BBR-limited lifetime on the radius of the apertures in the cryogenic shields. The final case in our experiment is indicated by blue lines where we have a radius of 2.5 mm and a corresponding lifetime of 81.4 s. The red lines show the corresponding solid angle contributions c_{T_i} assumed all apertures have the same radii.

2.5.3 Cryogenic Setup: Thermal Contraction

In the context of the development of the cryogenic assembly, numerical solutions on the change of the geometry due to thermal contraction when cooling down from 295 K to 17 K were carried out. The main concern was the relative displacement of the magnetic-trap center to the center of the electric stopping potential. Therefore, a CAD drawing of a simplified version of the geometry in fig. 2.4.6 was constructed. The geometry was simplified in order to allow for converged numerical results. The complex copper body and stainless steel parts were replaced with simple blocks of the same materials. The thermal expansion coefficients which were used in this simulation are summarized in tab. 2.5.1.

Figure 2.5.8 shows the main result of these simulations. The color bar shows the magnitude of the displacement vectors of certain points in the setup in mm. Note that for the magnets, the material NdFeB instead of PrFeB was used.

The labels were chosen according to fig. 2.4.6 and are as follows: the magnets (3) held in the AlN part (7), the holders for the stopping wires (4) and (5), the Shapal™assembly (6) for spanning of the stopping wires and as addition holders for the ion trap (9). The stopping wires were neglected, as they are positioned by the

holders. As copper has a much larger thermal contraction than AlN, the magnets,

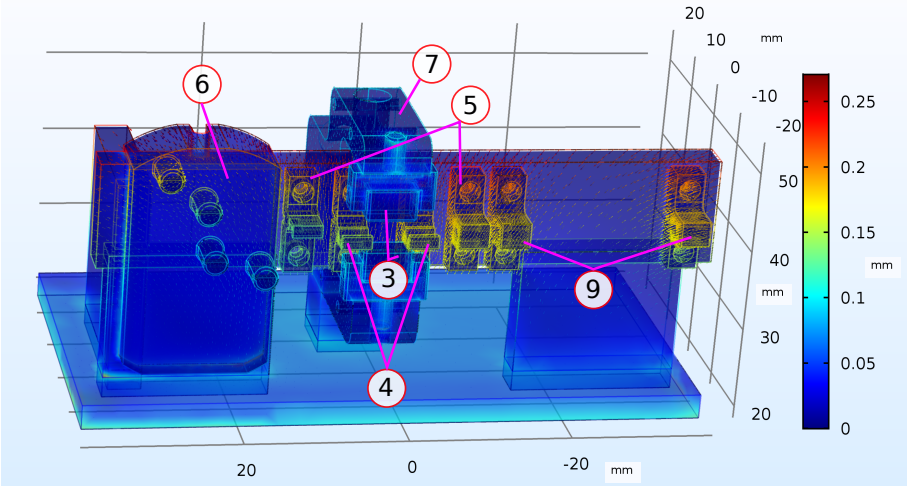

Fig. 2.5.8: **Deformation of the Cryogenic Assembly due to Thermal Contraction.** The labels are as follows: the magnets (3) held in the AlN part (7), the holders for the stopping wires (4) and (5), the Shapal™ part for spanning the stopping wires (6) and as addition holders for a future ion trap (9). The labels were chosen according to fig. 2.4.6.

Tab. 2.5.1: Thermal expansion coefficients used for the simulation are shown for different materials.

	Thermal expansion coefficient (10^6/K)	Source
Cu	17	[130]
NdFeB	3.4	[131]
Stainless steel	16.5	[132]
Macor®	7.4	[121]
Shapal™	4.5	[123]
AlN	4.5	[122]

which are held by a big AlN assembly are less displaced than the holders for the stopping wires on the large copper body. The difference in these displacement magnitudes comes directly from the difference in thermal expansion between copper and AlN. As the stopping wire assembly is on a large copper block, the displacement is larger than, for example, the displacement of the magnets which are placed on an assembly made of AlN.

Fig. 2.5.9 shows a histogram of the displacement magnitudes. It shows two distinct peaks at 0.08 mm and 0.17 mm. The latter is caused by the assembly of holders for stopping wires and ion trap (4, 5, 6 and 9 in fig. 2.5.8). The values of lower displacement are spread over the complete assembly. As the density of points is larger

in small parts of the geometry, such as the stopping wire holders, the magnitudes of the two peaks in the histogram are not meaningful. As a result we see that the relative displacement of the magnetic trap center and the center of the stopping wire assembly is on the order of 90 μm. As the mechanical tolerances for the parts in the assembly are on the same order (around 100 μm), this is in an acceptable range.

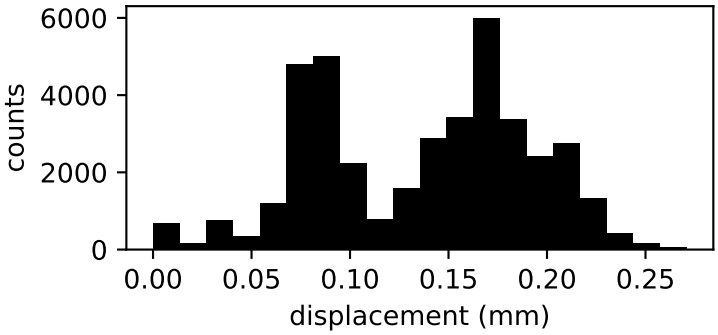

Fig. 2.5.9: **Histogram of the Displacement Magnitudes at 17 K.** There are two maxima at 0.8 mm and 1.7 mm. The latter corresponds to the displacements in the stopping wire assembly on the copper body (4, 5, 6 and 9 in fig. 2.5.8). The values of lower displacement are spread over the complete assembly.

2.5.4 Complete Experimental Setup

The complete experimental setup for the trapping experiments is shown in fig. 2.5.10. It is the same setup as for deceleration as shown in fig. 2.3.1, but the trap assembly is placed behind the decelerator with the trap center at the interaction point from fig. 2.3.1.

Pulsed beams of internally cold OH radicals were generated by the NPV with a DC-discharge unit (1). After passing through a skimmer (2), the molecules were decelerated from velocities of 425 m/s down to 29 m/s by a 124-stage Stark decelerator (3). The translationally cold molecules were loaded into a permanent magnetic trap by applying high voltages to the bar magnets and stopping wires acting as a last deceleration stage. The whole trap assembly (7) was mounted on a feedthrough with a XYZ-translation stage (6) for fine adjustment of its position. Trapped molecules were detected by LIF collected by a lens onto onto a photomultiplier tube (PMT) (5). The trap region was shielded from stray light using light baffles (4). The blue line shows the laser axis (8) of the detection laser.

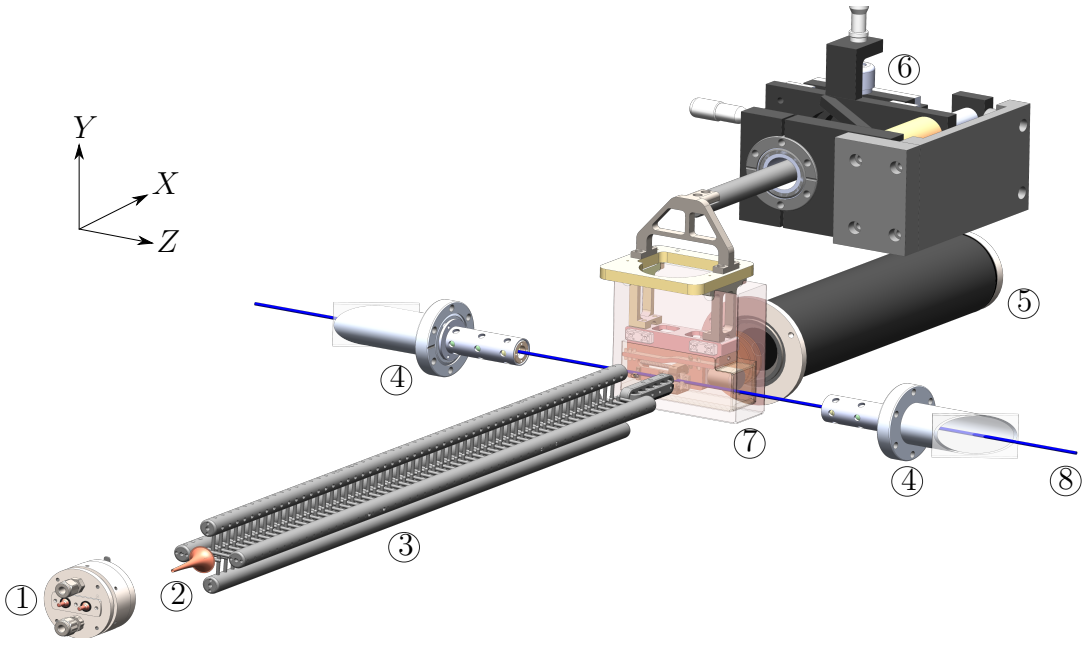

Fig. 2.5.10: **Experimental Setup for Trapping of OH molecules.** Pulsed beams of internally cold OH radicals were generated by the NPV with a DC-discharge unit (1). After passing through a skimmer (2), the molecules were decelerated by a 124-stage Stark decelerator (3). The trap assembly (7) was mounted on a feedthrough with XYZ-translation stage (6). Trapped molecules were detected by LIF on a photomultiplier tube (PMT) (5). The trap region was shielded from stray light using light baffles (4). The blue line shows the laser axis (8).

2.6 Experimental Control

To allow a smooth operation in the lab environment, a modular multithreaded software with graphical user interface (GUI) was developed using python 3 and QT 5, called HyT-Control. A pulse sequence to control the whole experiment is defined in the GUI and given to a pulse generator card (Spincore, PB 12) with 12 programmable channels, 100 MHz clock frequency, PCIe connector, a minimum pulse length of 50 ns and a time resolution of 10 ns. The signal from the PMT is collected on a 600 MHz oscilloscope (LeCroy, WaveSurfer 64 MXs-B) and then read by our control software.

2.6.1 Main program: HyT Control

The main program is segmented into three threads: the main thread (GuiThread) which runs the GUI and gives control over experimental parameters, data storage and displays the latest measurement; a listener thread (ListenerThread) starts a measurement and listens for it to finish; the actual measurement thread (DelayScanThread) that programs the sequence, waits for the measurement to finish and acquires the data recorded on the oscilloscope. The attributes from GuiThread are inherited to ListenerThread and down to DelayScanThread.
This main program loads several self-made modules for control over different parts which will now be presented. Most of these modules are classes themselves and contain an example code, so they can be run alone for testing. The program reads an initialization file when starting up, where all experimental parameters can be initialized and then further be controlled via the GUI. Fig. 2.6.1 shows screenshots of the two main panels. The upper part shows the first panel, where the trigger sequence is determined. The lower picture shows the scan panel, where scan are setup and started, as well as monitored in the black panels on the right, where the data is plotted (not shown here).

2.6.1.1 Pulse Sequence

The sequences are put together from events defined for each channel. The easiest trigger event would be a single pulse of duration τ on channel m. Therefore we need to define two events: the beginning m_b and the end of the pulse m_e. If this would be the only channel we use, this sequence would be defined by setting the start time setting m_b to any time relative to some starting point T_0 and m_e to τ relative to

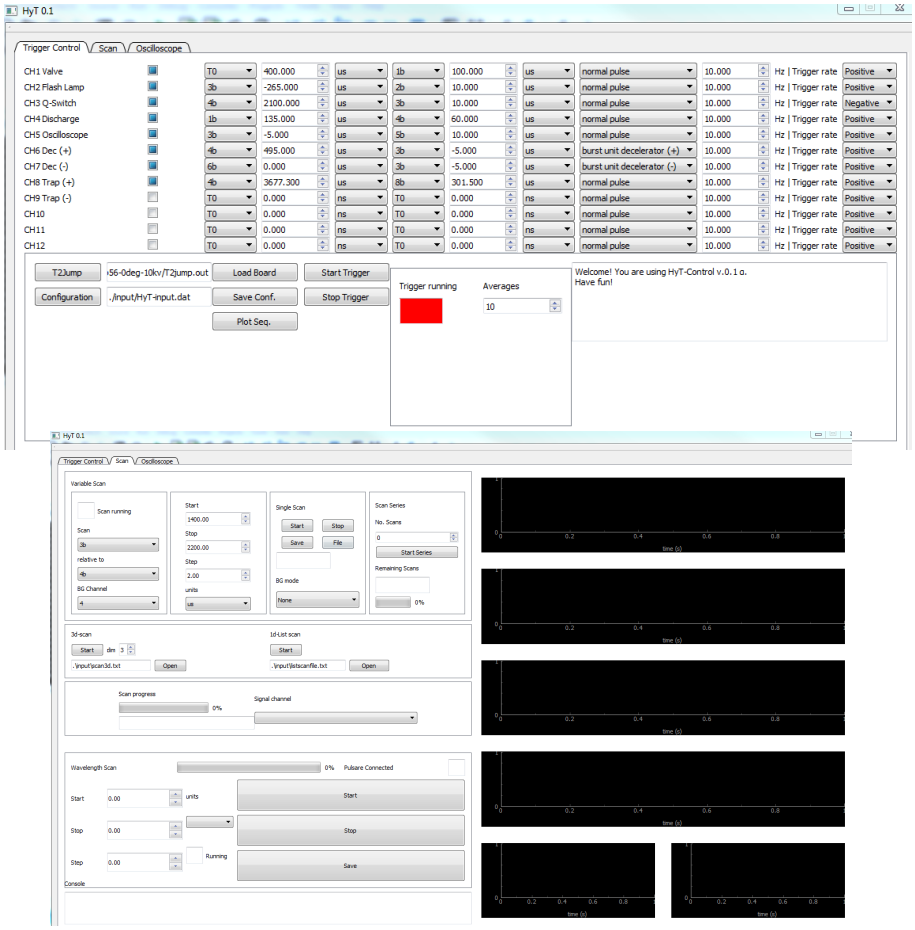

Fig. 2.6.1: **HyT Lab Control.** Screenshots of our lab control software. The upper part shows the first panel, where the trigger sequence is determined. The lower picture shows the scan panel, where scan are setup and started, as well as monitored in the black panels on the right, where the data is plotted.

m_b. If we want to operate the valve, the DC-discharge on the valve, the decelerator (2 channels), the laser (2 channels) and the oscilloscope (PMT is not triggered), we need 7 channels. Each Sequence starts with the valve trigger, which defines T_0 and is usually chosen as channel 1. With a pulse duration of 100 μs this defines the events 1_b and 1_e.

Next, one can define the discharge trigger on channel 2, which is usually around 135 μs after the valve trigger starts. Thus, one can define $2_b = 1_b + 135$ μs and so on. Figure 2.6.2 shows an example of a complete trigger sequence to measure the LIF of decelerated OH radicals. After the valve (1) and the DC-discharge (2) are triggered, the molecules are decelerated. In this particular example all 124 pulses (6, 7) (required for the 124 electrode pairs) are switched at a constant frequency of 42.7 kHz, which represent operation in guiding mode since all molecules require the same amount of time to travel from one module to the next. The guided velocity

in this case is 470 ms^{-1}. For detection, the laser is triggered first, which consists of a trigger for the Q-switch on the Nd:YAG laser (4) before the trigger for the laser itself (3). The oscilloscope (5) is triggered 5 μs before the laser (3).
The corresponding module is called *pulseseq* which contains the class *sequence* and an example code. Once an instance of the class is initialized, the function *seq* can be called to generate an output, stored in the class attribute *sequence.output*. The output is of the shape (2, number of events). The first row contains a string of zeros and ones, which stands for 0: low, 1: high. These are the output trigger voltages, where 0 is 0 V and 1 is 3.3 V.
The order of the digits corresponds to the order of the channels, e.g. '101' means: channel 1 high, channel 2 low, channel 1 high. The second row of the output contains the duration of this event in seconds. This is directly the format which is accepted by the functions as defined in the module *spinapi*, which is adapted from the version of reference [133]. The module contains various functions which use the dynamic link library *spinapi.dll* via the python module *ctypes*.

2.6.1.2 Delay Scans

The main goal of this program is the automation of our measurement process. Therefore, the DelayScanThread can create pulse sequences, where the settings of up to three channels can be changed in a 3d-grid. A 3d-grid was required, for example, for the optimization of the NPV, which changes its characteristics permanently. For a successful experiment is was essential to find good settings for the discharge delay and duration to produce an intense signal at desired velocity. The automation allows for overnight measurements. The optimal settings found during such a long scan can be used for the experiment during the day. An input file needs to be created for this purpose, where the event to be scanned, the event relative to which the delay is defined need to be given. Furthermore the first and last value for the grid, as well as the step size need to be defined in a structure as in the following example:

```
#Loop 1: discharge delay
#event, relative event, start value, stop value, step size
4b 1b 100e-6 130e-6 10e-6
#Loop 2: discharge duration
4e 4b 30e-6 80e-6 10e-6
#Loop 3: laser delay
```

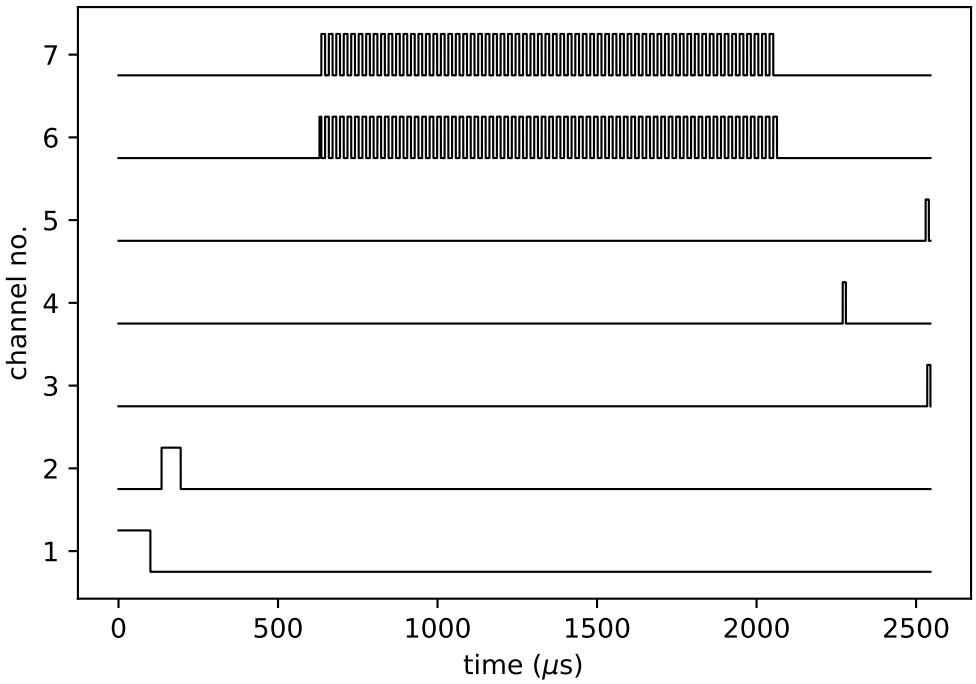

Fig. 2.6.2: **Pulse Sequence.** Shows an example of a complete trigger sequence. After the valve (1) and the DC-discharge (2) are triggered the molecules are decelerated. All 124 pulses (6, 7) (required for the 124 electrode pairs) are switched at a constant frequency of 42.7 kHz, which indicated a guiding mode since all molecules require the same amount of time to go from one module to the next. The guided velocity in this case is 470 ms^{-1}. For detection, the laser is triggered first, which consists of a trigger for the Q-switch on the Nd:YAG laser (4) before the trigger for the laser itself (3). The oscilloscope (5) is triggered 5 μs before the laser (3).

```
3b 4b 2050e-6 2180e-6 2e-6.
```

A line starting with # is regarded as comment. The outermost loop scans 4_b relative to 1_b from 100 μs to 130 μs in steps of 10 μs. The next loop defined is the middle loop and the third one the innermost loop. Optionally, the innermost loop can be replaced by an arbitrary list of values. This allows to measure values of interest such as the LIF of the undecelerated OH molecules. Fig. 2.6.3 shows an example of a 3d grid scan. The LIF-TOF signal was measured with a guiding sequence at 425 m/s (x-axis) for different discharge delays and discharge durations as shown in the example input file above. Each row in this plot corresponds to one integrated LIF-TOF measurement with a guiding sequence, representing the innermost loop in the example. It clearly shows the triple peak structure at delays of 2.09 ms, 2.12 ms and 2.15 ms. The y-axis shows the measurement number as tuples of (i,j) where i

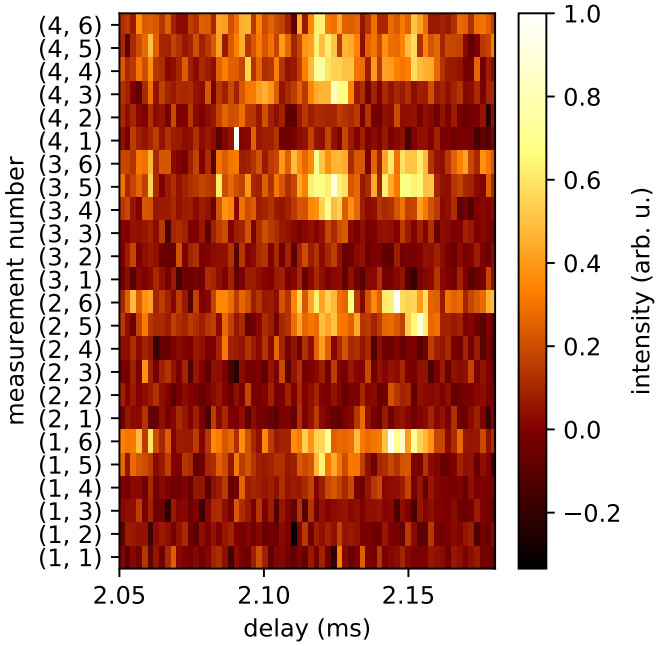

Fig. 2.6.3: **3d Grid Scan.** The LIF-TOF signal using a guiding sequence on the decelerator was measured for various discharge delays and durations of the discharge unit on the NPV in a 3d grid scan.

is the index in the outermost loop (loop 1) and j is the index in the middle loop (loop 2).

The measurement leading to the highest intensity is the measurement (2, 6), giving the best valve parameters for the delay after NPV trigger of the DC-discharge on the NPV of 110 μs and a DC-discharge pulse duration of 70 μs. The measurement leading to a maximal intensity gives us the parameters for the specific measurement.

2.7 Experimental Results

This section covers the experimental results which show long term trapping of OH radicals in a cryogenic magnetic trap. Since we measured the LIF of OH on the $A\ ^2\Sigma^+(v = 1) - X\ ^2\Pi(v = 1)$ transition (sec. 2.3.3), we did not end up in the vibrational ground state, therefore our detection method was destructive. This means that we had to repeat a complete experimental cycle to probe the population of trapped OH radicals at different delays after the onset of trapping. To measure a signal at 10 s means to have a repetition rate of 0.1 Hz. It was thus worth optimizing the LIF signal of trapped OH before starting a long term (a few days) trapping-time measurement. We start with the optimization of the trapping signal and conclude this section with measurements of the trapped OH population over time.

2.7.1 Trap Loading: Optimization

For optimizing the trapping signal, we had to focus mainly on two parameters: the start of the decelerator sequence (incoupling time) relative to the DC-discharge onset on the NPV and the switch-off time or the duration of the final stopping pulse in the trap. The switch-on timing of the stopping pulse was fixed at a delay such that the decelerated package experiences the complete duration of the pulse. As the phase space acceptance of the Stark decelerator decreases for lower final velocities (see sec. 2.3.2.2), already a slight mismatch of the incoming OH packet relative to the synchronous molecule leads to a decrease in density of decelerated molecules. At a velocity of 425 m/s a mismatch of 1 mm corresponds to 2.35 μs which is why the incoupling time is a very sensitive parameter.
For the optimization of the trap loading, the incoupling time was scanned first with a fixed duration and timing of the stopping pulse. The LIF signal was measured at delays long enough (> 4000 μs) such that the decelerated OH package had already passed the trap if not trapped (see fig. 2.3.11). At such a delay, the incoupling time was scanned and optimized for maximum LIF signal. Figure 2.7.1 shows an example scan of the incoupling time, where the LIF signal was observed at a fixed time of 50 ms after trap loading and measured at a repetition rate of 0.5 Hz.

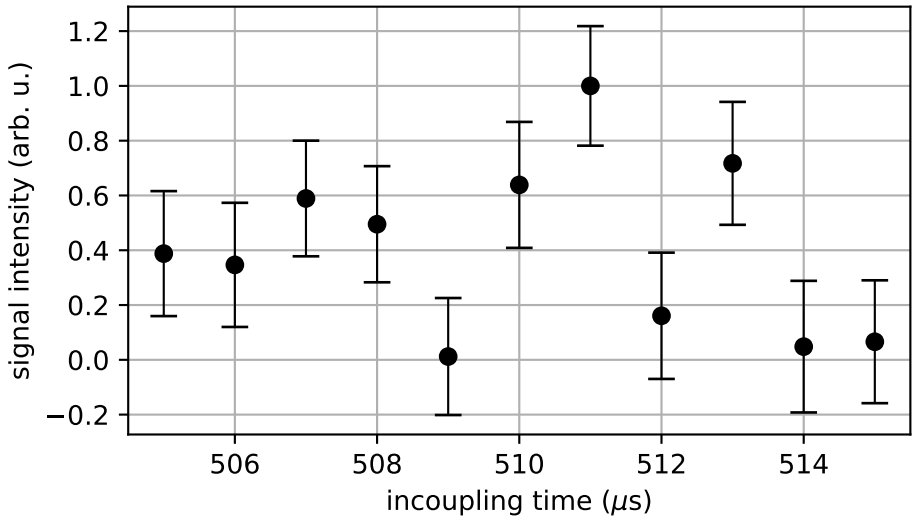

Fig. 2.7.1: **Optimization of the Incoupling Time.** The integrated LIF signal of trapped OH was measured 50 ms after trap loading at a repetition rate of 0.5 Hz. Each point represents an average of 1060 background-subtracted shots. The error bars represent one standard error of the background-subtracted signal. From this plot, we read an optimal incoupling time of 511 μs after the valve HV-discharge trigger.

The graph shows the difference between signal and background measurements (1060 shots each) per delay. The error bars are given as one standard error. After each 10 shots of signal, 10 shots of background were collected by repeating the complete sequence without triggering the discharge in the NPV. This ensures the same pressure fluctuations in the trap chamber. After subtracting the background, the final signal was normalized by the maximum of the mean values for all delays. The points at 510, 511 and 513 μs show a positive signal and are not withing error bars of e.g. the points at 514, 515 μs which correspond to the background signal level. Thus, we read an optimized incoupling time of 511-512 μs after the valve HV-discharge trigger. The low signal levels of the points at 509 and 512 μs are a result of convolutions of several effects from the molecular beam and decelerator.

The properties of the beam from the NPV varied from day to day. Thus, such a scan was necessary before each longer trapping experiment. To optimize our signal even more, the duration of the last HV-stopping pulse in the trap has to be optimized. On the one hand, if the pulse is too short, the molecules will not be stopped in the trap center. On the other hand, too long pulses will not only stop the molecules, but push them out of the trap towards the decelerator. An example stopping pulse measurement is shown in fig. 2.7.2. It shows the background-subtracted, integrated

LIF signal of 800 shots per delay, where the trap stopping pulse was switched off for background measurements. The final signal was smoothed, using a running average of 5 points. An interesting result of these measurements was the reproducible occurrence of several local maxima in the stopping pulse durations. By fitting two Gaussian peaks to this signal, we get two local maxima at 251 μs and 301 μs. Fig. 2.7.3 shows a LIF-TOF (integrated LIF traces for a certain delay after the DC discharge on the NPV) measurement of the decelerated OH package with a resolution of 5 μs. It clearly shows local maxima, separated by the same distance as the two local maxima in fig. 2.7.2. We find maxima with the same time separation in a decelerated OH package as shown in fig. 2.7.3, indicating that they can be attributed to local maxima in OH density in the decelerated OH package. However,

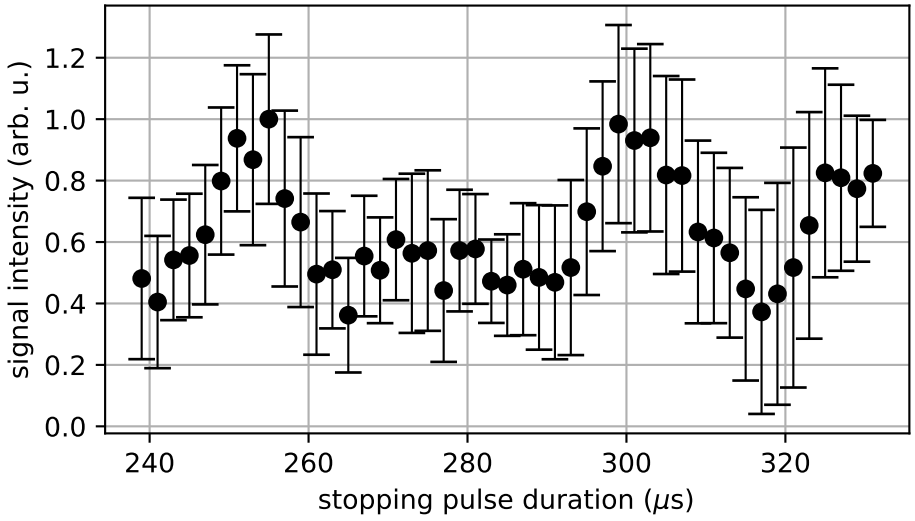

Fig. 2.7.2: **Optimization of the Stopping Pulse Duration.** The integrated LIF signal of trapped OH was measured 5 ms after trap loading at a repetition rate of 10 Hz. Each point represents an average of 800 background-subtracted shots. The error bars represent one standard error of the background-subtracted signal.

the trapping signal did not drop to zero in a range of 100 μs, making this parameter less sensitive than the incoupling time into the decelerator. As the decelerated OH cloud has a width in arrival time of about 500 μs, the signal intensity depends less on the timing and duration of the stopping pulse than the incoupling time, where the beam still has a high velocity.

Finally, we measure an integrated LIF-TOF signal of the trap-loading process by repeating the complete sequence and scan the delay of the LIF laser with respect to the DC-discharge in the NPV. Figure 2.7.4 shows in integrated LIF-TOF signal of

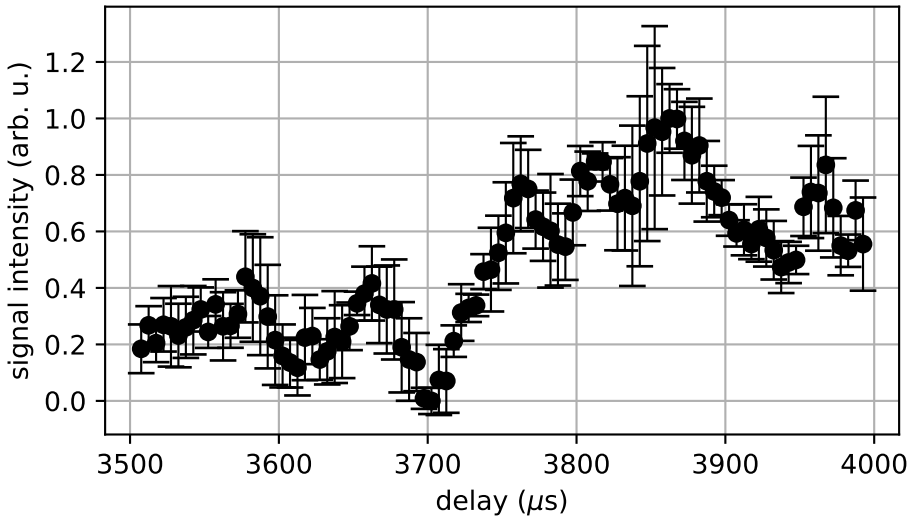

Fig. 2.7.3: **LIF-TOF measurement of the OH Package at Loading Velocity.** Several local maxima are visible with a separation of about 50 μs. Each point represents an average of 700 shots. The delay represents the time difference between the discharge pulse on the NPV and the timing of the LIF laser pulse. The error bars represent one standard error of the background-subtracted signal.

the trap-loading process. A total of 2800 shots were averaged per delay with a total measurement time of about 30 h. For better visibility, the data points are plotted as a line. The time resolution is 20 μs. The data was smoothed, using a 5-point running average. The colored area represents one standard error from the mean. The signal was measured and the corresponding offset of the LIF was subtracted to get a zero level. As we couple three phase-stable molecular packages into our decelerator, we see three packages leaving the decelerator. The first to arrive has the highest velocity, the center one is our target OH package. The peak at 3400 μs shows the fastest OH package flying through the detection volume, which is also represented by the trajectory simulation (black dotted line, developed by D. Haas)[105].
The relative height of the trapping signal to the peak at 3400 μs depends strongly on the characteristics of the NPV and the incoupling parameters. The vertical red lines show the onset and the end of the HV stopping pulse. Thus, the beginning of trapping can be defined as the time after the later red line. After the trap loading, the signal drops rapidly which is mostly related to the magnetic high-field seekers being attracted by the magnets (sec. 2.4.1.1) as well as warm molecules leaving the trap. The damped oscillatory behavior in the signal comes from the OH molecules passing the interaction volume of the focused laser in the trap center which fill out the trap volume over time. This measurement demonstrates loading of cold OH molecules in

their $X^2\Pi_{3/2}$ ($J = 3/2,\ M_J = +3/2,\ f$) ground state after Stark deceleration to 29 m/s. From trajectory simulations, we estimate translational temperatures of about 25 mK and a root-mean-square velocity of about 6 m/s after loading. The molecular densities are about half the density of the 29 m/s loading velocity signal which is estimated around 2×10^6 cm^{-3} [105]. These density estimations are including the collection efficiency from a cylindrical excitation volume with a measured $1/e^2$ radius of 0.7 mm on the PMT and the measured photon count.

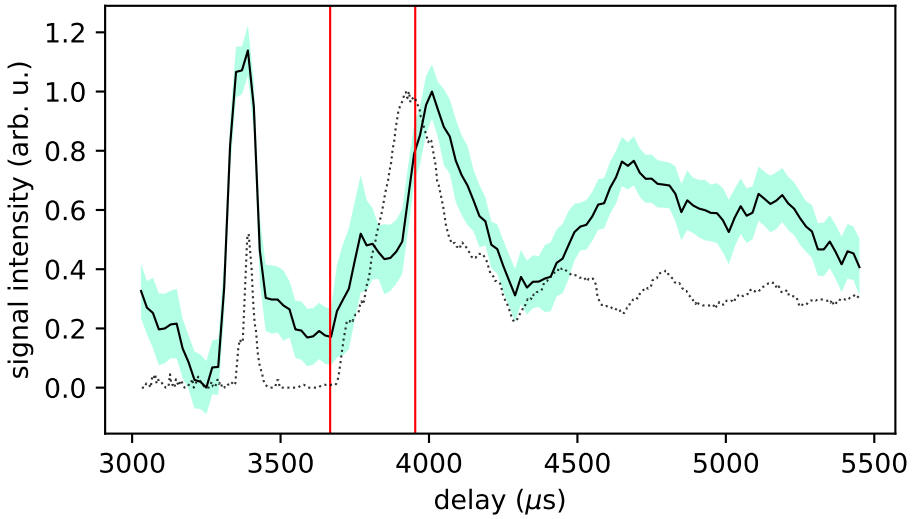

Fig. 2.7.4: **Trap Loading.** The integrated LIF signal of decelerated OH was measured for different delays after the valve discharge (solid black line). A total of 2800 shots were averaged. The coloured area represents one standard error from the mean. The vertical red lines show the onset and the end of the HV stopping pulse. For better visibility, the data points are connected by a line. The temporal resolution is 20 μs. The colored area shows the error bars as 1 standard error. The dotted black line shows a corresponding trajectory simulation.

The experiment experienced occasional transient electric discharges when the high voltages on the stopping fields or decelerator electrodes were switched, particularly under cryogenic conditions. The glow of these discharges was then picked up by the photomultiplier tube. Additionally, these discharges sometimes caused malfunctions in triggering the pulsed laser, resulting in a shut down.

In the experiment we repeated complete LIF-TOF-traces and averaged them afterwards. Thus, we were able to identify bad data points as described above. Figure 2.7.5 shows the maximum values of all 116 LIF-TOF traces which result in the plot in fig. 2.7.4.

Data points which had either a very high intensity due to discharge glows or very

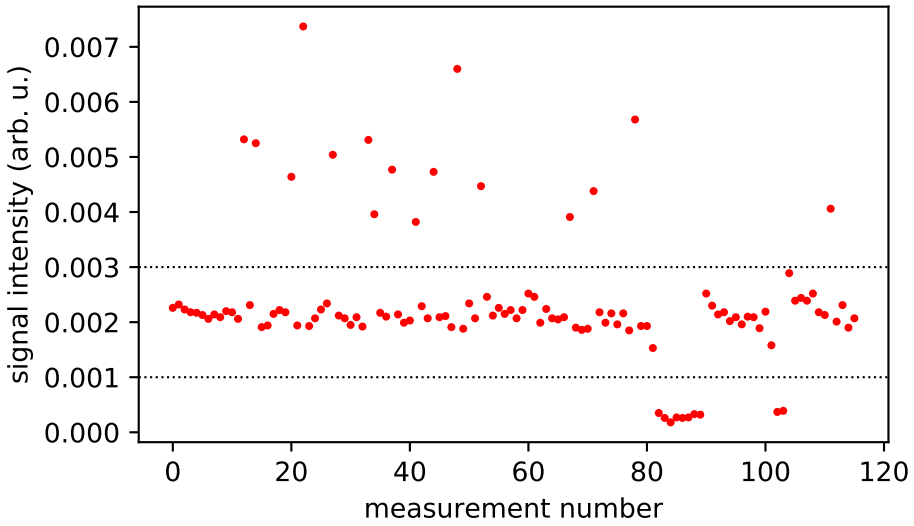

Fig. 2.7.5: **Trap Loading Data Selection.** The maximum values of several LIF-TOF traces measurements are shown. Measurements which were not between the boundaries, represented by the dotted black lines, were removed from the data set. High values are usually caused by the insulator glowing after an electric discharge. Low values are caused due to shut down of the detection laser.

low intensity due to laser shut down were removed from the presented data set. Figure 2.7.5 shows the selection criteria for the presented data in fig. 2.7.4.

2.7.2 Long-Term Cryogenic Trapping of OH

The following section is based on the publication [116]

This section presents long-term trapping (> 10 s) of cold OH molecules in a cryogenic environment and at room temperature. As discussed in sec. 2.5.2.5, the trapping-time limit due to pumping into non-trappable states by interaction with room temperature BBR is about 2.8 s for room temperature and 81 s under cryogenic conditions at a temperature of the trap environment of 17 K. The trapping measurement data is shown in fig. 2.7.6. It was recorded over several days. The population remaining in the trap was probed at increasing delays relative to the end of the trap loading sequence. The data points pertaining to a single trap-loss measurement at room temperature (295 K) were acquired as an average over 10 experimental cycles and recorded 500-1200 times depending on the specific delay. Likewise, the trap loss under cryogenic conditions (17 K) was recorded 165 times, where each acquisition comprised 5 repetition cycles of the experiment. Trapping lifetimes of the OH molecules were determined by fitting a model to the data. This model consisted of the populations from the BBR model $p_{\mathrm{BBR}}(t)$ at the measured experimental temperatures (sec. 2.5.2.5), multiplied by an exponential decay $p_{\mathrm{bg}}(t)$ to the measurements to account for collisions with background gas particles:

$$p(t) = p_{\mathrm{BBR}}(t)p_{\mathrm{bg}}(t) = p_{\mathrm{BBR}}(t)e^{-at}. \tag{2.7.1}$$

Here, a represents the background loss rate as a fitting parameter. The error bars are given as the standard error. The acquisition of the room-temperature lifetime data was performed by alternating signal and background measurements, i.e., for each delay point 10 laser pulses of signal and background were measured before the next delay point was probed. For the background measurements, the discharge unit of the pulsed valve was switched off. The red data shown in fig. 2.7.6 present a point-by-point subtraction from the recorded signal and background measurement. The acquisition of the cryogenic trap lifetime data required operation of the experiment at a repetition rate of 0.1 Hz to measure at delays of up to 10 s relative to the onset of the experimental sequence. As for the room temperature measurements, the recorded background was subtracted in a point-by-point fashion, which is depicted by the grey data points in fig. 2.7.6. In order to reduce the influence of the statistical fluctuations in the background measurements due to the comparatively low statistics, the mean value of the constant background was subtracted from the measurement, shown also in fig. 2.7.6 by the black data points. As discussed in

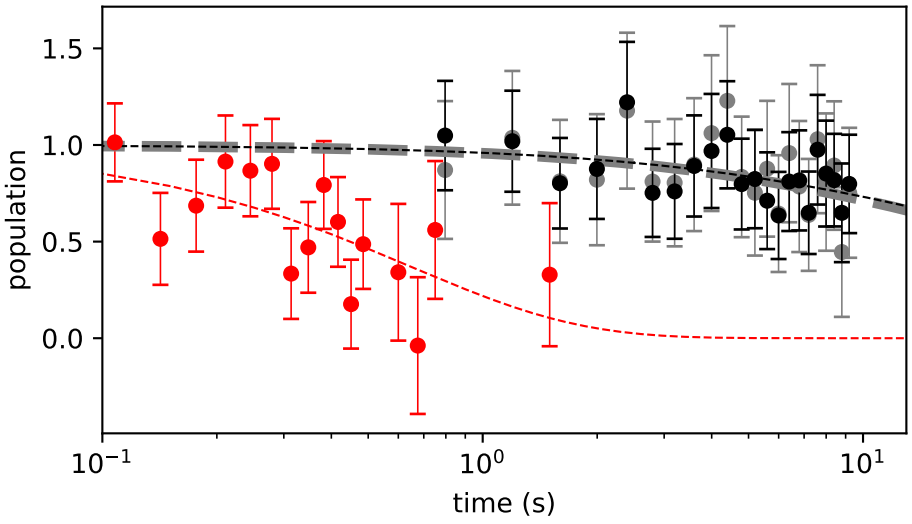

Fig. 2.7.6: **Lifetime of Trapped OH Molecules.** Fractional population of trapped OH radicals as a function of trapping-time at room temperature (295 K, red) and under cryogenic conditions (17 K, black and grey). The grey data points were obtained by subtracting experimentally determined background levels from each individual data point prior to fitting. The black data points result from the subtraction of a mean background value from the trapping signal. The dashed lines correspond to fits of the BBR model multiplied by an exponential decay to the data. The $1/e$ lifetime determined from the fits is 0.7(2) s at 295 K (red) and 45(35) s (grey) as well as 40(15) s (black) at 17 K. The time origin coincides with switching off the stopping fields. Uncertainties correspond to the standard error of 500–1200 and 121 experimental cycles for the room temperature and cryogenic data, respectively.

sec.2.5.2.5, we estimate a purely radiative lifetime of 2.8 s. The fact that the experimental result is more than a factor of 4 lower suggests that in this regime the trap lifetime is still likely to be limited by collisions with background gas particles. In order to model loss by collisions with background gas particles, we assumed that every elastic collision of an OH radical with a background gas particle leads to its ejection from the trap. For room temperature measurements, it is assumed that the main background consists of Kr from the seeding gas. At longer time scales as in the cryogenic measurements, the main background gas was assumed to be H_2 as Kr freezes out on the surfaces below 115 K. Both elastic cross sections were assumed to be identical [134]. The collision rate Z was calculated from

$$Z = \sigma_{\text{bg-OH}} v_{\text{bg}} \frac{p}{k_{\text{B}} T} \tag{2.7.2}$$

with the elastic collision cross section $\sigma_{\text{bg-OH}}$ estimated as 500 Å^2 [35] and p is the background gas pressure. The relative velocity of the background gas calculated as

$$v_{\text{bg}} = \sqrt{\frac{3k_{\text{B}}T}{m_{\text{bg}}}}\,, \tag{2.7.3}$$

where T is the assembly temperature. The model in eq. 2.7.1 was then fitted to the experimental data, to give a background collision rate, which determines the background gas pressure via eq. 2.7.2, where the background gas pressure is assumed to be constant over time.

Tab. 2.7.1: Calculated black-body radiation (BBR) pumping rates out of the trapped $|v = 0,\ J = 3/2, F = 3/2,\ M_J = 3/2,\ f\rangle$ state as well as background (BG) collision rates and radiative BBR lifetimes. Experimentally determined lifetimes are given in the last column.

assembly temperature	BG collision rate (s^{-1})	BBR pumping rate (s^{-1})	BBR lifetime (s)	exp. lifetime (s)
295 K	1.1	0.40	2.8	0.7(2)
17 K	0.008	0.030	81	40(15)

The Kr gas pressure inside the trapping region was thus estimated to be 4×10^{-8} mbar. This is a reasonable value considering that the fast part of the molecular beam is reflected off the surfaces of the cryogenic shield and the gas molecules remain in the trapping region for some time before they can escape through the apertures to be pumped away. Under cryogenic conditions (17 K), the holding duration in the trap was increased to up to 10 seconds, and a 1/e trapping lifetime of 40(15) s was determined under these conditions.[3] This value is about a factor of 2 smaller than the expected limit from BBR pumping (see Table 2.7.1). This result indicates that in this regime the lifetime is considerably enhanced comparing to room-temperature measurements. However, improving both, the shielding from room temperature BBR and the vacuum conditions to reduce the effect of collisional processes would increase the lifetime. While most gases should efficiently freeze out on the cryogenic shields surrounding the trap, these residual collisions could originate from gas particles streaming into the trapping region through the apertures in the cryogenic shield and hitting the OH molecules before they freeze out on the sur-

[3]Note that the values differ from the ones published in [116], due to the different fit model being used. In the published version, a single exponential decay was used to extract the lifetime by fitting to the data.

faces. Another likely contribution are collisions with hydrogen molecules which are not expected to freeze out efficiently on the surfaces under the UHV conditions and cryogenic temperatures of the present experiment. Assuming that the trap lifetime is limited by the collision rate with H_2 molecules at 17 K, an effective H_2 pressure of 1×10^{-11} mbar in the trapping region can be deduced from this lifetime. This value is on the same order as the typical pressures measured by a pressure gauge in the trap chamber surrounding the cryogenic shield.

Using the rate of collisions with background gas particles Z as defined in eq. (2.7.2) and the pumping rates out of the ground state from the BBR model, we can compare the rates for different background pressures as shown in fig. 2.7.7. The BBR pumping rates from the ground state are shown as dashed lines: blue at 295 K, black under cryogenic conditions using the effective spectral energy density of BBR and red shows the case at 17 K purely. The black line shows the rate of collisions with background gas particles at 295 K and the blue line at 17 K. From this figure, we see that in the cryogenic experiments, the BBR loss rate and the background collision rate are equal around 2×10^{-10} mbar H_2 pressure and in the room temperature case at a Kr partial pressure of 1×10^{-8} mbar.

In the room temperature experiments, the trap loss rate due to collisions with background gas particles was slightly higher than the loss rate due to BBR pumping. Lower background gas pressures could potentially increase the trapping-times up to an upper limit of 2.8 s. In the cryogenic experiments the trend was inverted. Improved shielding from room-temperature BBR can increase the BBR-limited lifetimes by another factor of 5 as shown in fig. 2.5.7 and improving the vacuum conditions would increase the lifetime as well.

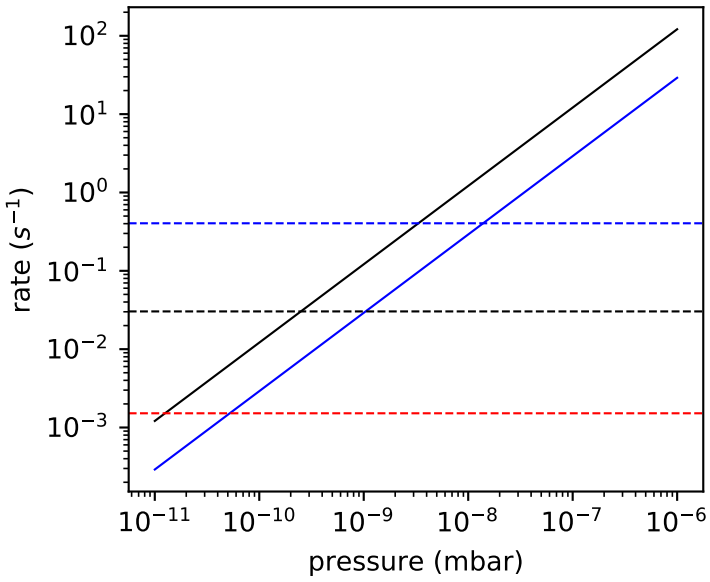

Fig. 2.7.7: **Comparison of Collision Rates with Background Gas and BBR Pumping Rates.** The BBR pumping rates from the ground state are shown as dashed lines: blue at 295 K, black under cryogenic conditions using the effective BBR intensities and red shows the case at 17 K. The solid blue line shows the collision rate with background gas at 295 K and the black line at 17 K.

2.8 Conclusion and Outlook

This chapter discussed the complete development of a cryogenic magnetic trap for translationally cold radicals. Cold OH radicals were produced via the NPV valve with subsequent Stark deceleration to longitudinal velocities of 29 m/s. The stopping pulses and the basic geometry were optimized by D. Haas to reach a loading efficiency of 25% of the decelerated molecules into the trap with densities on the order of 10^6 cm^{-3}, where half will still be lost due to the magnetic low field seekers, being attracted by the magnets. We finally reached a loading efficiency of approx. 10%, estimated by comparison to trajectory simulations.

A cryogenic setup was built, which allowed the application of stopping pulses with amplitudes of $\pm$5.8 kV at temperatures of 17 K in the trap environment. The cryogenic shields have proven their value by allowing us to trap OH molecules on the order of tens of seconds (40(15) s) and improving the lifetime compared to the room temperature case (0.7(2) s) by a factor of about 57. This is a result of reduced background pressures in the cryogenic environment as well as shielding from room temperature BBR.

A model to estimate the lifetime of trapped OH radicals, limited by BBR-induced pumping into untrappable states was developed and applied to measurements. The model was based on a rate equation model and considered magnetic high-field seekers as lost. An effective spectral energy density of BBR was modeled by summing the contributions at temperatures of our three stages (295, 53 and 17 K), weighted by their solid angle contributions illuminating the trap volume. The BBR-limited lifetime was estimated to be 2.8 s at room temperature and 80 s in the cryogenic environment. We estimated a background pressure of Kr at room temperature of 4×10^{-8} mbar and in the cryogenic case 1×10^{-11} mbar of H_2. Both, improved vacuum conditions and better shielding from BBR could potentially increase the lifetimes.

Besides collisions with the background gas and pumping by BBR, loss of OH radicals from the trap can also result from Majorana-type transitions close to the field-free trap center and from non-adiabatic spin-flip transitions in crossed electric and magnetic fields [30, 135, 136, 137, 138]. In our experiments, an electric field is applied to the stopping electrodes near the trap for a short duration of around 250 µs. As can be seen from comparing the signal levels in fig. 2.7.4, the loss of OH radicals observed during this period is on the order of 50%. This is expected as magnetically low-field seeking molecules are lost in the magnetic trap. Therefore, we conclude

that loss by spin-flip transitions only plays a minor role during the loading phase of the experiment. Majorana-type losses can in principle occur during the hold time of the molecule in the trap. However, the trap loss observed seems to be dominated by collisions with residual background gas and loss due to BBR pumping. Losses due to inelastic collisions between OH radicals do not appear to play a dominant role at the trap densities prevailing in the present experiments.

The presented project successfully demonstrated the design and development of a cryogenic trap and experimental results of long-term trapping of OH radicals in this trap. Optimizations to the given trap design are already being developed by C. Mangeng which are based on the outcome of this project. We tackle high-voltage problems with replacing the HV stopping part by pulsed electromagnets, similar to the trap in reference [139]. Furthermore the low signal levels in the detection (about 1 signal photon against 10 background photons) will be improved by adding additional observables. Therefore, we plan to implement a second detection method. OH radicals will be ionized via REMPI and detected with a TOF mass spectrometer [140] on a microchannel plate detector (MCP). The mass spectrometer can then not only be used to detect OH but also to detect future reaction products from cold collisions in a hybrid trap. The next step to hybrid trapping is the ion trap. The development of a cryogenic ion trap is discussed in the next chapter.

Chapter 3

Ion Trap

After trapping neutral OH radicals on the order of tens of seconds in a magnetic trap, the next step towards building a hybrid trap for neutral molecules and molecular ions was the development of the ion trap. A small glimpse at the ion trap was already given in section 2.5.3. The geometrical choices in the magnetic trap directly influenced the geometrical restrictions of the ion trap.
In this chapter we discuss the principles behind ion traps, our choice of ion trap and its design. We therefore start with a general introduction about ion traps followed by the source and production of the ions. Furthermore, this trap has to function with high voltage being pulsed in proximity used for stopping of the neutral molecules. We thus developed a shielding for the trap which will be characterized numerically. This ion trap is the second part in the design of the hybrid trap, allowing the trapping of Ca^+ ions and sympathetically cooled molecular ions such as N_2^+, moving one step closer towards studying cold collisions between cold neutral molecules and cold molecular ions.

3.1 Ion Traps: An Overview

Compared to neutral molecules or atoms, cold ions offer much more control as they offer a strong particle-particle interaction from the Coulomb repulsion and are easily manipulable with electric fields, where even single ions can be used for experiments [141, 142].

Nowadays, trapped ions belong to the best controlled quantum systems and are used in precision spectroscopy [1, 2] and quantum information processing [4, 5, 6, 90, 142]. The high degree of precision these systems allows to test fundamental physical theories such as the time variation of physical constants [143, 144] and the existence of the dipole moment of the electron [145].

The particular interest for this work lies in the ordered structures of ions in ion traps referred to as Coulomb crystals [146]. The long-term goal is investigating collisions between cold neutral molecules and cold molecular ions. These structures can be stored in ion traps for hours [141] and have found applications in studies of ultracold chemistry [26, 40, 55, 147].

Atomic ions with simple energy level structures, such as alkaline earth metal ions, can be cooled down using laser cooling [148]. Due to the strong particle-particle interaction between ions, these can be used to sympathetically cool molecular ions [40, 55, 149, 150]. A commonly used form of the ion trap is the Paul trap [151] which is also implemented in this study, which combines radiofrequency (RF) electric fields with constant direct current (DC) electric fields in order to achieve confinement of the ions.

3.2 The Paul Trap

For trapping ions, we take advantage of the electrostatic force $\mathbf{F}_{\text{ion}}$ acting on the ion in an electric field which is given by

$$\mathbf{F}_{\text{ion}} = q\mathbf{E} \ , \tag{3.2.1}$$

where q is the charge of the ion and the electric field $\mathbf{E} = -\Delta\phi$, where ϕ is the electric potential. The typical choice for ion traps is an electric field which depends linearly on the spatial coordinates [151]. Such a field is produced by the electrostatic potential

$$\phi\left(x, y, z\right) = V_0 \left(ax^2 + by^2 + cz^2\right) \ , \tag{3.2.2}$$

where V_0 is the amplitude with the parameters a, b and c. From Maxwell's first equation for a source-free region, one arrives at a condition for the potential of the form of Laplace's equation [152]

$$\Delta\phi = 0 \ . \tag{3.2.3}$$

Therefore, the coefficients in eq. 3.2.2 have to fulfill the condition

$$a + b + c = 0 \ . \tag{3.2.4}$$

One solution to this equation is $a = -b = \frac{1}{r_0^2}, c = 0$, i. e., a quadrupolar potential, corresponding to a linear mass filter consisting of four hyperbolic electrodes. Fig. 3.2.1 shows hyperbolic electrodes in grey and the electrodes which are used in this work as black circles for comparison. While a voltage of V_0 is applied to one pair of opposite electrodes, a voltage of $-V_0$ is applied to the other pair. The coordinate system x, y was used in this derivation and as a comparison our experimental coordinate system as used for the magnetic trap is shown as X, Y. The radial distance from the trap center to the surface of an electrode is denoted as r_0. The quadrupolar electric potential focuses the ions along the x-axis and defocuses along y. However, if one rotates this potential around the z-axis over time with a frequency of Ω, one achieves a two-dimensional confinement in the xy-plane (radial confinement). The z-axis is perpendicular to the xy plane and is also referred to as

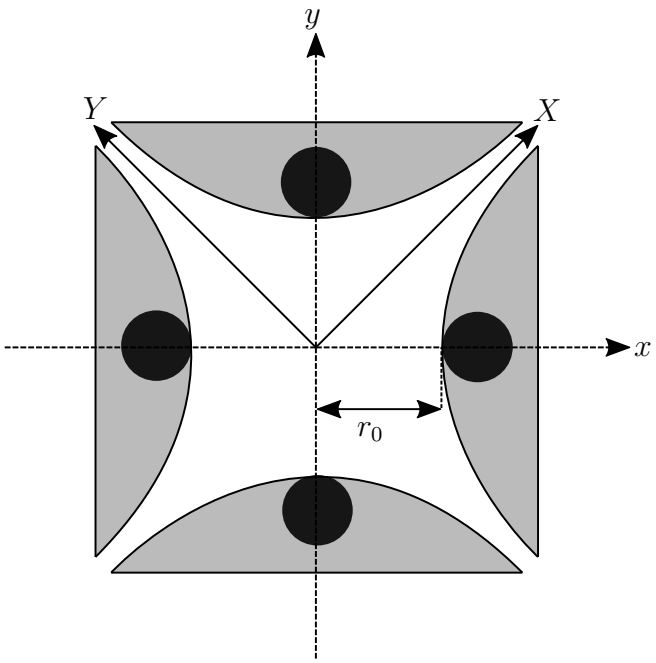

Fig. 3.2.1: **Hyperbolic Electrodes.** The hyperbolic electrodes which were assumed in this derivation are shown in grey. As a comparison, the electrodes which are used in this thesis are shown as black circles. The coordinate system x, y was used in this derivation and as a comparison our experimental coordinate system as used for the magnetic trap is shown as X, Y. The radial distance from the trap center to the surface of an electrode is denoted as r_0.

the trap axis. Therefore, a time-dependent radio frequency (RF) voltage V_{RF} of

$$V_{\mathrm{RF}} = V_0 \cos(\Omega t) \tag{3.2.5}$$

is applied to a pair of opposite electrodes and $-V_{\mathrm{RF}}$ to the other pair. These electrodes, however, only provide confinement in the xy plane, or radial confinement and the resulting potential in proximity of the trap center is given by

$$\phi_{\mathrm{RF}} = V_0 \left(\frac{x^2 - y^2}{r_0^2} \right) \cos(\Omega t) \ , \tag{3.2.6}$$

where r_0 is half of the distance between two opposite electrodes.
To achieve confinement along the z-axis, axial confinement, by adding endcaps with a static positive voltage U_{end} applied. A trap of this type is referred to as a linear Paul trap which consists of four rods parallel to the z-axis at the corner of a square in the xy-plane [153]. The static potential close to the trap center can be approximated

as

$$\phi_{\text{end}} = \frac{\kappa U_{\text{end}}}{z_0^2}\left(z^2 - \frac{1}{2}\left(x^2 + y^2\right)\right) \ , \tag{3.2.7}$$

where z_0 is half of the distance between the two endcap electrodes and κ is a geometrical parameter (see sec. 3.5.2.1).
Adding the static and the time-dependent potentials and substituting with $\tau = \frac{\Omega t}{2}$ leads to the equations of motion according to eq. 3.2.1:

$$\frac{\mathrm{d}^2 x}{\mathrm{d}\tau^2} + x\left(\frac{-4q\kappa U_{\text{end}}}{m\Omega^2 z_0^2} + \frac{8qV_0}{m\Omega^2 r_0^2}\cos(2\tau)\right) = 0 \ , \tag{3.2.8}$$

$$\frac{\mathrm{d}^2 y}{\mathrm{d}\tau^2} + y\left(\frac{-4q\kappa U_{\text{end}}}{m\Omega^2 z_0^2} - \frac{8qV_0}{m\Omega^2 r_0^2}\cos(2\tau)\right) = 0 \ , \tag{3.2.9}$$

$$\frac{\mathrm{d}^2 z}{\mathrm{d}\tau^2} + \frac{8q\kappa U_{\text{end}}}{m\Omega^2 z_0^2} = 0 \ , \tag{3.2.10}$$

where m is the mass of the ion. These have the form of the Mathieu equations [154]

$$\frac{\mathrm{d}^2 u}{\mathrm{d}\tau^2} + \left[a_u + 2q_u\cos\left(2\tau\right)\right]u = 0, u \in \{x, y, z\} \ , \tag{3.2.11}$$

with the Mathieu stability parameters [142]

$$a_x = a_y = -\frac{1}{2}a_z = \frac{-4\kappa q U_{\text{end}}}{m\Omega^2 z_0^2} \ , \tag{3.2.12}$$

$$q_x = q_y = \frac{4qV_0}{m\Omega^2 r_0^2} \ , \ qz = 0 \ . \tag{3.2.13}$$

Fig. 3.2.2 shows the stable regions leading to stable trajectories and confinement of the ion in the trap depending on a_u and q_u, where the functions *mathieu a(m,q)* and *mathieu b(m,q)* from the python package *scipy.special* were used [155]. Summarized, the motion of the ion is periodic and can be separated into two components, called the adiabatic approximation.

3.2.1 The adiabatic approximation

The ion motion in an inhomogeneous RF-field can be described by assuming the field to vary smoothly for the spatial coordinate $\mathbf{r}$ and the frequency is high enough such that the amplitude of the oscillatory motion is small, called the adiabatic approximation.
It is convenient to describe the ion motion as the sum of two separated motions:

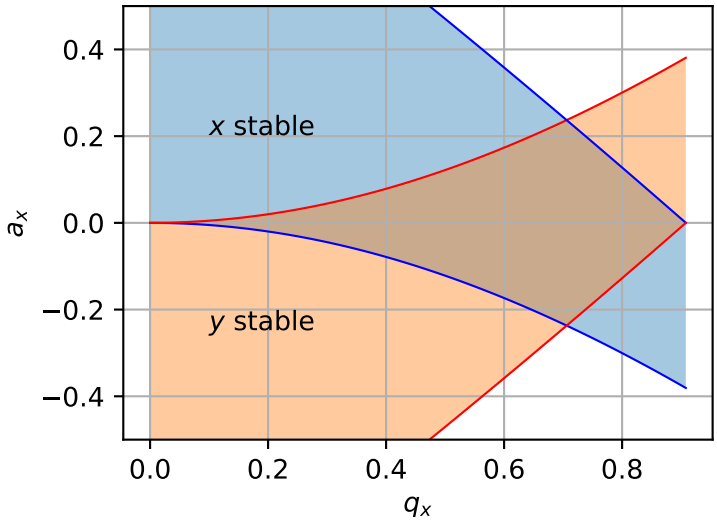

Fig. 3.2.2: **Stability Diagram for the Linear Paul trap.** Characteristic values for the even and odd Mathieu function which enclose a stable region for the x and y direction.

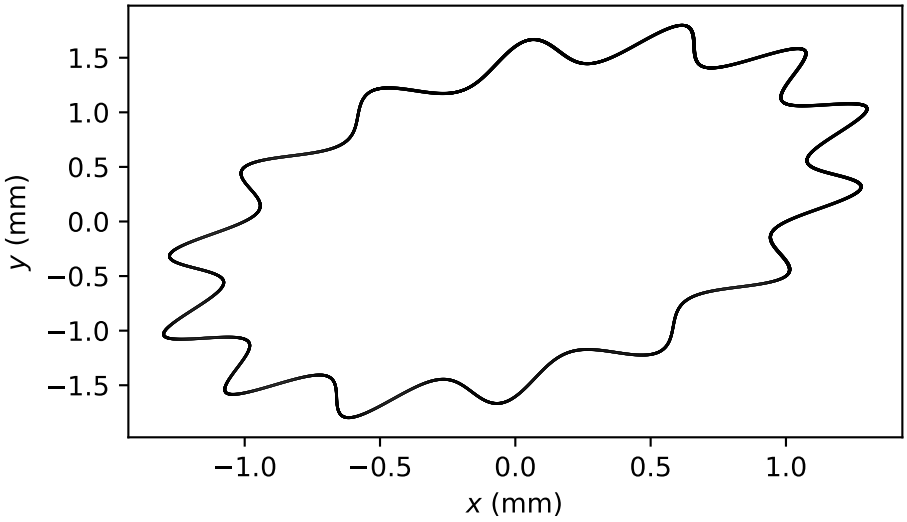

Fig. 3.2.3: **Ion motion.** The trajectory of an ion in a Paul Trap was simulated by solving the Mathieu equation for $a_x = 1 \times 10^{-4}$ and $q_x = 0.2$. The ion shows a slow smooth drift overlapped with a fast oscillating motion.

a slow drift motion and a fast oscillating motion as shown in fig. 3.2.3, where the Mathieu equations (3.2.11) were solved for $a_x = 1 \times 10^{-4}$ and $q_x = 0.2$. The ion shows a slow smooth drift overlapped with a fast oscillating motion. For $|a_u|^2$ and $q_u^2 \ll 1$ the trajectory of the ion can be approximated as [142, 156]

$$u(t) \approx u_0 \cos(\omega_u t + \phi) \left(1 + \frac{1}{2} q_u \cos(\Omega t)\right) \ , \tag{3.2.14}$$

where ϕ is a phase, depending on the initial position and velocity of the ion and $u_0 \equiv x_0, y_0, z_0$ are the initial amplitudes. The slow motion of the ions, the secular motion, can be described by the first term with the secular frequencies

$$\omega_u = \frac{1}{2}\Omega\sqrt{a_u + \frac{1}{2}q_u^2}\ . \tag{3.2.15}$$

The second term describes the fast oscillating motion, the micromotion[157, 158]. Generally, when assuming an electric field $\mathbf{E}(\mathbf{r}, t)$ to be composed of a static electric field $\mathbf{E}_{\mathrm{DC}}(\mathbf{r})$ and a time dependent part $\mathbf{E}_{\mathrm{RF}}(\mathbf{r})\cos\Omega t + \delta$, the equation of motion for an ion can be written as

$$m\ddot{\mathbf{r}} = q\left(\mathbf{E}_{\mathrm{RF}}(\mathbf{r})\cos\Omega t + \mathbf{E}_{\mathrm{DC}}(\mathbf{r})\right) \tag{3.2.16}$$

Now, we want to find a solution by adding a slow drift $\mathbf{R}_0(t)$ and a fast oscillating motion $\mathbf{R}_1(t)$ such that

$$\mathbf{r}(t) = \mathbf{R}_0(t) + \mathbf{R}_1(t) \tag{3.2.17}$$

with

$$\mathbf{R}_1(t) = -\mathbf{a}(t)\cos\Omega t\ . \tag{3.2.18}$$

Assuming a slow time derivation of the amplitude $\mathbf{a}$ and the smooth term R_0 implies $\dot{\mathbf{a}} \ll \Omega\mathbf{a}$ and $\ddot{\mathbf{R}}_0 \ll \Omega\dot{\mathbf{R}}_0$. Additionally replacing $\cos^2\Omega t$ by the time averaged value $1/2$ results in the equation of motion for the secular motion

$$m\ddot{\mathbf{R}}_0 = \frac{-q^2}{4m\Omega^2}\nabla\mathbf{E}_{\mathrm{RF}}^2. \tag{3.2.19}$$

This time-averaged expression shows us a force acting on the charged particle depending on the gradient of the field, pushing the ion towards the trap center, the region of a minimal field. As the charge q is squared, the force is independent on the sign of the charge. As a result, when viewing the right-hand side of eq. (3.2.19) as the negative gradient of the time-independent potential, we can describe the motion by a time-averaged pseudo-potential [159]

$$V_{\mathrm{ps}}(\mathbf{r}) = \frac{q^2}{4m\Omega^2}\mathbf{E}_{\mathrm{RF}}^2(\mathbf{r}) \tag{3.2.20}$$

and finally by an effective potential

$$V_{\text{eff}}(\mathbf{r}) = \frac{q^2}{4m\Omega^2}\mathbf{E}^2_{\text{RF}}(\mathbf{r}) + qU_{\text{DC}}. \tag{3.2.21}$$

The motion of the ion is completely described by the Mathieu equations (eq. 3.2.11). However, this effective potential approximation can be used to gain insight into the ion trajectory for $q_u \leq 0.4$ [157].

3.3 Calcium Source

The ion trap is designed to trap laser-cooled $^{40}Ca^{+}$ ions. This section covers the discussion of the calcium source in our trap. Our calcium source consists of a resistively heated Ca oven (AlfaVakuo, AS-Ca-2.5-080-3S - AlfaSource Ca-2.5). The oven contains Ca powder with a purity of 99.5 % which is evaporated at around 555 K, at a current of around 7 A with a frequency of 50 Hz in our setup. The opening is sealed by a thin layer of indium, which is usually removed around 450 K [160]. The current to heat the oven is supplied by a home-built AC current supply, which can be remotely switched on/off via a transistor–transistor logic (TTL) pulse. Fig. 3.3.1 shows the assembly of the Ca source. (1) is the said Ca oven which is connected to two copper parts (2) where the electrical currents for heating are applied. To isolate this part electrically and thermally from the rest, the copper parts (2) are held by two parts made of Macor®(3). Both ends (3) are stabilized with a aluminium part (4). To reduce the amount of Ca sprayed onto the trap electrodes, the Ca beam is skimmed with a small slit with a height of 500 μm and a width of 2 mm (5). Part (4) is connected to a spacer (6). The whole assembly is mounted on the first stage of the cryogenic assembly (see sec. 2.5.1) using two Macor®parts. The choice of material for the latter is due to its low thermal conductivity to reduce the heat flow between the Ca oven and the cryogenic assembly. As the copper parts are connected to thick copper wires with a diameter of 5 mm, the heat flow between the chamber walls and the Ca tube will be much larger than the heat flow between the Ca oven and the cryogenic assembly.
On the ion trap side, another skimmer plate made of copper is used (8). Fig. 3.3.1 a) shows the Ca oven, b) shows the oven mounted on the cryogenic assembly, where the cryogenic shields are not shown. The magnetic trap assembly consisting of stopping wires and magnets is shown on the left (10). Fig. 3.3.1 c) shows a front view of the skimmer plate (8) on the ion trap. The holders of the ion trap wires and the endcaps (not shown) is visible in fig. 3.3.1 d) (9). The green line (11) in fig. 3.3.1 d) connects the opening of the Ca oven tube to the ion trap center.

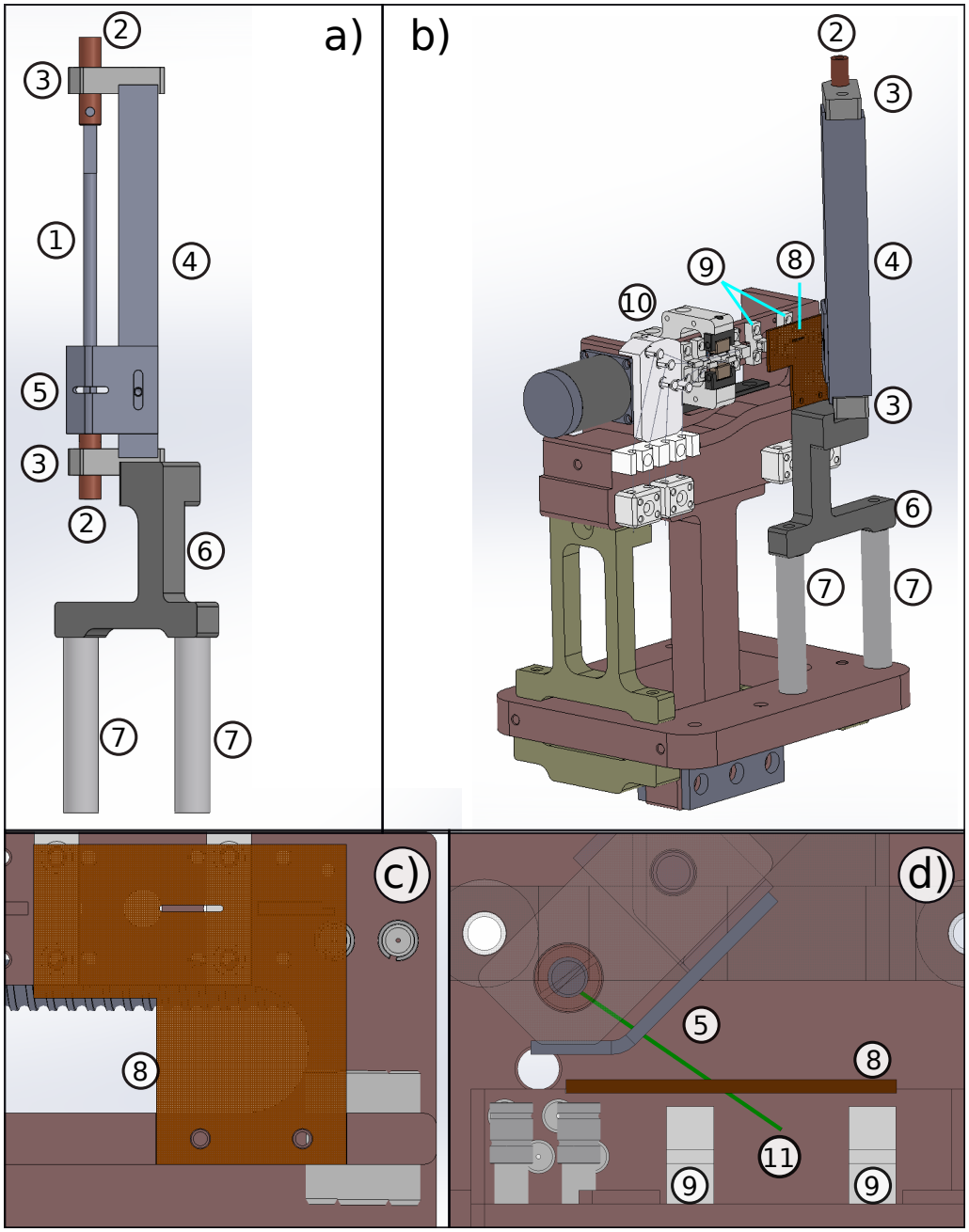

Fig. 3.3.1: **Ca Source.** The Ca oven (1) is connected to two copper parts (2) where the electrical current for resistive heating is applied. For thermal and electrical insulation, the copper parts (2) are held by two parts made of Macor®(3). These (3) are stabilized with an aluminium holder (4). The Ca beam is streaming out of the opening to the trap center along the line (11) and the beam is skimmed with a slit with a height of 500 μm and a width of 2 mm (5). Part (4) is connected to a spacer (6). The whole assembly is mounted on the first stage of the cryogenic assembly using two Macor®parts (7). On the ion trap side, another skimmer plate made of copper is used (8). Part a) shows the Ca oven, b) shows the oven mounted on the cryogenic assembly. The magnetic trap assembly is shown (10). Part c) shows a front view of the skimmer plate (8) on the ion trap. The holder of the ion trap wires and the endcaps (not shown) is visible in d) (9). The green line (11) in d) connects the opening of the Ca oven tube to the ion trap center.

3.3.1 Ionization of Ca atoms

Photo-ionization of a calcium beam has first been shown by Kjærgaard et al. Photo-ionization as opposed to electron bombardment allows selective loading of isotopes as well as loading a specific number of ions into a trap [161]. To generate ions from the neutral Ca beam provided by the calcium oven, we use a resonance-enhanced photoionization scheme (REMPI) [36, 37]. This method has the advantage of a large cross section for field ionization when exciting high-lying Rydberg states [36, 37] and requires the use of cheap diode-laser systems. In a first step, the atom is excited from the $4s^1S_0$ ground state to the $4p^1P_1$ excited state using a laser with a wavelength of around 423 nm. The decay into the metastable $3d^1D_2$ state is negligible due to the small branching ratio. In the original scheme from Gulde et al. [36], the atoms are excited to a Rydberg state with principal quantum number around 30 in a laser field of 390 nm and are subsequently ionized in the presence of strong electric fields. Isotope shifts are significantly larger than the excitation linewidth, which is why this scheme allows isotope selective ionization of Ca [36]. Lucas et al. found that the 390 nm laser may be replaced by an incoherent light source with a central wavelength of 375 nm [37] leading to a direct ionization from the $4p^1P_1$ state. Thus, we use a commercially available free-running laser diode with a wavelength of 375 nm (Thorlabs, L375P70MLD) combined with the laser with a wavelength of 423 nm. Fig. 3.3.2 shows the relevant electronic energy levels of atomic calcium for the ionization.

Figure 3.3.3 shows an image of Ca atoms in the trap volume, where the fluorescence of calcium from the excited state $4p^1P_1$ to the ground state $4s^1S_0$ with a wavelength of 423 nm was collected on a charge-couple-device (CCD) chip coupled to a microscope. When overheating the oven, the trap was covered in calcium and the oven deformed. Therefore the oven had to be operated at minimal conditions (heating current of 6 A at a frequency of 50 Hz) to find calcium, which resulted in a very weak fluorescence signal. The image shows the signal of the fluorescence minus the background which consisted of oven glowing, background light from the excitation laser at 423 nm as well as a constant stray-light background. The data was collected with a power of the excitation laser of 2 mW, an exposure time of 0.3 seconds with electron multiplying gain and a magnification of 4. For more details about the imaging setup, see sec. 3.4.6.

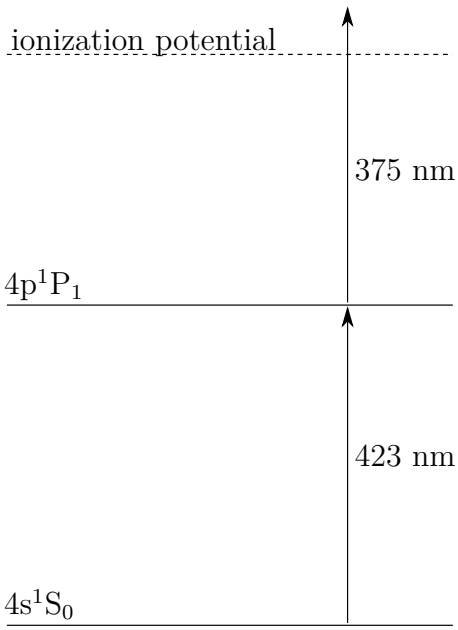

Fig. 3.3.2: **Resonance-Enhanced Photoionization Scheme.** The relevant levels for the REMPI of Ca atoms are shown. The laser at 423 nm drives the dipole transition from the $4s^1S_0$ ground state to the $4p^1P_1$ excited state. The second step is the ionization with a laser at a wavelength of 375 nm.

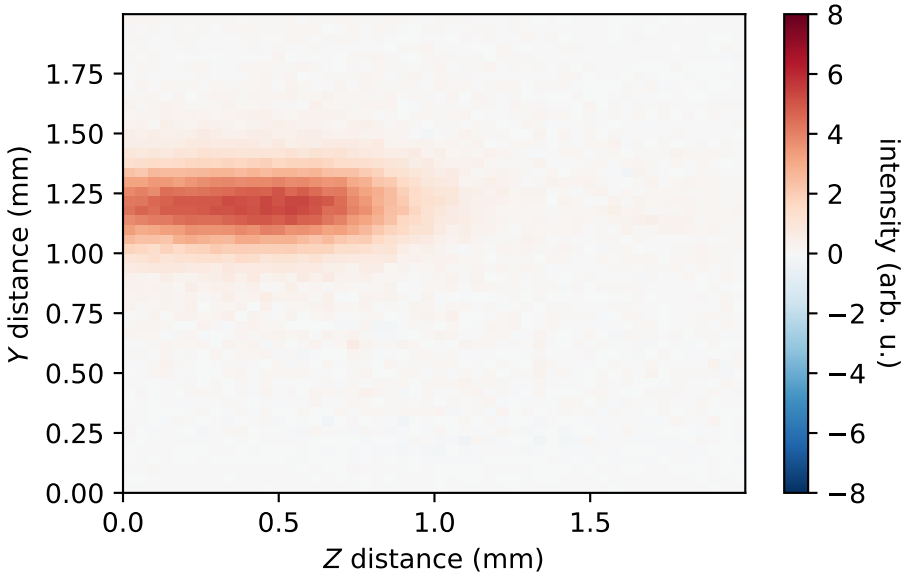

Fig. 3.3.3: **Ca Atoms.** The fluorescence of calcium from the excited state $4p^1P_1$ to the ground state $4s^1S_0$ with a wavelength of 423 nm is collected from the trap volume.

3.4 Doppler Cooling of Calcium Ions

To generate translationally cold ions, we cool down warm Ca^+ ions by means of laser cooling [142, 162]. Cooling trapped ions was pioneered by Wineland et al. [163] and Neuhauser et al. [148]. The principle of laser cooling lies in the momentum transfer by absorption of photons from a laser beam. By detuning the laser frequency to the red side of a resonance, the absorption rate of atoms moving in the opposite direction of the laserbeam is higher due to the detuning being compensated by the Doppler shift. As laser cooling requires simple energy-level structures which allow for closed optical cycles, the method is limited to a few species such as the alkaline-earth ions Be^+, Mg^+, Ca^+, Ba^+ and Sr^+. Molecules which allow for an optical closed cycle can be laser cooled as well, e.g. laser cooling of SrF molecules was achieved by McCarron et al. [22] and CaF molecules by Anderegg et al. [23]. The force acting on a particle during laser cooling is described by the scattering force. The next sections are used to derive the scattering force, starting with the description of atom-light interaction.

3.4.1 The Rabi Two-Level Problem

Let H_{atom} be the atomic Hamiltonian with the eigenstates $|n\rangle$ and H_{i} is the interaction Hamiltonian, describing the interaction of the atom's induced dipole moment with the electric field of light. The total Hamiltonian is then given by [162]

$$H = H_{\text{atom}} + H_{\text{i}} \ , \tag{3.4.1}$$

with

$$H_{\text{i}} = -\mu \cdot \mathbf{E} = e \ \mathbf{r} \cdot \mathbf{E_0} \ \cos(\omega t) \ , \tag{3.4.2}$$

where e is the electric charge at position $\mathbf{r}$, $\mathbf{E_0}$ is the electric field amplitude vector of the electromagnetic wave and ω is its angular frequency. Assuming a two level system with the states $|1\rangle$ and $|2\rangle$ we propagate the time independent $|n\rangle$ by

$$|n(t)\rangle = e^{-iH_{\text{atom}}t/\hbar}\,|n\rangle = e^{-iE_{\text{atom}}t/\hbar}\,|n\rangle = e^{-i\omega_n t}\,|n\rangle \, . \tag{3.4.3}$$

We can write the total wave function as a superposition both states

$$\Psi(\mathbf{r}, t) = \sum_{n=1}^{2} c_n(t) \ |n(t)\rangle \ , \tag{3.4.4}$$

where the coefficients c_n have to satisfy the normalization condition

$$\sum_{1}^{2} c_n(t)^2 = 1 \ . \tag{3.4.5}$$

Finally, the time dependent Schrödinger equation is solved, using eq. (3.4.4) as an ansatz which leads to the coupled differential equations for the coefficients c_n:

$$i\dot{c_1} = \Omega \cos(\omega t) e^{-i\omega_{21}t} c_2 \ , \tag{3.4.6a}$$

$$i\dot{c_2} = \Omega \cos(\omega t) e^{i\omega_{21}t} c_1 \ , \tag{3.4.6b}$$

where $\omega_{21} = \omega_2 - \omega_1$. Ω is the Rabi frequency, which is defined as

$$\Omega = \frac{e \ \langle 1|\mathbf{r} \cdot \mathbf{E_0}|2\rangle}{\hbar} \ . \tag{3.4.7}$$

The Rabi frequency describes the coupling strength between the two states by the interaction of the induced atomic dipole moment with the external electric field. Using the rotating wave approximation leads to eqns. (3.4.6a) and (3.4.6b) as [162]

$$i\dot{c_1} = \frac{\Omega}{2} e^{i(\omega-\omega_{21})t} c_2 \ , \tag{3.4.8a}$$

$$i\dot{c_2} = \frac{\Omega^*}{2} e^{-i(\omega-\omega_{21})t} c_1 \ . \tag{3.4.8b}$$

So far, the effect of spontaneous emission has been neglected completely, which means that the model has to be further generalized. This will eventually lead to the optical Bloch equations, for which the density matrix formalism has to be introduced.

3.4.2 The Optical Bloch Equations

To further analyze the Rabi two-level problem, we write the density matrix for a pure state as [162]

$$\rho = \begin{pmatrix} \rho_{22} & \rho_{21} \\ \rho_{12} & \rho_{11} \end{pmatrix} = \begin{pmatrix} c_2 c_2^* & c_2 c_1^* \\ c_1 c_2^* & c_1 c_1^* \end{pmatrix} \ . \tag{3.4.9}$$

The spontaneous emission is included as

$$(\dot{\rho}_{ij})_{\text{spont}} = -\frac{\Gamma}{2} \rho_{ij} \ , \tag{3.4.10}$$

which describes an exponential decay with a rate $\Gamma/2$. With eqns. (3.4.8a), (3.4.8b), the detuning $\delta = \omega - \omega_{21}$ and $\tilde{\rho}_{12} := \rho_{12} e^{-i\delta t}$, we obtain the optical Bloch equations (OBEs):

$$\dot{\rho}_{11} = +\Gamma\rho_{22} + \frac{i}{2}\left(\Omega^*\tilde{\rho}_{21} - \Omega\tilde{\rho}_{12}\right) \ , \tag{3.4.11a}$$

$$\dot{\rho}_{22} = -\Gamma\rho_{22} + \frac{i}{2}\left(\Omega\tilde{\rho}_{12} - \Omega^*\tilde{\rho}_{21}\right) \ , \tag{3.4.11b}$$

$$\dot{\tilde{\rho}}_{12} = -\left(\frac{\Gamma}{2} + i\delta\right)\tilde{\rho}_{12} + \frac{i}{2}\Omega^*\left(\rho_{22} - \rho_{11}\right) \ , \tag{3.4.11c}$$

$$\dot{\tilde{\rho}}_{21} = -\left(\frac{\Gamma}{2} - i\delta\right)\tilde{\rho}_{21} + \frac{i}{2}\Omega\left(\rho_{11} - \rho_{22}\right) \ . \tag{3.4.11d}$$

Combining $\rho_{11} - \rho_{22} =: w$ results in

$$\dot{\rho}_{21} = -\left(\frac{\Gamma}{2} - i\delta\right)\rho_{21} + \frac{iw\Omega}{2} \ , \tag{3.4.12a}$$

$$\dot{w} = -\Gamma w - i(\Omega\rho_{21}^* - \Omega^*\rho_{21}) + \Gamma \ . \tag{3.4.12b}$$

with the steady state solutions($\dot{w} = \dot{\rho}_{21} = 0$):

$$\rho_{21} = \frac{i\Omega}{2(\Gamma/2 - i\delta)(1+s)} \ , \tag{3.4.13a}$$

$$w = \frac{1}{1+s} \ . \tag{3.4.13b}$$

The saturation parameter s is defined as

$$s = \frac{|\Omega|^2}{2|(\Gamma/2 - i\delta)|^2} = \frac{|\Omega|^2/2}{\delta^2 + \Gamma^2/4} =: \frac{s_0}{1 + (2\delta/\Gamma)^2} \ , \tag{3.4.14}$$

with the on-resonance saturation parameter

$$s_0 = \frac{2|\Omega|^2}{\Gamma^2} = \frac{I}{I_\mathrm{s}} \ . \tag{3.4.15}$$

The saturation intensity is given by

$$I_\mathrm{s} = \frac{\pi hc}{3\lambda^3\tau} \ . \tag{3.4.16}$$

The excited state population is then

$$\rho_{22} = \frac{1}{2}(1-w) = \frac{s}{2(1+s)} = \frac{s_0/2}{1 + s_0 + (2\delta/\Gamma)^2} \ , \tag{3.4.17}$$

which saturates for high intensities I at $1/2$. Since the excitation rate equals the decay rate in steady state, we can finally write the scattering rate of photons from the laser field as [153, 162]

$$\Gamma_{\mathrm{p}} = \Gamma\rho_{22} = \frac{\Gamma}{2}\frac{s_0}{1+s_0+(2\delta/\Gamma)^2} \ . \tag{3.4.18}$$

3.4.3 The Scattering Force

The momentum of a photon is given $\hbar\mathbf{k}$, where $\mathbf{k}$ is the wave vector. When absorbing a photon, the momentum of the atom and the photon add up. The excited atom can then emit the photon in a random direction (spontaneous emission), where the momentum change of the atom is opposite to the momentum of the emitted photon. The force, acting on an atom, by scattering photons can then be described as the scattering rate times the momentum of a single photon [153, 162]

$$\mathbf{F}_{\mathrm{sc}} = \hbar\mathbf{k}\Gamma_{\mathrm{p}} = \hbar\mathbf{k}\Gamma\rho_{22} = \hbar\mathbf{k}\frac{\Gamma}{2}\frac{s_0}{1+s_0+(2\delta/\Gamma)^2} \ , \tag{3.4.19}$$

where $\mathbf{k}$ is the wave vector of the laser beam. Since the scattering rate becomes saturated at high intensities, the force has an upper limit of $\hbar k\Gamma/2$. Due to the randomness in direction of the emitted photon, the force is dissipative and irreversible. For a moving atom with velocity $\mathbf{v}$, we have to include the Doppler shift in the detuning as

$$\delta' = \delta + \delta_D = \delta - \mathbf{k}\cdot\mathbf{v} \ . \tag{3.4.20}$$

Cooling atoms with radiation pressure (scattering force) is limited to the Doppler temperature [162, 164]

$$T_{\mathrm{D}} = \frac{\hbar\Gamma}{2k_{\mathrm{B}}} \ , \tag{3.4.21}$$

which is 0.5 mK for the cooling transition of Ca^+ [141, 156]. The temperature of laser cooled atoms can reach values below the Doppler limit. Explanations can be given by sub-Doppler cooling mechanisms like Sisyphus cooling[153, 162]. Including these effects, the lowest reachable temperature with laser cooling is given by equating the kinetic energy resulting from the photon recoil with the kinetic energy, which leads to

$$T_{\mathrm{r}} = \frac{mv^2}{k_{\mathrm{B}}} = \frac{\hbar^2k^2}{k_{\mathrm{B}}m} \ , \tag{3.4.22}$$

where k is the wave constant of the beam, which amounts 3 μK for Ca^+

3.4.4 Cooling Scheme

Figure 3.4.1 illustrates the relevant energy levels for laser cooling of Ca^+. The cooling laser drives the optical transition from the electronic ground state $4s^2S_{1/2}$ to the excited state $4p^2P_{1/2}$ at a wavelength of 397 nm, with a transition rate of 1.36×10^8 s^{-1} [165]. However, the electron can also relax into the $3d^2D_{3/2}$ state with a transition rate of 9.45×10^6 s^{-1} and a wavelength of 866 nm. As the transition rate of the cooling laser is more than an order of magnitude larger, the ions will stay in this cycle most of the time and are cooled. However when the ion relaxes into the $3d^2D_{3/2}$ state, it needs to be excited back into the $4p^2P_{1/2}$ state to be further cooled. Therefore, to have an efficient closed optical cycle, two lasers are required for laser cooling of Ca^+: the blue cooling laser with a wavelength of 397 nm and the red repumping laser with a wavelength of 866 nm.

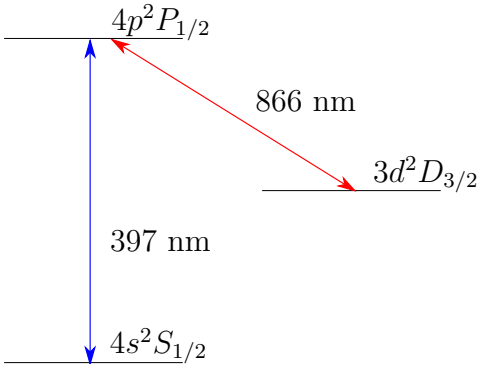

Fig. 3.4.1: **Laser Cooling Scheme of Ca^+.** The cooling laser drives the optical transition from the electronic ground state $4s^2S_{1/2}$ to the excited state $4p^2P_{1/2}$ at a wavelength of 397 nm. For the ions to stay in the cooling cycle, the population of $3d^2D_{3/2}$ state needs to be driven back into the cooling cycle, using a laser with a wavelength of 866 nm.

3.4.5 Coulomb Crystals

After laser cooling an ensemble of ions inside an ion trap, the ions form highly localized structures called Coulomb crystals. Such an ion Coulomb crystal is a form of ionic plasma with a strong coupling [141, 166]. When the potential energy between the ions is about a factor of 150 larger than their kinetic energy, a phase transition to a Coulomb crystal occurs as shown by theoretical simulations [166, 167]. By controlling the number of ions which are loaded into the trap and fine tuning the potentials, Coulomb crystals of several shapes from single ions over strings of ions to three dimensional spheroidal crystals can be obtained [7, 141]. The number of

ions in an experimental Coulomb crystal and their kinetic energies can be determined by comparison with molecular-dynamics simulations. Figure 3.4.2 shows the projections onto the X and Z axes of a simulated Coulomb crystal formed by 50 $^{40}Ca^{+}$ ions using the OpenMM package in C++.[1] The scattering force as introduced above was used to model the process of laser cooling. From the scattering rate for photons from the cooling laser, a scattering probability is calculated which is the rate times the time step. Depending on this probability a photon can be absorbed or not. Similarly, an excited ion can emit a photon via either spontaneous emission in a random direction or via stimulated emission in direction of the laser beam. The temperature (average kinetic energy divided by k_B) was around 3 mK. For this simulation, the fitted potentials in our trap (sec.3.5.2) were used with an RF voltage amplitude V_0 of 100 V, an RF frequency Ω of 10 MHz and a DC voltage U_{end} of 2 V resulting in Mathieu parameters of $a_x = -3.15 \times 10^{-4}$ and $q_x = 0.0813$. The laser power of the cooling laser was 0.5 mW with a Gaussian intensity profile and a 1/e radius of 180μm.

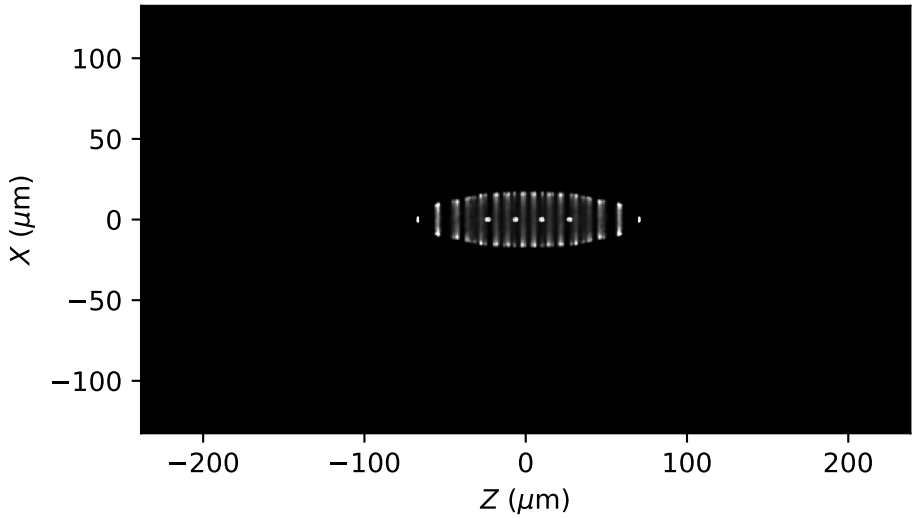

Fig. 3.4.2: **Simulated Coulomb Crystal.** Simulated Coulomb Crystal of 50 $^{40}Ca^{+}$ ions at a temperature of about 3 mK. An RF voltage V_0 of 100 V, an RF frequency Ω of 10 MHz and a DC voltage U_{end} of 2 V resulting in Mathieu parameters of $a_x = -3.15 \times 10^{-4}$ and $q_x = 0.0813$ were used.

[1]The simulation code was originally written by Ian Rouse.

3.4.5.1 Sympathetic Cooling of Molecular Ions

As the goal of the project is to investigate cold collisions by simultaneously trapping neutral molecules and molecular ions, it is essential to cool down molecular ions. A very flexible method of cooling molecular ions is sympathetic cooling [149], which was used to produce a Coulomb crystal of molecular MgH^+ and MgD^+ ions by Mølhave in 2000 [4]. Once one ion species can be cooled by laser cooling, another ion species such as molecular ions can be cooled sympathetically: While the laser cooled species acts as a cooling reservoir the other ion species can be cooled as they are strongly coupled by Coulomb interaction. Figure 3.4.3 shows a simulated Coulomb crystal of 100 $^{40}Ca^+$ ions (blue dots) and 10 sympathetically cooled N_2^+ ions with a mass of 28 u (red dots). The lighter sympathetically cooled N_2^+ ions form a string on the central axis of the trap. Heavier sympathetically cooled ions would form a shell around the lighter laser-cooled ions. The method of sympathetically cooling is most efficient, if the two ion species are similar in mass-to-charge ratios m/z in which case secular temperatures of around 10 mK have been achieved [150].

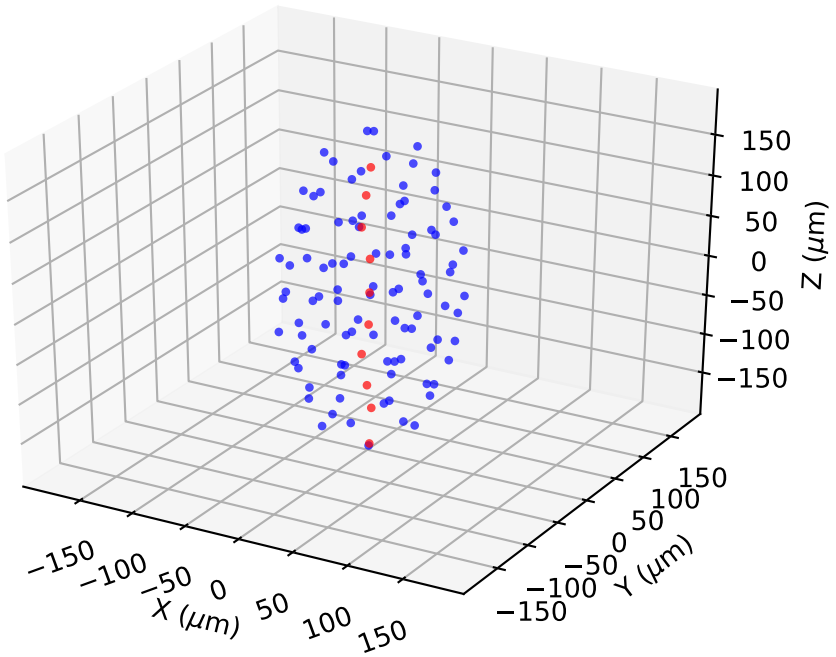

Fig. 3.4.3: **Sympathetic Cooling of N_2^+.** A simulated crystal of 100 cooled $^{40}Ca^+$ (blue dots) and 10 sympathetically cooled $^{14}N_2^+$ (red dots) is shown. The sympathetically cooled N_2^+ ions form a string on the central axis of the trap.

3.4.6 Laser Setup and Imaging

The laser setup is separated into two parts: the ionization of Ca and laser cooling of Ca^+. Fig. 3.4.4 shows schematics of this setup. All the mirrors (M) are aluminium mirrors. (HWP) are half-wave plates which are used to adjust the polarizations of the laser beams and (BS) are beam stoppers. All the lasers access the ion trap center via Brewster windows (BW). The blue dot illustrates a Coulomb crystal in the ion trap center. Note that the ion trap is off-center in the chamber, not in a direct line with the decelerator.

On the right side there are the ionization lasers. The light from the diode laser (423 nm DL, Toptica DL 100) with a wavelength of 423 nm (cyan line) reaches the setup via an optical fiber. The beam passes a half-wave plate (HWP) and is focused into the ion trap center with a lens (L1, f = 500 mm). The second laser for the ionization comes from a free-running laser diode (375 nm LD, L375P70MLD, Thorlabs) with a wavelength of 375 nm. A few percent of the power from this light are overlapped with the 423 nm light using a glass plate, while the rest of the light is blocked with a beam stopper (BS). As the ionization lasers are only used to load the ion trap, they are blocked with a beam stopper (BS*) during the experiments.

The left side shows the setup of the cooling lasers. Laser light at a wavelength of 397 nm (blue line) is provided by a diode laser (397 nm DL, Toptica DL 100) and reaches the setup via an optical fiber. It passes a half-wave plate (HWP) and is focused via a lens (L3, f = 75 mm) through a pinhole with a diameter of 100 μm in order to cut off higher transversal electromagnetic modes (TEM) and provide a clean Gaussian beam. The beam is collimated with another lens (L4, f = 75 mm). The repumping laser with a wavelength of 866 nm (866 nm DL, Toptica DL 100) reaches the setup via an optical fiber as well. It passes a half-wave plate (HWP) and is overlapped with the laser light at a wavelength of 397 nm on the dichroic mirror (M2). Both cooling lasers are focused into the ion trap center with a lens (L2, f = 500 mm).

The imaging of the ions fluorescence (blue line from the trap center towards the camera) is achieved using a low-light camera (Luca R 604, Andor) [168] using electron multiplying (EMCCD) technology. The CCD sensor has 1004×1002 pixels with a pixel size of 8×8 μm^2. The camera was used in combination with an objective lens (O, EDF20052, Nikon) which has a numerical aperture (NA) of 0.14, a working distance of 64 mm and a focal length of 42.3 mm. In order to reduce stray light reflected from the surface of the electrodes and the cryogenic assembly,

an optical band pass filter (F, FBH400-40) was used with a transmission window of 400 ± 40 nm. The typical magnification used in the experiments in this thesis is around $M = 8$.

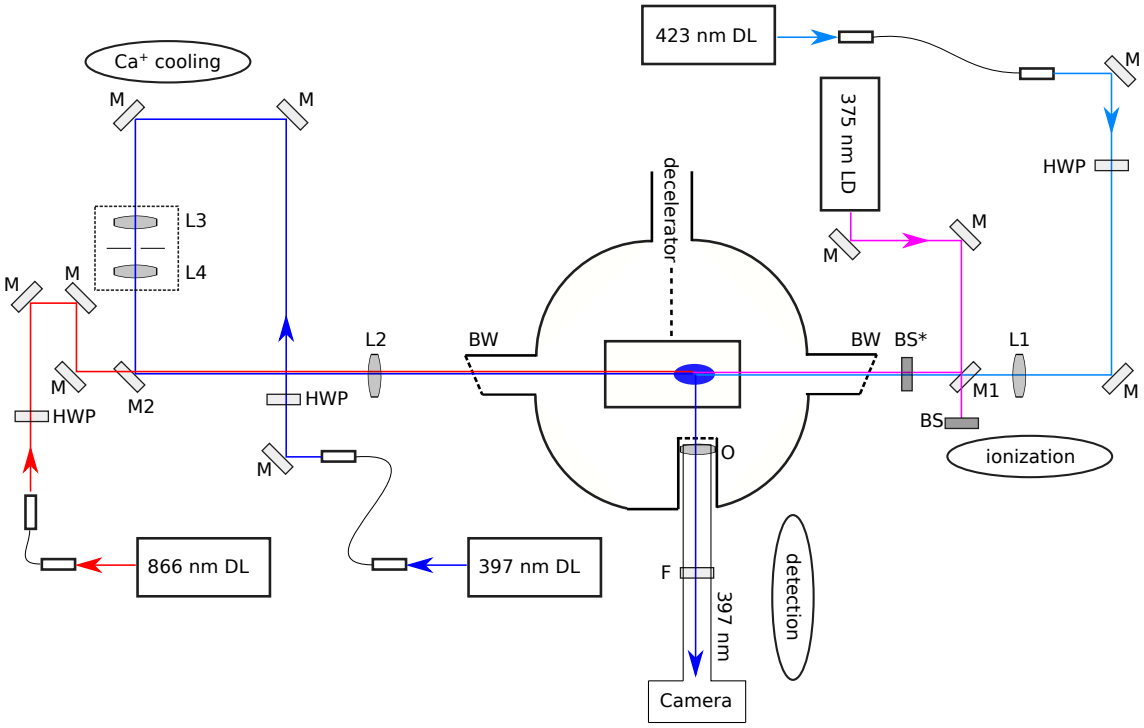

Fig. 3.4.4: **Laser Setup and Imaging.** The laser setup is separated into two parts: the ionization of Ca and laser cooling of Ca^+. (M) are mirrors, where M1 and M2 are dichroic mirrors. (HWP) are half-wave plates which are used to adjust the polarizations of the laser beams and (BS) are beam stoppers. All the lasers access the ion trap center via Brewster windows (BW). The blue dot illustrates a Coulomb crystal in the ion trap center. Note that the ion trap is off-center in the chamber, not in a direct line with the decelerator. For imaging of the ions the fluorescence light is collected with an objective onto the CCD chip of a low-light camera.

3.5 Thin Wire Ion Trap

The constraints for the size of the ion trap are similar to those for those of the stopping assembly in the magnetic trap.

Figure 3.5.1 shows technical drawings of our ion trap, where the coordinate system is shown with magenta arrows. For the RF electrodes, we use the same type of thin wires as in the neutral stopping part, namely stainless steel wires with a diameter of 0.2 mm, producing a quadrupolar potential. These are arranged in a quadratic configuration with center-to-center distances between the wires of 2.0 mm as shown

in the inset of fig. 3.5.1. The diagonal distance between the surface of an RF electrode to the trap center is then $R = \sqrt{2}$ mm $-$ 0.1mm $=$ 1.314 mm. For the endcaps we use stainless steel tubes with an inner radius of 0.8 mm and an outer radius of 1.0 mm. The distance from the trap center to each endcap is $z_0 = 2.5$ mm. The main advantages of such a thin wire ion trap are a very compact design as well as a large amount of optical access. Furthermore Ray et al. [169] trapped Rb^+, where they also used thin wires as endcap electrodes. Their design was motivated by [170] in which a magneto-optical trap (MOT) was superimposed with an electrostatic trap to trap ultra cold polar NaCs molecules at translational temperatures of $\approx 200\mu$K. Cryogenic ion traps have been built before and used e.g. to trap sympathetically cooled highly charged ions [171, 172, 173].

In the following sections, we first discuss the electrostatic shielding of the ion trap from the high voltages pulsed in the magnetic trap assembly. Subsequently, the potentials produced by the trap shown in fig. 3.5.1 will be analyzed, the electronics to produce these potentials in an experiment are described and experimental results of trapping of Ca^+ will be presented. All electrostatic potentials are produced in a finite element method (FEM) using COMSOL Multiphysics© v. 5.3[174].

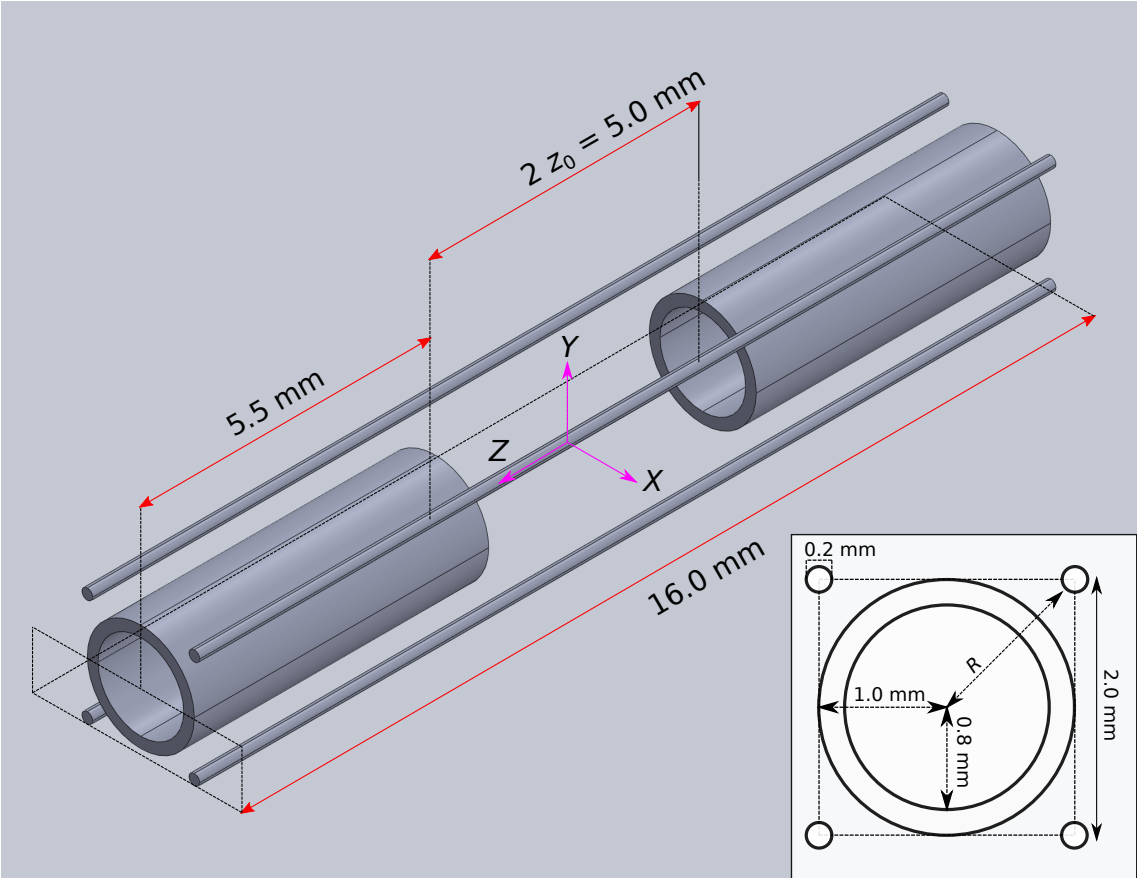

Fig. 3.5.1: **Technical Drawing of the Thin Wire Ion Trap.** The ion trap consists of four wires where RF potentials are applied to produce a quadrupolar field for confinement of an ion along the X and Y direction. The have a diameter of 0.2 mm and are spaced in a square configuration with a size of 2×2 mm as shown in the inset. The radial distance from the trap center to the surface of an electrode is $R = 1.314$ mm. Two endcaps with applied DC voltage allow for confinement along the Z axis. They have a length of 5.5 mm and are separated along the Z axis by $2z_0 = 5.0$ mm. The coordinate system is shown with magenta arrows.

3.5.1 High-Voltage Shielding

To allow for simultaneous operation of ion trap and magnetic trap, the ion trap needs to be shielded from the high-voltage pulses which are used to stop the neutral molecules in the magnetic trap assembly.

Fig. 3.5.2 shows a technical drawing of the hybrid trap setup, where the coordinate system is represented by magenta arrows and originates in the ion trap center (5). The right part shows the magnetic trap assembly, as presented in sec. 2.4.5, with four stopping wires and two magnets. The labels mark several points of interest along the shared trap axis Z in the analysis of the shielding. (1) is the end of the lower pair of wires, (2) the end of the upper pair. Label (3) marks the beginning of the first ion trap endcap, when looking from the magnetic trap assembly. (4) is the other end of that endcap, (5) is the ion trap center, (6) is the beginning of the next endcap and (7) marks the end point.

The potentials during a high voltage pulse of the stopping wires on the right of fig. 3.5.2 were numerically calculated, applying voltages of ± 5.8 kV on the back wires ($X < 0$) and magnets and ± 2.3 kV on the front wires ($X > 0$) as discussed in sec. 2.4.2. The plates around the ion trap are electrostatically grounded, whereas the front plate has a slit with a width of 500 μm to allow for loading of Ca atoms from the Ca oven. The most important quantity is the residual electrostatic potential in the ion trap. Fig. 3.5.3 shows the results from the numerical calculations. Graph a) shows the residual potential along the Z line where the black curve is the case without shielding and the red line shows the shielded case. The labels on the vertical lines match to the points of interest introduced above. While in the unshielded case, the residual electrostatic potential is on the order of several volts, the shielded case results in residual electrostatic potential below 1 mV. This is an improvement of three orders of magnitudes in the trap center. Graph b) shows a contour plot of the residual potential along the X and Y axes in the trap center $Z = 0$. The residual potential is mainly caused by the imperfect shielding from the front plate, due to the slit for the loading of Ca atoms. As these residual electrostatic potentials are on the order of the fluctuations of the trap electronics, the shielding achieved with this configuration is sufficient.

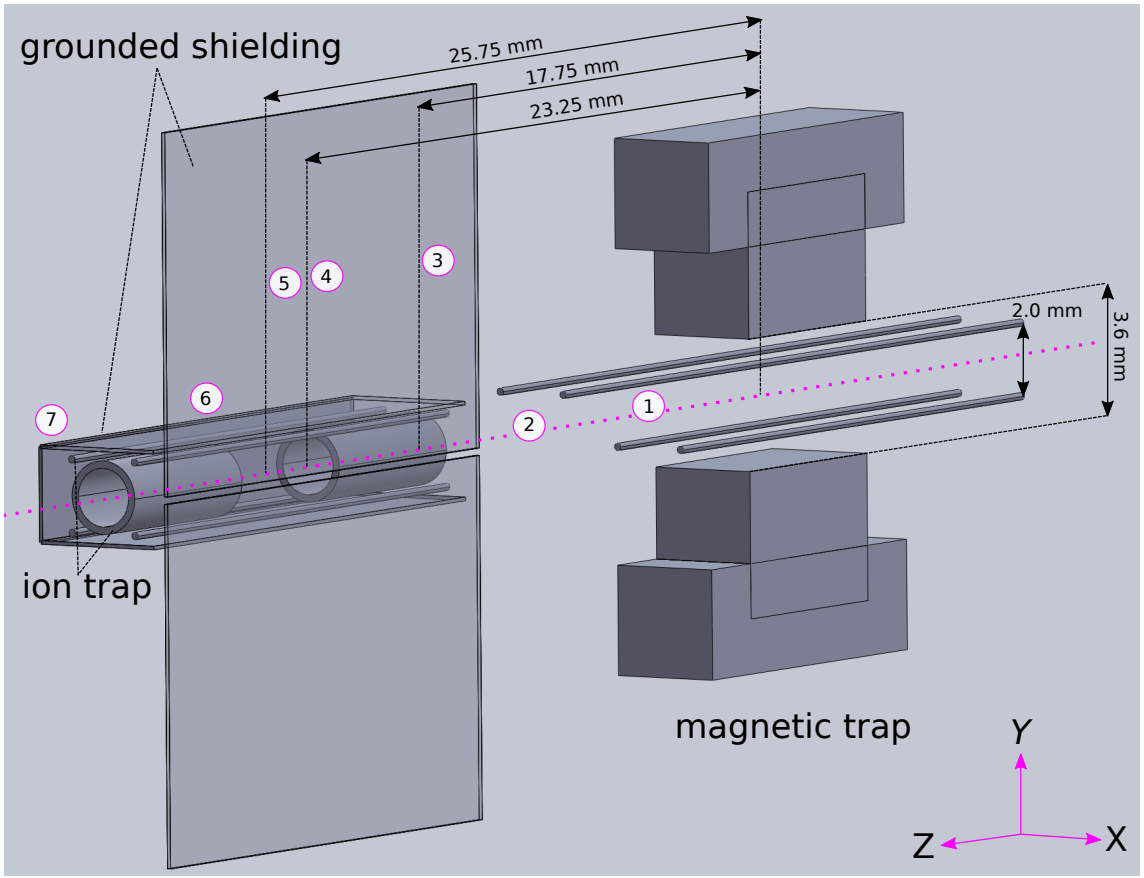

Fig. 3.5.2: **HV Shielding of the Ion Trap.** The magnetic trap assembly, consisting of four stopping wires and two magnets with stainless steel holders is shown on the right. On the left, the ion trap is shown, consisting of four wires and two endcap tubes. The ion trap is shielded from the high voltages on the magnetic trap assembly using four shields which are electrostatically grounded. The front shield has a has a slit with a width of 200 μm to allow for loading of Ca atoms from the Ca oven. (1) is the end of the lower pair of wires, (2) the end of the upper pair. Label (3) marks the beginning of the ion trap endcap, which is closer to the magnetic trap assembly. (4) is the end of that endcap, (5) is the ion trap center, (6) is the beginning of the next endcap and (7) marks the end point. The coordinate system is represented by magenta arrows and originates in the ion trap center (5).

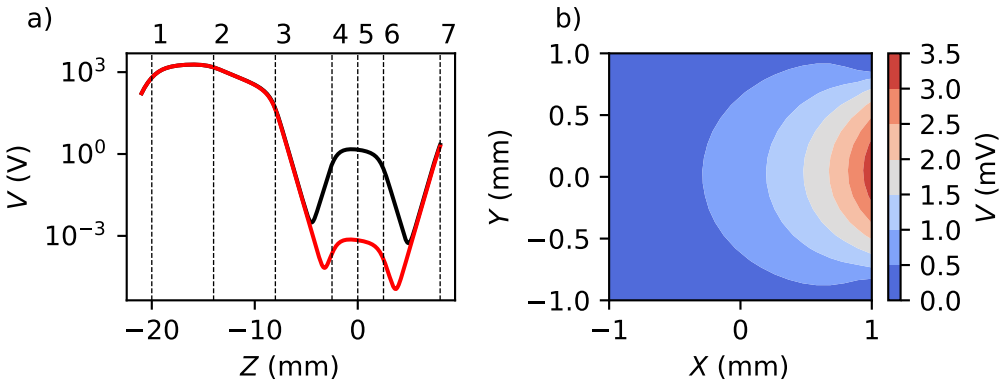

Fig. 3.5.3: **Residual Potential.** The residual electric potential from the magnetic trap assembly is shown in proximity of the ion trap center. Graph a) shows the potential along the Z axis for the unshielded case (black line) and the shielded case (red line). The shielding reduces the residual electric potential by three orders of magnitude to less than 1 mV in the shielded case. Graph b) shows the same potential at $Z = 0$ in radial direction, along the X and Y axes. Most of the residual potential reaches the trap through the slit in the front plate on the ion trap.

3.5.2 Trap Potentials

This section covers a numerical analysis of the electrostatic potentials, produced by the electrodes shown in fig. 3.5.1. To be able to use the stability parameters a_u and q_u as described in sec. 3.2, we introduce geometrical parameters for both stability parameters.

3.5.2.1 Endcap Potentials

Fig. 3.5.4 shows the electrostatic potentials in proximity of the trap center produced by the endcaps in the ion trap, calculated by FEM. The graph on the left shows the radial component along the X- and the Y-axis in the trap center at $Z = 0$. The potential shows an anti-trapping behavior in radial direction, meaning that the electrostatic potential decreases as the radial coordinate increases or, in other words, has a maximum along the Z-axis. The graph on the right shows the axial behavior, where the potential is plotted along the X and the Z axes at $Y = 0$. As the electrostatic potential produced by both endcaps is symmetric along the Z-axis around $Z = 0$, the data is shown for $Z > 0$. The potential has a trapping behavior along the Z-axis, which means that there is a minimum in the trap center.
In the derivation of the stability parameters for a_u the electrostatic potential in proximity of the trap center produced by the endcaps U_{end} was assumed to be of quadrupolar shape as shown in eq.(3.2.7). Fig. 3.5.5 shows the numerical potential along the Z-axis at $X = Y = 0$ as black dots. The potential from eq.(3.2.7) using $\kappa = 1$ is shown as a black line. As the potential does not decrease to zero in the center, an offset was added. By fitting this function with an offset fitting parameter to the numerically calculated potential κ can be determined by using it as a fitting parameter. From a full three dimensional fit, we extract $\kappa = 0.404(2)$ and relative offset potential of 0.0628(1). The resulting fitted potential is shown as a red line in fig. 3.5.5. Similar approaches can be found e.g. in [155, 159].

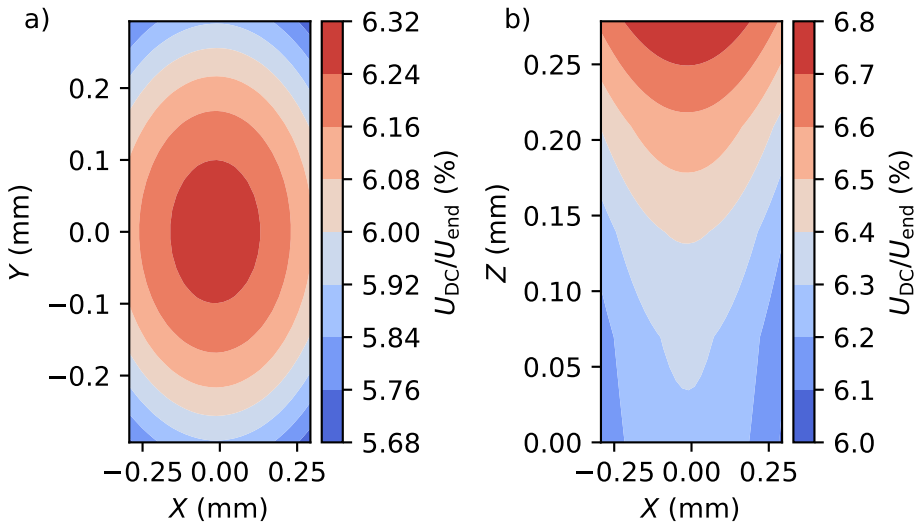

Fig. 3.5.4: **Endcap Potentials.** The graph a) shows the potentials along the radial axes X and Y at $Z = 0$. Visible is a maximum in the trap center, leading to an anti-trapping behavior along the radial components. The graph b) shows the same potential along the Z and X axes at $Y = 0$. The potential shows a minimum in the trap center along the Z axis, leading to axial confinement.

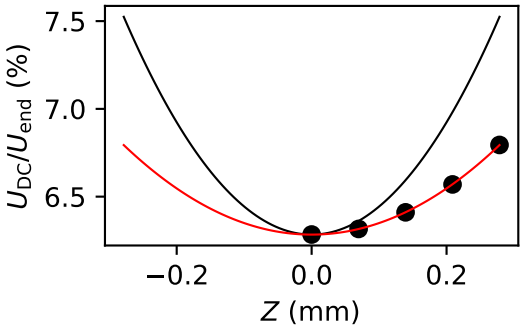

Fig. 3.5.5: **Geometric factor κ.** The potential produced by applying 1 V to the endcaps is shown along the Z axis in the radial center at $X = Y = 0$ as black dots. The black line shows the potential which is assumed in the derivation of the a_u stability parameter with the geometric factor $\kappa = 1$ and an offset added. The red line shows the same function with a fitted κ parameter extracted from a full three dimensional fit: $\kappa = 0.404$.

3.5.2.2 RF Potentials

Fig. 3.5.6 shows the electrostatic potential produced by the thin wires in the ion trap when applying voltages of ±1 V: 1 V the the left wire on top and the right wire on the bottom and −1 V to the other pair. The result is a quadrupolar potential with a minimum in the trap center along the Z axis allowing for radial confinement. Mathieu's differential equation is valid for hyperbolically shaped electrodes. It is however much more convenient to use cylindrical electrodes, which are also easier to manufacture. To reproduce the quadrupolar potential from such electrodes using cylindrical electrodes, the radial distance r_0 as defined in fig. 3.2.1 and the radius r_e of the cylindrical electrodes should be in a relation of $r_\mathrm{e}/r_0 = 1.1468$ [175]. The trap in this work, however, has a ratio of 0.076. To calculate meaningful q_u stability parameters, a geometric factor can be introduced, similarly to the endcap case. Instead of using the radius $R = 1.314$ mm from fig. 3.5.1 directly to calculate q_u, a geometrically corrected parameter r_0 can be extracted, similarly to the κ parameter for the endcaps. The function in eq.(3.2.5) can be fitted to the numerical potential from the FEM to extract an effective radius r_0 which can then be used for the stability parameters. Fig. 3.5.7 shows the numerical data points along the X axis at $Y = Z = 0$ as black dots. Using $r_0 = R$ produces the potential shown by the black line. The fitted potential is shown as a red line and gives the parameter $r_0 = 1.734(1)$ mm for our trap. With the geometric parameters κ and r_0 we can finally describe our trap with a stability diagram using Mathieu's stability parameters.

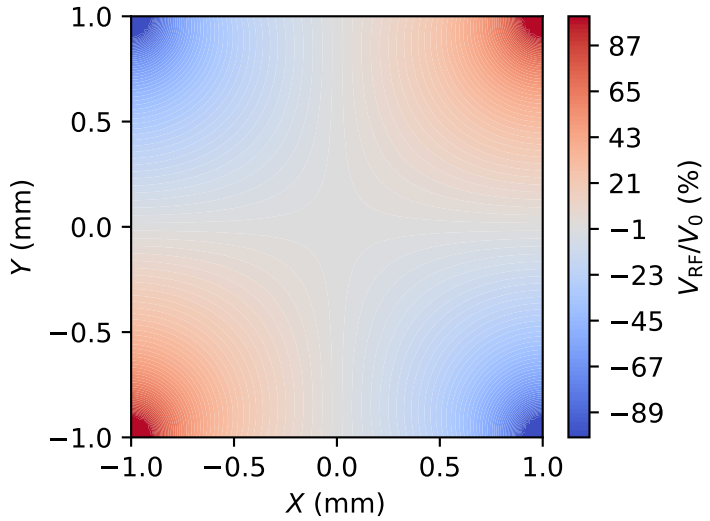

Fig. 3.5.6: **RF Potential.** The electrostatic potential produced by the thin wire electrodes is shown along the X and Y axes. The same voltages were applied to diagonal pairs of electrodes: 1 V the the left wire on top and the right wire on the bottom and -1 V to the other pair. The result is a quadrupolar potential with a minimum in the trap center along the Z axis allowing for radial confinement.

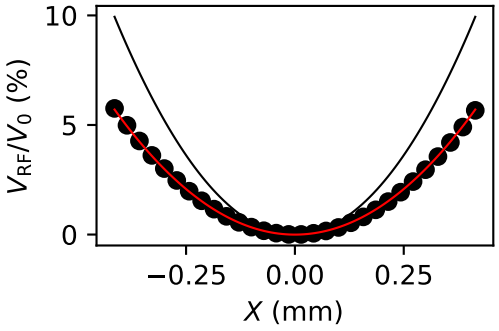

Fig. 3.5.7: **Geometric Factor in the RF Potential.** The electrostatic potential from the thin wire electrodes (FEM) is shown along the X axis at $Y = Z = 0$ as black dots. The black line shows the potential assumed in the derivation of the stability parameters using $r_0 = R = 1.314$ mm. The red curve shows the potential which is produced by using a fitted effective radius $r_0 = 1.734$ mm which can be used to calculate the stability parameters.

3.5.2.3 Effective potential

The effective potential V_{eff} as described by eq. (3.2.21), which is a good approximation for low q_u parameters is analyzed in order to estimate the trap depths. The effective potential along the radial components X and Y is shown in fig. 3.5.8 at $Z = 0$, using the numerical potentials from the FEM. The potentials were calculated for amplitudes of 1 V and scaled by the parameters V_0 and U_{end} respectively. The trap parameters were the amplitude of the RF voltage $V_0 = 100$ V, the endcap voltage $U_{\text{end}} = 2$ V the RF frequency $\Omega = 10$ MHz. The resulting effective potential shows a radially confining shape and is not perfectly radially symmetric. This radial asymmetry comes from the grounded shields, as discussed in sec. 3.5.2.1.
Figure 3.5.9 shows the trap depths along the X-axis and Y axis as a black line and red line. These were calculated by subtracting the minimum of the potential from the maximum along the X and Y axis for several points along the Z axis. The trap is slightly deeper along the X axis, since the HV shielding has a larger distance along this direction. The trap depth has a maximum in the trap center and decreases as Z increases. This is due to the anti-trapping behavior of the endcap potential in radial direction which increases for smaller distances to the endcaps.

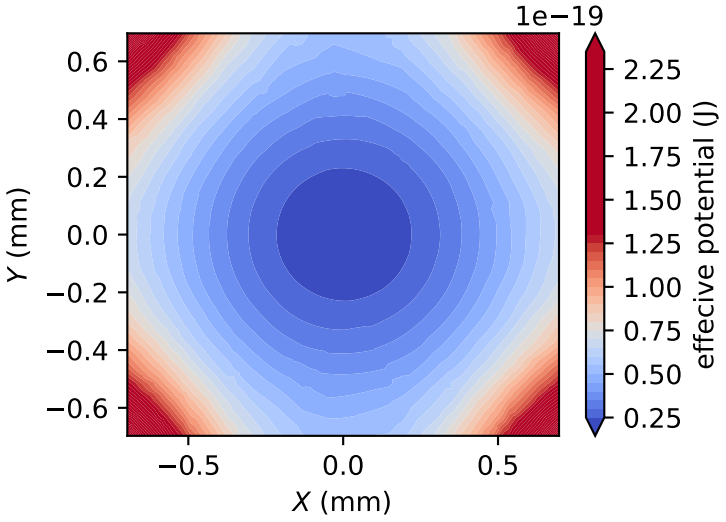

Fig. 3.5.8: **Effective Potential.** The effective potential using the numerical potentials (FEM). The trap parameters were $V_0 = 100$ V, $U_{\text{end}} = 2$ V and $\Omega = 10$ MHz. The resulting effective potential shows a radially confining shape and is not perfectly radially symmetric. This radial asymmetry comes from the grounded shields which are used to protect the trap center from the high voltages which are switched in the magnetic trap assembly.

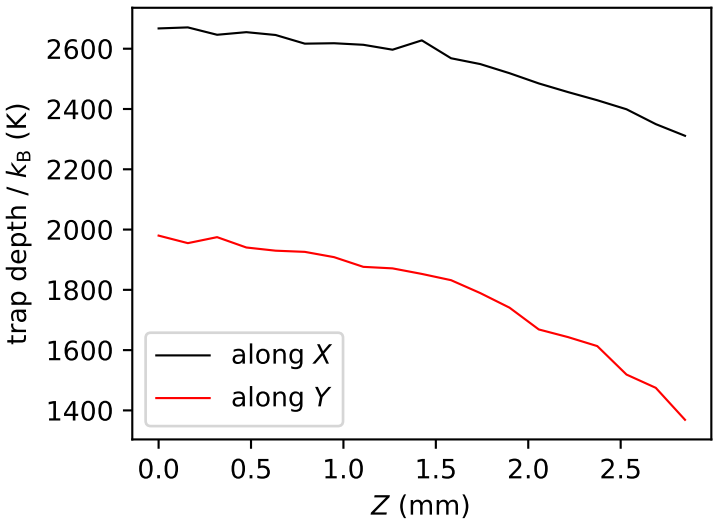

Fig. 3.5.9: **Trap Depth.** The trap depths were calculated using the effective potential. The trap is slightly deeper along the X axis (black line) than along the Y-axis (red line), since the HV shielding has a larger distance along this direction. The trap depth has a maximum in the trap center and decreases as Z increases. This is due to the anti-trapping behavior of the endcap potential in radial direction which increases for smaller distances to the endcaps.

3.6 Electronics

3.6.1 RF Wires

To produce the RF voltages, a home built RF generator was employed, based on a resonating LC circuit [176]. The RF frequency Ω was adjustable in a range of 5 - 10 MHz with amplitudes between 0 to 600 V using a low noise DC power supply (MCP 140-650, FUG).

Due to imperfections on the RF electrodes and charges accumulating on the insulator holders for the wire, the effective center generated by the electrodes is not necessarily the geometric center of the trap. This could result in the ions being trapped in a radial offset which would mean that they experience excess micromotion. This can ultimately prevent trapping of Coulomb crystals. Therefore, a RF-DC mixing box was built to allow adding a DC offset voltage to each separate RF electrode.[2]

Fig. 3.6.1 shows the circuit diagram of the RF/DC voltage mixing box. The electric current on the DC input (1) is limited using a first resistor of 1 kΩ (2). The reference potential (ground) is coupled in via a resistor of 1 MΩ (3). Then a low-pass (LP) filter consisting of two RC filters in series ($R = 10$ MΩ, $C = 3.3$ nF) cleans the DC voltage from noise over 2.4 Hz and prevents RF voltage from reaching the DC input. The RF voltage is coupled in via a capacitor (100 nF) to prevent the DC voltage being fed back to the RF generator. The output (6) gives the RF voltage with the DC voltage as an offset.

Fig. 3.6.2 shows the output of the RF/DC mixing box, where a DC voltage of 10 V was added to an RF voltage with a zero-to-peak amplitude V_0 of 100 V and a frequency of $\Omega = 8.3$ MHz. The black dots are the data points measured on an oscilloscope and the red curve is a fit of a scaled sine function which gives us a fitted offset of 6.3(1) V with an RF frequency of 8.30(3) MHz and an RF amplitude of 103.8(1) V.

3.6.2 Endcaps

As the trap set up in the chamber limits the distance that can be achieved between the cables providing the RF voltage to the thin wire electrodes and the cables which provide DC voltage to the endcap electrodes, the RF frequency can be picked up on the endcaps. This can lead to axial heating of trapped ions and can make crystallization impossible. Thus, an RC filter (LP) was used to suppress the RF

[2]The RF-DC mixing was based on the design developed by G. Hegi in our research group.

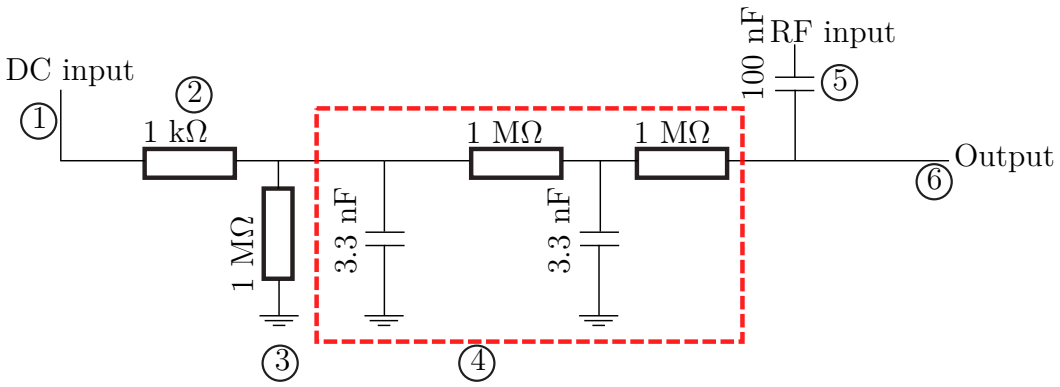

Fig. 3.6.1: **RF/DC Mixing Circuit Diagram.** The electric current on the DC input (1) is limited using a first resistor of 1 kΩ (2). The reference potential (ground) is coupled in via a resistor of 1 MΩ (3). Then a LP filter consisting of two RC filters in series ($R = 10$ MΩ, $C = 3.3$ nF) cleans the DC voltage from noise over 2.4 Hz. The RF voltage is coupled in via a capacitor (100 nF) to prevent the DC voltage being fed back to the RF generator. The output (6) gives the RF voltage with the DC voltage as an offset.

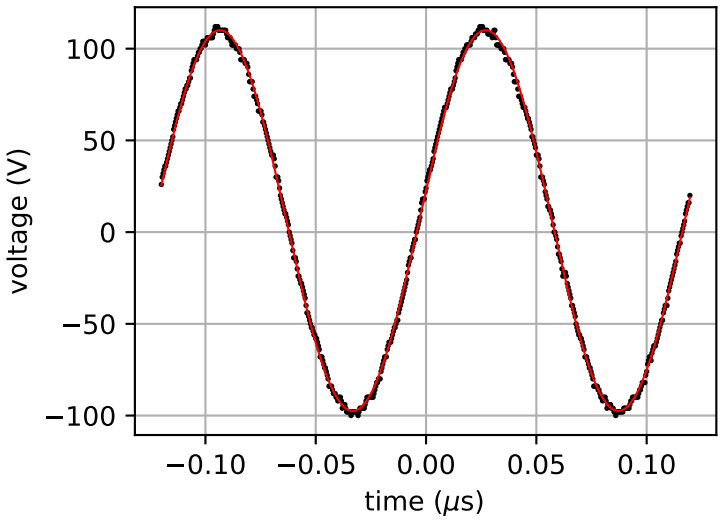

Fig. 3.6.2: **RF Voltage with DC offset.** The measured RF voltage (100 V amplitude, frequency of 8.3 MHz) with a DC offset (10 V) is shown as black dots. The red line shows a fitted sine model giving a fitted offset voltage of 6.3(1) V, a RF frequency of 8.30(3) MHz and a RF amplitude of 103.8(1) V.

voltage on the end caps. This was achieved by placing capacitors with a capacity C of 100 nF close to the end caps in a distance of about 6 cm. The capacitors connect the wires, which provide the voltages to the endcap, to the copper body which is grounded. Resistors can be placed outside of the vacuum. Using a resistance R of 1 kOhm leads to a cutoff frequency f of $f = \frac{1}{2\pi RC} = 1.59$ kHz, where the RF

frequency is on the order of 10 MHz.

Fig. 3.6.3 shows the voltage as measured directly on the endcaps for testing purposes. A home built DC voltage provided the voltage for the endcaps and was set to 10 V. Simultaneously, RF voltage with an amplitude of $V_0 = 200$ V and a frequency of $\Omega = 8.3$ MHz was applied to the RF electrodes. The black curve shows the resulting voltage on the endcap without the RC filter and the red curve shows the filtered voltages. The noise on the endcap voltage was reduced from (peak-to-peak) 0.57 V to 0.19 V. The standard deviation was reduced by a factor of 4 to 0.036 V.

The frequency of the noise in the unfiltered circuit is an unclear superposition of many frequencies. A power spectrum from the measured data did not give more insight. In the cleaned circuit, the RF frequency of 8.3 MHz and overtones is clearly visible and shown by power spectra.

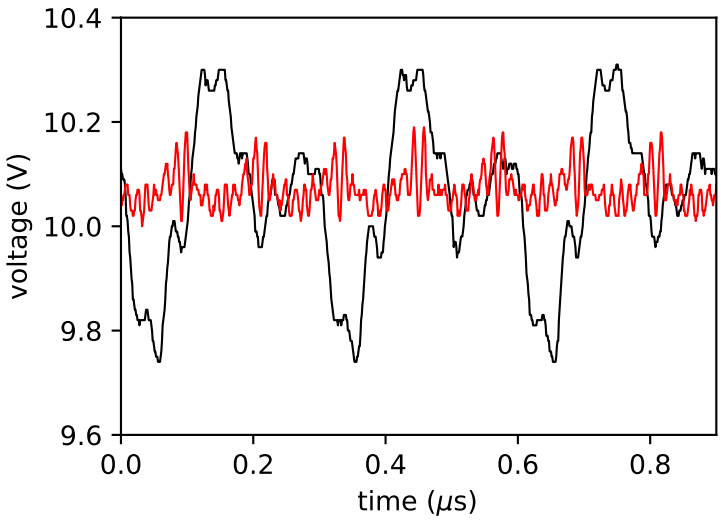

Fig. 3.6.3: **Noise Filter on Endcap.** A RC filter was used to suppress the RF voltage picked up on the end caps. The resistance R was 1 kOhm and the capacity C was 100 nF, leading to a cutoff frequency f of 1.59 kHz. A DC voltage of 10 V was applied to the endcaps and an RF voltage with an amplitude of $V_0 = 200$ V and a frequency of $\Omega = 8.3$ MHz was applied to the RF electrodes. The black curve shows the resulting voltage on the endcap without the RC filter and the red curve shows the filtered voltages.

3.7 Trapping of Ca^+ Coulomb Crystals

The measured pressure in the trap chamber was on the order of 6×10^{-11} mbar with trap temperatures of around 20 K. This resulted in clear images of Ca^+ Coulomb crystals with trap lifetimes of hours. To correct imperfections from the trap electrodes and push the ion crystals to the trap center, offset DC voltages on the order of 10 mV where applied to the RF electrodes, depending on the trap settings via the RF/DC voltage mixing box as described in sec. 3.6.1.

Fig.3.7.1 shows false-color images of the fluoresence of trapped Ca^+ Coulomb crystals. The magnification of the imaging system was about 8, resulting in a resolution of about 1 μm per pixel. The cooling laser had a power of 0.2 mW at a wavelength of 396.959205 nm and the frequency was locked to a wavelength meter (WS-7, High Finesse). The pumping laser at a wavelength of 866.451580 nm had a power of 2.7 mW where the frequency was locked as well (WSU-30, High Finesse).

Image a) shows a crystal of 19 Ca^+ ions forming a string along the Z-axis. The endcap voltage U_{end} was set to 0.34 V and the amplitude of the RF voltage was 242 V (zero to peak) at an RF frequency of 10.69 MHz. Image b) shows the corresponding simulation leading to a temperature along the laser axis Z of around 1 mK. The experimentally measured length of the ion string was 274 μm and the simulated length was 272 μm, showing a good agreement within 1 %. A good agreement between the simulation and the experiment is important for future experiments of cold collisions in the hybrid trap: the number of ions in the crystal is planned to be determined via comparison with simulations. Image c) shows a larger Coulomb crystal of 38 trapped Ca^+ ions. The exact ion number was measured by forming an ion string from this crystal. In comparison to image a), only the amplitude of the RF voltage was changed to 85 V. Image d) shows the simulation of 38 Ca^+ ions at these settings. The agreement is not as good as in images a) and b). However, it is safe to assume a relative error of about 5 % which is ± 2 ions in this case and the translational temperature of the trapped ions was at around 1.5 mK.

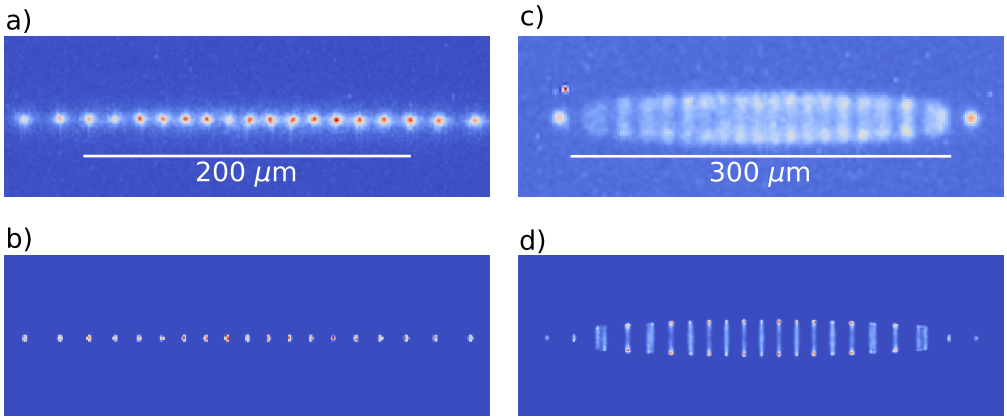

Fig. 3.7.1: **Trapped Ca^+ Coulomb Crystals.** False-color images from the fluorescence of laser-cooled and trapped Ca^+ ion crystals are shown. Image a) shows a string along the Z axis of 19 ions and image b) shows the corresponding simulation. A larger crystal of 38 Ca^+ ions is shown in c) with the simulation d). From the simulation an ion number of 38(2) can be estimated by comparison to the experimental image.

3.8 Conclusion and Outlook

This chapter presented the complete design and development of the cryogenic ion trap as a part of a new type of hybrid trap.
A source of Ca atoms was constructed, where the biggest problem was a reliable functionality under cryogenic conditions. A beam of Ca atoms was provided by resistive heating of a tube filled with Ca powder. These atoms were detected in the ion trap region by collection of the fluorescence with a wavelength of 423 nm.
An ion trap with a strong optical access was designed, consisting of four thin wire electrodes to provide radial confinement and two endcap electrodes for axial confinement. The decision to use hollow tubes for endcap electrodes was directly influenced by the requirement for the transport of cold neutral molecules by moving the magnetic trap over the ion trap.
A strategy to shield the ion trap from residual electrostatic potentials of the high voltage pulses was presented. Therefore, the ion trap was shielded in the radial directions with thin grounded plates while being open along the axial direction to still allow for a transport of neutral molecules in the future.
The final potentials, created in the ion trap, were analyzed by FEM. The shape of the RF electrodes deviates strongly from hyperbolic electrodes, but the created potentials can still be approximated as such in proximity of the trap center. To be able to use the same stability diagram and stability parameters in a meaningful way, geometrical parameters were calculated. These parameters correct for the deviation from perfect hyperbolic electrodes for the electric potentials in axial direction κ and radial direction r_0.
An optical setup was built to allow for ionization of Ca atoms by using a diode laser with a wavelength of 423 nm and a free-running laser diode at a wavelength of 375 nm on one side of the trap chamber. On the other side the lasers which are used for cooling of Ca^+ ions were set up: the cooling laser with a wavelength of 397 nm and the repumping laser with a wavelength of 866 nm. Additionally an imaging setup was built, consisting of a camera objective, an optical bandpass filter and a low-light camera.
The electronics to provide the required RF and DC voltages were developed and tested. The noise on the voltage on the endcaps was successfully reduced with an RC filter. A RF/DC mixing box was constructed, to allow for applying offset DC voltages on the RF electrodes. This is necessary in order to correct the potentials of the trap and ensure to trap the ions in the center of the trap.

As a final result, the functionality of the trap was shown by trapping Coulomb crystals of laser cooled Ca^+ ions. A software, similar to the software in the magnetic trap, was written to allow for quick operation of the ion trap and imaging of the ions. The ion traps were imaged and compared to simulations. Due to the good agreement between the experimental and the simulated images, the simulation can be used to estimate the number number of ions as well as the kinetic energies in experiments of cold collisions of hybrid systems. The agreement between the simulation and the experiment can be improved by adjusting a constant heating force of the ions. However, blurring effects in the imaging system have to be ruled out before a perfect agreement can be achieved.

The next step towards hybrid trapping of neutral molecules and ions is to superimpose the magnetic trap with the ion trap. This will be achieved by moving the magnetic trap after loading. The next chapter focuses on hybrid trapping and the mechanism for the transport of the neutral molecules.

Chapter 4

The Hybrid Trap

In the previous chapters, the two components needed to build a hybrid trap were presented: We built a cryogenic assembly which successfully allowed trapping of neutral OH molecules and Ca^+ ions in separate traps on the same assembly. The long-term goal of studying reactions between these neutral and ionic species, however, requires the two trap centers to be superimposed: hybrid trapping.

This chapter presents our implementation of the hybrid trap. Therefore, we move the permanent magnets in the magnetic trap towards the ion trap, to achieve hybrid trapping by overlapping both traps. This chapter covers the development of this main element to achieve hybrid trapping and shows a characterization of the current state.

By combining strong magnetic fields with large gradients with an ion trap, new problems can arise which will be discussed. Thus, our magnetic trap is theoretically analyzed. The strong magnets in the neutral trap cause a large shift in the Zeeman energy of the magnetic sublevels in the ionic species ($^{40}Ca^+$), which can cause problems in laser cooling.

The interaction time of the ionic species and the neutral species will be analyzed by comparing the overlap over time to the case of an experiment where an ion trap is placed behind a Stark decelerator.

4.1 Magnet Transport

In order to superimpose both ionic and magnetic trap, the magnetic trap is moved towards the ion trap. Fig. 4.1.1 shows technical drawings of the assembly. A cryogenic motor (1) (VSS 19.200.1.2-UHVC2-KTC, Phytron) rotates a ball screw made of stainless steel (2). The magnet holder (3) contains a spindle nut and is placed on a sled on a rail guide (MN 7-055-G1-V1 and MNNS 7-G1, Schneeberger) made of stainless steel (4). The cryogenic stepper motor rotates the ball screw which moves the magnet holder on the rail guide allowing a translation of the magnetic trap from the stopping wires for the neutral molecules (5) to the ion trap (6) and back.
The operation of the transport was tested and worked. In vacuum and room temperature conditions, the motor worked on the order of 10 cycles in 60 seconds, moving the magnets to the ion trap and back, which was limited by the amount of heat which can be removed under vacuum conditions. The motor, however, is designed to be operated at temperatures around 77 K where the heat is efficiently removed by the cryo-cooler. For operation in hybrid trapping experiments, the repetition cycle of the magnet transport will be below 0.1 Hz. Fig. 4.1.2 shows exemplary the temperature development during 100 repetitions of moving the magnets from the starting position to the ion trap center and back. This test was done under standard conditions for temperature and pressure. The motor increased about 6 K in temperature. Under cryogenic conditions, the temperature increase was found to be on the same order. However, under normal pressure the heat dissipation is higher. On the other hand, the experimental repetition cycle for collision experiments will be lower, making the heat production of the motor a negligible problem.

4.1.1 Home Switch Electrode

When operating a stepper motor, single steps can be skipped, especially when the motor is operating at its limits in terms of torque. As we plan to do long term measurements, skipped steps can accumulate and the actual position of the magnetic trap may vary. Therefore, a so-called home switch electrode was built. Fig. 4.1.3 shows the cryogenic motor. An electrode (1) is placed on a spacer made out of PEEK (2) in order to electrically insulate the electrode from the copper body (3). On the other side, the spindle nut on the magnet holder piece (4) is electrically grounded to the copper body via the ball screw and the cryogenic motor. By moving the magnet holder towards the homing electrode, the homing electrode is electrically grounded. A voltage of 5 V is applied to the electrode (1). If a contact between the

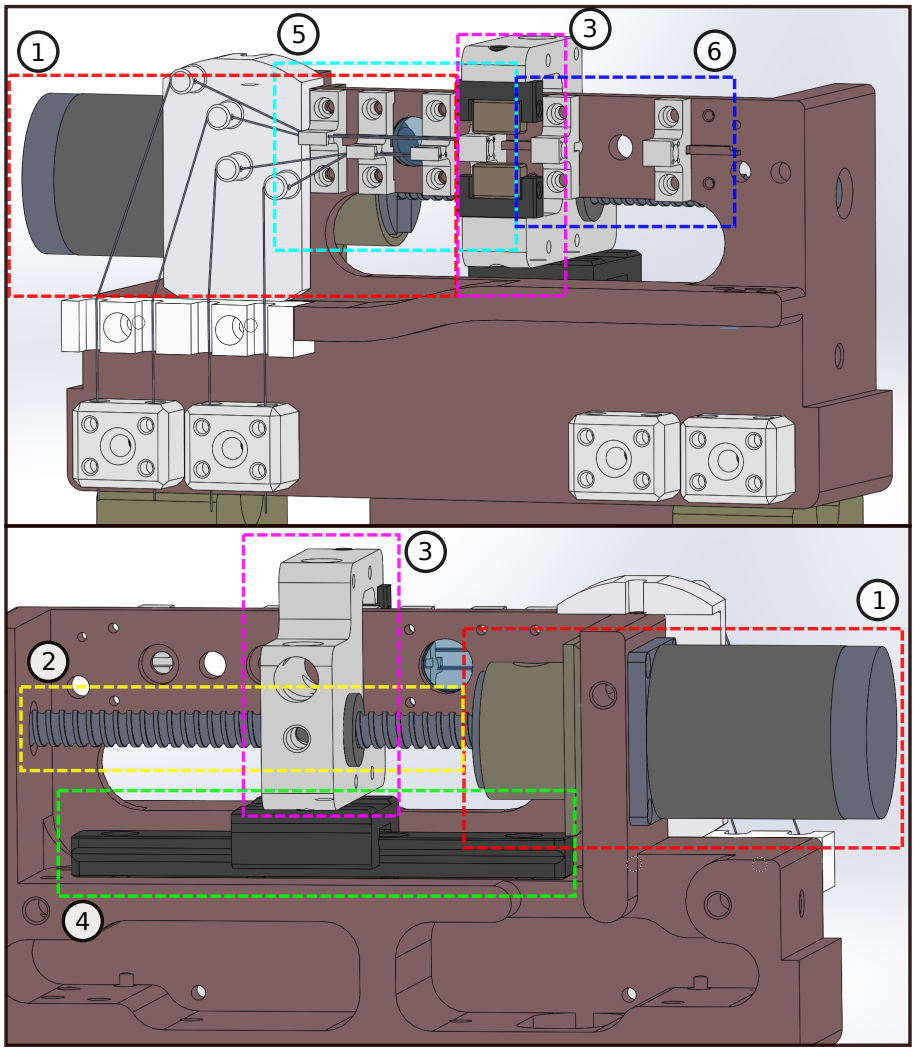

Fig. 4.1.1: **Transport Mechanism of Magnetic Trap.** A cryogenic motor (1) rotates a ball screw made of stainless steel (2). The magnet holder (3) contains a spindle nut and is placed on a sled on a rail guide (4). The cryogenic motor rotates the ball screw which moves the magnet holder on the rail guide allowing a translation of the magnetic trap from the stopping wires for the neutral molecules (5) to the ion trap (6) and back.

electrode (1) and the spindle nut (4) is established, the voltage is pulled down to the level of the copper body (ground). For reading out, we use the digital input on an I/O controller (Unidaq, PIO-DA8) controlled with a self made Python wrapper around the Unidaq DLL, using ctypes. The channel is set to high (5 V), which is pulled down to low 0 V in the homing position.

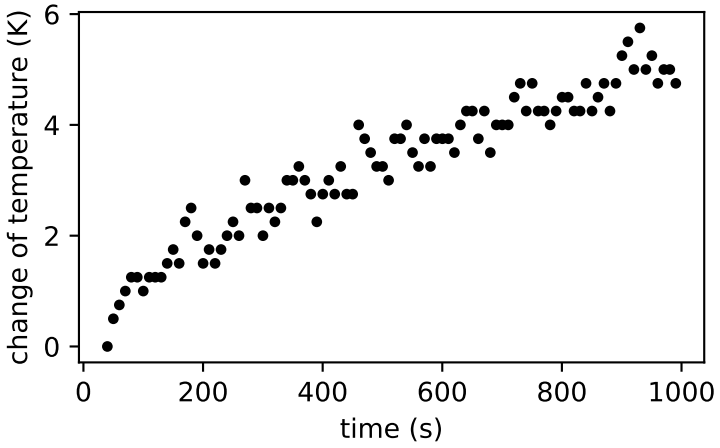

Fig. 4.1.2: **Temperature Development of the Motor.** The temperature of the motor during 100 runs at a repetition rate of 0.1 Hz from the magnetic trap position to the ion trap and back is shown. The experiment was done under at 295 K and 1 atm pressure.

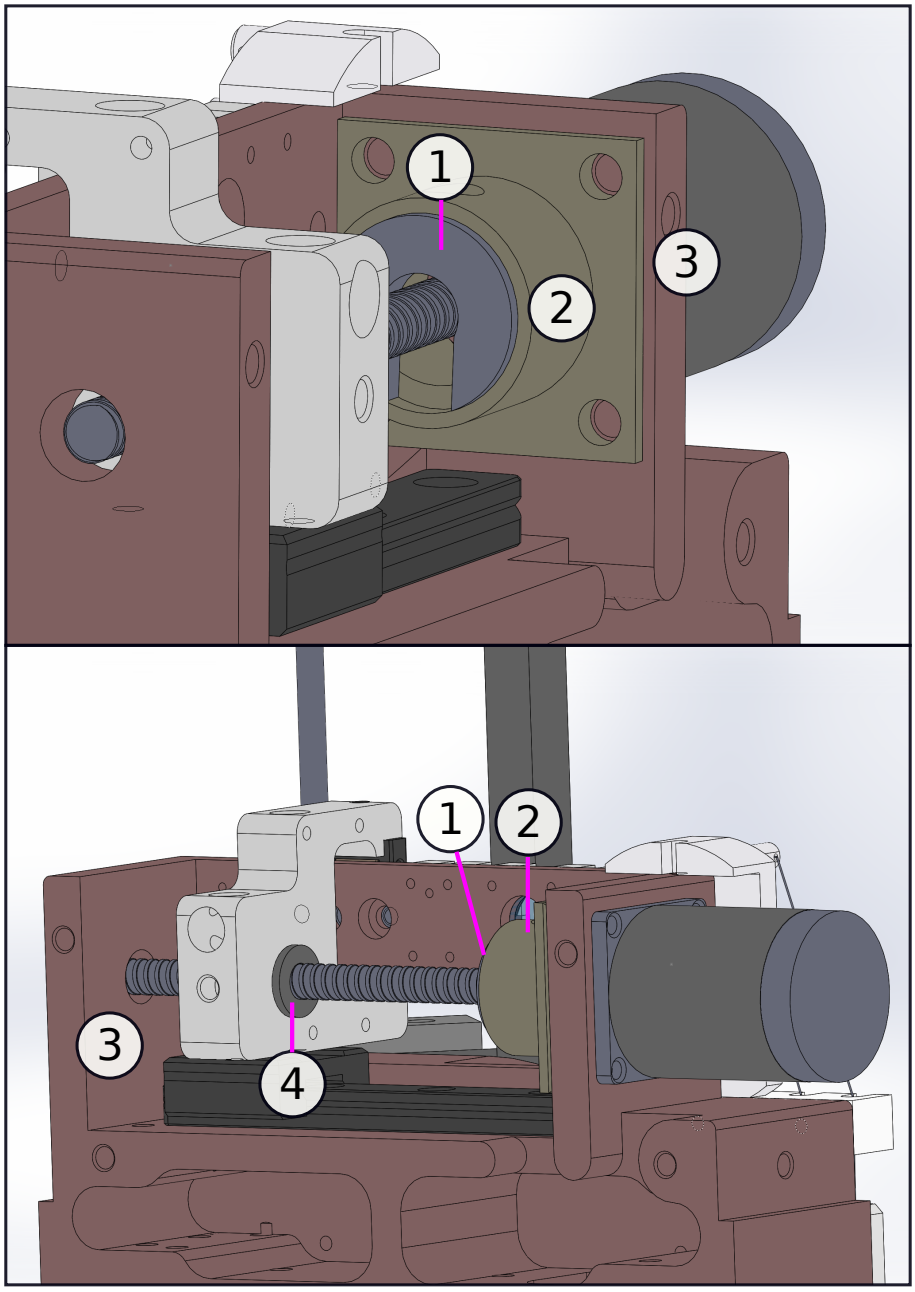

Fig. 4.1.3: **Homing Mechanism.** An electrode (1) is placed on a spacer (2) in order to electrically insulate the electrode from the copper body (3). The spindle nut on the magnet holder piece (4) is electrically grounded to the copper body via the ball screw and the cryogenic motor. A voltage of 5 V is applied to the electrode (1).

4.2 Doppler Cooling in Magnetic Field Gradients

The mechanism of Doppler cooling was discussed in sec. 3.4. An ion is cooled by the change of its momentum upon absorption of photons from a laser field. In order to achieve low temperatures, the frequency of the laser field is detuned in order to compensate for the Doppler shift of an ion flying towards the source of the photons. In the superimposed hybrid trap, however, the ion experiences a large Zeeman energy shift, due to the strong magnetic fields present (up to 1.4 T). This may decrease the cooling efficiency as the laser frequency will not be on resonance with a cooling transition.

Laser cooling in a strong magnetic field is not a new problem. A Penning trap combines strong homogeneous magnetic field to achieve axial confinement of particles with quadrupolar electric fields for axial confinement [177]. In such traps, Ca^+ ions have successfully been Doppler cooled and trapped [178]. While first experiments with Ca^+ were limited to translational temperatures of around 1 K [178], further improvements such as resolved-sideband cooling [179] allowed to reach temperatures of several species of trapped ions close to the Doppler limit [180, 181].

The magnetic trap developed and used in this thesis, however, provides very strong magnetic field gradients of up to 0.4 T/mm, in order to confine neutral molecules. This is in contrast to the homogeneous magnetic fields applied in Penning traps and changes the picture of laser cooling.

This section explores the problem of Doppler laser cooling of Ca^+ in strong magnetic fields to determine limitations by the means of trajectory simulations.

4.2.1 8-Level Optical Bloch Equation

In sec. 3.4.3 the scattering force was derived by solving the optical Bloch equations for a two-level system: the electronic ground state $4s^2S_{1/2}$ and the excited state $4p^2P_{1/2}$ with a transition wavelength of 397 nm. The presence of a magnetic field, however, changes the picture due to Zeeman energy shifts in the m_J levels. Fig. 4.2.1 illustrates the resulting 8-level system: The ground state and the excited state are each split into two states due to the Zeeman effect. Additionally, an excited electron can decay to the $3d^2D_{3/2}$ state, which itself is split into four energy levels. The blue arrow represents the transition at 397 nm (blue laser, subscript b) in absence of a magnetic field and the red arrow the transition at 866 nm respectively (red laser, subscript r). We will now set up the optical Bloch equations of the 8-level system in interaction with the laser field following the derivations of [38] and [39].

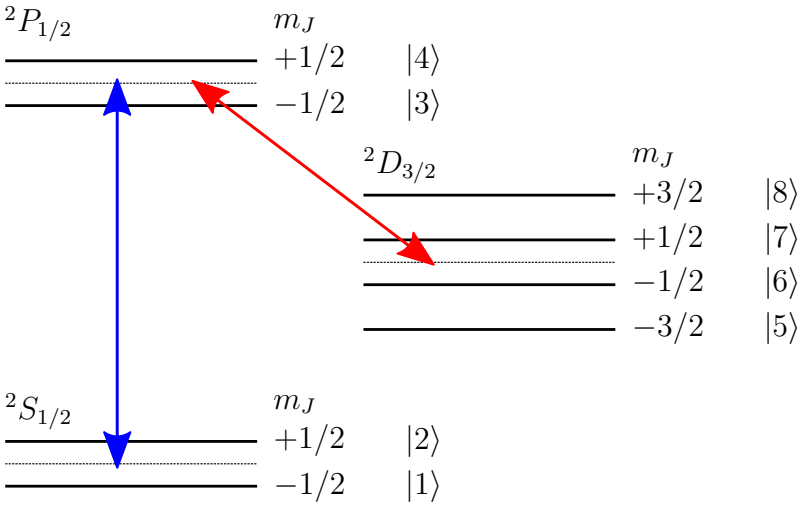

Fig. 4.2.1: **8-Level System in Ca^+.** Due to the Zeeman effect the electronic ground state $4s^2S_{1/2}$ is split into two m_J sublevels $|1\rangle$ and $|2\rangle$ as well as the excited state $4p^2P_{1/2}$ into $|3\rangle$ and $|4\rangle$. The $3d^2D_{3/2}$ state gives rise to the four sublevels $|5\rangle$ through $|8\rangle$. The $4s^2S_{1/2}$ state and the $4p^2P_{1/2}$ are coupled via a laser field with a wavelength of 397 nm and the $3d^2D_{3/2}$ state is coupled to the $4p^2P_{1/2}$ state with a laser field with a wavelength of 866 nm.

The energy levels are split by the Zeeman effect in the magnetic field $\mathbf{B}$ given by

$$\Delta\omega = m_J g_J \frac{\mu_B |\mathbf{B}|}{\hbar} = m_J g_J u \ , \tag{4.2.1}$$

where $u = \frac{\mu_B |\mathbf{B}|}{\hbar}$ and g_J is the Landé factor calculated as

$$g_J = \frac{J(J+1) + S(S+1) - L(L+1)}{2J(J+1)} \ . \tag{4.2.2}$$

The g_J factors in this case are $g_J(^2S_{1/2}) = 2$, $g_J(^2P_{1/2}) = \frac{2}{3}$ and $g_J(^2D_{3/2}) = \frac{4}{5}$. For diople-allowed transitions in the rotating wave approximation the total Hamiltonian can be written as [38, 39]

$$\mathbf{H}_{\text{int}}/\hbar = \tag{4.2.3}$$
$$\begin{pmatrix}
\Delta_{\text{b}} - u & 0 & \frac{\cos\alpha}{\sqrt{3}}\Omega_1 & -\frac{\sin\alpha}{\sqrt{3}}\Omega_{\text{b}} & 0 & 0 & 0 & 0 \\
0 & \Delta_{\text{b}} + u & -\frac{\sin\alpha}{\sqrt{3}}\Omega_{\text{b}} & -\frac{\cos\alpha}{\sqrt{3}}\Omega_{\text{b}} & 0 & 0 & 0 & 0 \\
\frac{\cos\alpha}{\sqrt{3}}\Omega_{\text{b}} & -\frac{\sin\alpha}{\sqrt{3}}\Omega_{\text{b}} & -\frac{1}{3}u & 0 & -\frac{\sin\beta}{2}\Omega_{\text{r}} & -\frac{\cos\beta}{\sqrt{3}}\Omega_{\text{r}} & \frac{\sin\beta}{2\sqrt{3}}\Omega_{\text{r}} & 0 \\
-\frac{\sin\alpha}{\sqrt{3}}\Omega_{\text{b}} & -\frac{\cos\alpha}{\sqrt{3}}\Omega_{\text{b}} & 0 & +\frac{1}{3}u & 0 & -\frac{\sin\beta}{2\sqrt{3}}\Omega_{\text{r}} & -\frac{\cos\beta}{\sqrt{3}}\Omega_{\text{r}} & \frac{\sin\beta}{2}\Omega_{\text{r}} \\
0 & 0 & -\frac{\sin\beta}{2}\Omega_{\text{r}} & 0 & \Delta_{\text{r}} - \frac{6}{5}u & 0 & 0 & 0 \\
0 & 0 & -\frac{\cos\beta}{\sqrt{3}}\Omega_{\text{r}} & -\frac{\sin\beta}{2\sqrt{3}}\Omega_{\text{r}} & 0 & \Delta_{\text{r}} - \frac{2}{5}u & 0 & 0 \\
0 & 0 & \frac{\sin\beta}{2\sqrt{3}}\Omega_{\text{r}} & -\frac{\cos\beta}{\sqrt{3}}\Omega_{\text{r}} & 0 & 0 & \Delta_{\text{r}} + \frac{2}{5}u & 0 \\
0 & 0 & 0 & \frac{\sin\beta}{2}\Omega_{\text{r}} & 0 & 0 & 0 & \Delta_{\text{r}} + \frac{6}{5}u
\end{pmatrix},$$

where Δ_i are the laser detunings from resonance for the blue laser and the red laser (subscripts b, r), Ω_i are the Rabi frequencies and α, β are the angles between the laser polarization vectors and the magnetic field vector.

Similarly to the optical Bloch equation for a two-level system, the goal is to find the time evolution of the density matrix ρ. In general, this evolution is described by the Liouville equation

$$\dot{\rho} = -\frac{i}{\hbar}\left[\hat{H}, \rho\right] + \hat{L}(\rho), \tag{4.2.4}$$

where $\hat{L}(\rho)$ is the Linblad operator [38, 39, 182], given by

$$\hat{L}(\rho) = -\frac{1}{2}\sum_k \hat{C}_k^\dagger \hat{C}_k \rho + \rho \hat{C}_k^\dagger \hat{C}_k - 2\hat{C}_m \rho \hat{C}_m^\dagger. \tag{4.2.5}$$

The operator $\hat{L}(\rho)$ can be regarded as a relaxation superoperator acting on the density matrix ρ accounting for the decoherences[182]. To describe the decoherences, the operators are given as

$$\begin{aligned}
\hat{C}_1 &= \sqrt{\frac{2}{3}\Gamma_{\text{PS}}}\,|1\rangle\langle 4|\,, \\
\hat{C}_2 &= \sqrt{\frac{2}{3}\Gamma_{\text{PS}}}\,|2\rangle\langle 3|\,, \\
\hat{C}_3 &= \sqrt{\frac{1}{3}\Gamma_{\text{PS}}}\,(|1\rangle\langle 3| - |2\rangle\langle 4|)\,, \\
\hat{C}_4 &= \sqrt{\frac{1}{2}\Gamma_{\text{PD}}}\,|5\rangle\langle 3| + \sqrt{\frac{1}{6}\Gamma_{\text{PD}}}\,|6\rangle\langle 4|\,, \\
\hat{C}_5 &= \sqrt{\frac{1}{6}\Gamma_{\text{PD}}}\,|7\rangle\langle 3| + \sqrt{\frac{1}{2}\Gamma_{\text{PD}}}\,|8\rangle\langle 4|\,,
\end{aligned}$$

$$\hat{C}_6 = \sqrt{\frac{1}{3}\Gamma_{\mathrm{PD}}}\left(|6\rangle\langle 3| - |7\rangle\langle 4|\right),$$
$$\hat{C}_7 = \sqrt{2\Gamma_{\mathrm{b}}}\left(|1\rangle\langle 1| + |2\rangle\langle 2|\right) \ ,$$
$$\hat{C}_8 = \sqrt{2\Gamma_{\mathrm{r}}}\left(|5\rangle\langle 5| + |6\rangle\langle 6| + |7\rangle\langle 7| + |8\rangle\langle 8|\right) \ .$$

The coherences $\hat{C}_1$ through $\hat{C}_6$ describe the spontaneous emission from the P to the S and D states with the rates Γ_{PS} and Γ_{PD}. $\hat{C}_7$ and $\hat{C}_8$ describe the coherences due to the bandwidth of the blue and the red lasers $\Gamma_{\mathrm{b/r}}$.
Finally the optical Bloch equations are formed as

$$\dot{\boldsymbol{\rho}}_{\mathrm{c}} = \mathbf{M}\boldsymbol{\rho}_{\mathrm{c}} \ , \tag{4.2.6}$$

where $\mathbf{M}$ is the $N^2 \times N^2$ Liouvillian matrix, formed using Kronecker products of the Hamiltonian and the Linblad operator matrix

$$\mathbf{M} = -\frac{i}{\hbar}\left(\tilde{\mathbf{H}} \otimes \mathbf{I} - \mathbf{I} \otimes \tilde{\mathbf{H}}^{\dagger}\right) + \sum_k \mathbf{C}_k \otimes \mathbf{C}_k. \tag{4.2.7}$$

The matrix $\mathbf{I}$ is the $N \times N$ identity matrix and $\tilde{\mathbf{H}}$ is the non Hermitian effective Hamiltonian

$$\tilde{\mathbf{H}} = \mathbf{H} - \frac{i\hbar}{2}\sum_k \mathbf{C}_k^{\dagger}\mathbf{C}_k. \tag{4.2.8}$$

$\boldsymbol{\rho}_{\mathrm{C}}$ is a column vector consisting of the N^2 elements of the density matrix:

$$\boldsymbol{\rho} = \left(\rho_{11}, \rho_{12}, \rho_{13}, \ldots, \rho_{86}, \rho_{87}, \rho_{88}\right)^T .$$

The photon absorption rate of a ground state ion is proportional to the steady state population of the $^2P_{1/2}$ state. These can be found by solving

$$\dot{\boldsymbol{\rho}}_{\mathrm{c}} = 0 \ , \tag{4.2.9}$$

and by replacing one of the linear equations with the normalization condition

$$\sum_i \rho_{ii} = 1 \ . \tag{4.2.10}$$

4.2.2 Laser Intensities

The laser intensities in this formalism are included in the Rabi frequencies calculated as [38]

$$\Omega_{\mathrm{b/r}} = S_{\mathrm{b/r}}\Gamma_{\mathrm{b/r}} \tag{4.2.11}$$

with the saturation parameter $S_{\mathrm{b/r}}$ related to the laser intensity by

$$I\left[\frac{\mathrm{mW}}{\mathrm{cm}^2}\right] = 1.0456 \times 10^9 \frac{\Gamma_{\mathrm{b/r}}[\mathrm{MHz}]}{\lambda^3_{\mathrm{b/r}}[\mathrm{nm}^3]} S^2_{\mathrm{b/r}}, \tag{4.2.12}$$

with the transition wavelength $\lambda_{\mathrm{b/r}}$. In the context of this thesis we use the parameters from [165]:

$$2\pi \times \Gamma_{\mathrm{b/r}} = 136 \text{ MHz}, 9.45 \text{ MHz}$$
$$\lambda_{\mathrm{b/r}} = 396.96 \text{ nm}, 866.45 \text{ nm}.$$

leading to the relation between the saturation parameters and the laser intensities as:

$$I_{\mathrm{b}} = 362 \times S^2_{\mathrm{b}} \left[\frac{\mathrm{mW}}{\mathrm{cm}^2}\right] \tag{4.2.13}$$

$$I_{\mathrm{r}} = 2.41 \times S^2_{\mathrm{r}} \left[\frac{\mathrm{mW}}{\mathrm{cm}^2}\right] \tag{4.2.14}$$

4.2.3 Solutions of the 8-Level OBE

The optical Bloch equations describe the dynamics of the density matrix in interaction with a laser field. By integrating eq.(4.2.6), we can describe the populations on short timescales. In this example, the peak laser intensity of Gaussian laser beams I_0 with a 1/e width $w_{\mathrm{b/r}}$ of 200 μm and a power p_0 of 0.2 mW which corresponds to 318 mW/cm^2 resulting in saturation parameters of $S_{\mathrm{b}} = 0.938$ and $S_{\mathrm{r}} = 11.5$ using eqns.(4.2.13 & 4.2.14). The peak intensity of a Gaussian laser beam is connected to the power via [183]

$$I_0 = \frac{2p_0}{\pi w^2} \ . \tag{4.2.15}$$

Both detunings $\Delta_{\mathrm{b/r}}$ are set to -10 MHz, the linewidths of the lasers $\Gamma_{\mathrm{b/r}}$ are 0.3 MHz and a magnetic field of 0.5 G is applied. Fig. 4.2.2 shows the time evolution of the 8-level system in the first microsecond, starting form state $|1\rangle$. The populations oscillate with a steady drift towards the steady state solutions.

Fig. 4.2.3 shows the a spectrum of the $^2P_{1/2}$ population, which is proportional to the scattering rate of photons from the cooling laser. The detunings of both lasers $\Delta_{b/r}$ are scanned in a grid. The spectrum decreases in intensity where the detunings of both lasers match, known as dark resonance [184]. In this case, the populations do not drop to zero due to the finite linewidths of the lasers.

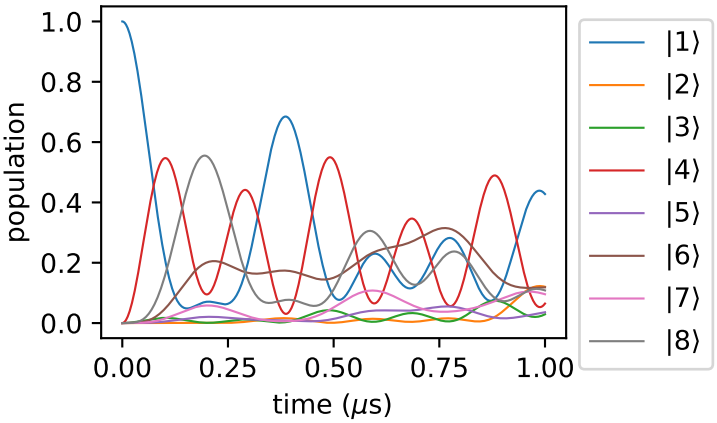

Fig. 4.2.2: **Time Evolution of the 8-Level System.** The system starts from $|1\rangle$ and the populations oscillate with a steady drift towards the steady state solutions.

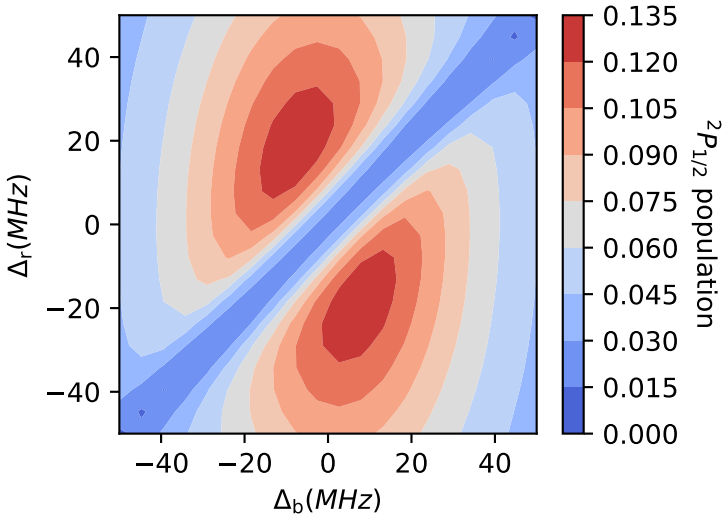

Fig. 4.2.3: **Spectrum of the $^2P_{1/2}$ Population.** The $^2P_{1/2}$ population for various detunings of both lasers $\Delta_{b/r}$ are shown. The spectrum decreases in intensity when both detunings match, known as dark resonance.

4.2.4 Photon Scattering Rates of Ca^+ in the Hybrid Trap

A first analysis of laser cooling of Ca^+ ions at rest in the presence of the magnetic fields in the hybrid trap was carried out with a stationary example. The detunings $\Delta_{b/r}$ were set to zero and both laser bandwiths were 0.3 MHz. The laser powers of both lasers were 0.2 mW with a focus spot size of 200 μm and a Gaussian intensity distribution. The laser propagates along the Z axis in positive direction with a linear polarization $\boldsymbol{\epsilon}_b$ in the XY-plane at an angle of $\pi/4$ meaning $\boldsymbol{\epsilon}_b = \frac{1}{\sqrt{2}}(1,1,0)^T$. The angles between the laser polarization $\boldsymbol{\epsilon}_{b/r}$ and the magnetic field $\mathbf{B}$ produced by the bar magnets in the magnetic trap (see sec.2.4.1.2), α and β, were calculated for the each point in space as

$$\alpha = \arccos\left(\frac{\mathbf{B}\cdot\boldsymbol{\epsilon}_b}{|\mathbf{B}|\ |\boldsymbol{\epsilon}_b|}\right) , \tag{4.2.16}$$

and analogously for β.

Fig. 4.2.4 shows a map of the populations of the $^2P_{1/2}$ state in Ca^+ in the center of the trap. The population is proportional to the photon scattering rate of the cooling laser [162]. As the gradient of the magnetic field is lowest along the Z axis, these profiles are elongated along this axis. In the center a dark resonance showed up, where the P state was not populated. The profile shows a ring of increasing population of the P-state with maxima at 5 μm along X, 4 μm along Y and 14 μm along Z. The excited state populations drop to below 0.02 at distances to the trap center of 55 μm.

To optimize the efficiency of the laser cooling in the magnetic field, the scattering rates have to be maximized. Therefore, we look at the mean population of the P state in a line along the Z axis (the laser axis) with a length of 1 mm and centered in the trap center. Fig. 4.2.5 shows the mean of steady state solutions along this line for different combinations of detunings $\Delta_{r/b}$. It shows three maxima: one for detunings of zero and, similar to the case of a low homogeneous magnetic field shown in fig. 4.2.3, two bigger maxima for detunings of $(\Delta_b, \Delta_r) = \pm(7.69, -24.1)$ MHz. However, the average P state population and thus the scattering rate is about one order of magnitude lower due to the large Zeeman splittings compared to the case of a weak homogeneous magnetic field.

To further analyze the laser cooling of Ca^+ in magnetic fields with large gradients, a trajectory simulation can be carried out and is discussed in the next section.

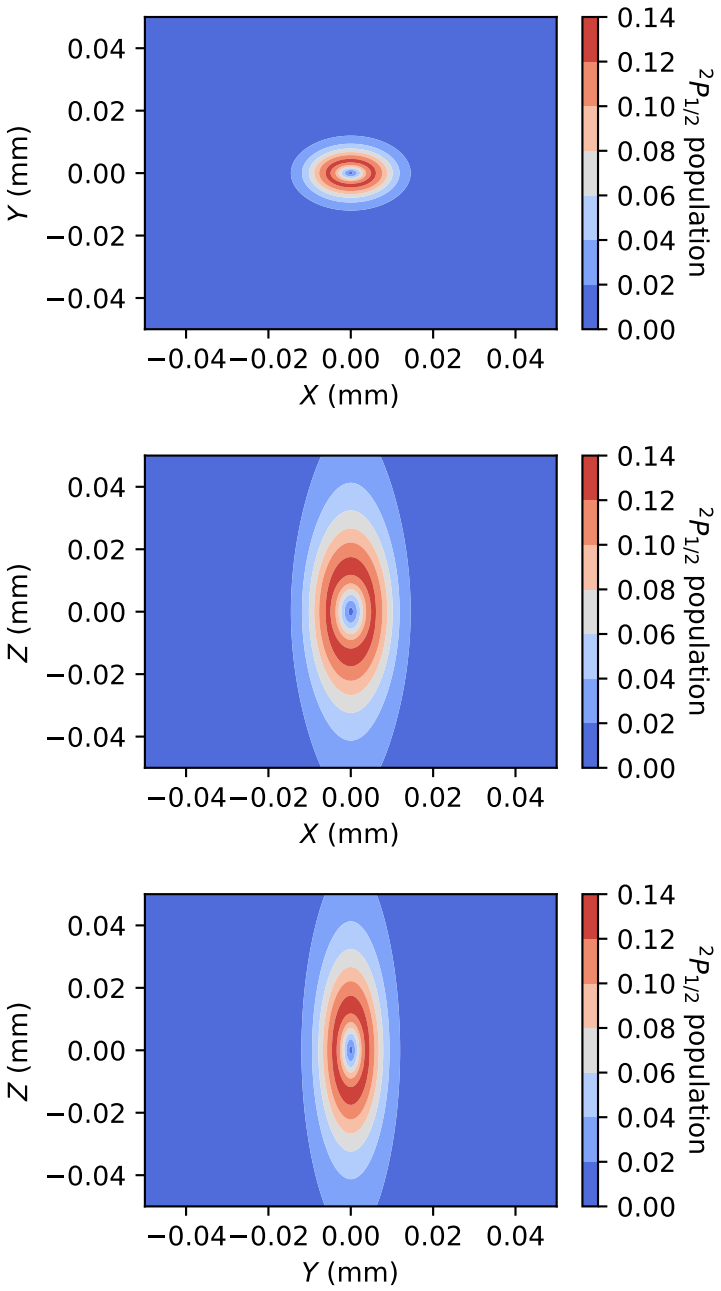

Fig. 4.2.4: **Map of the $^2P_{1/2}$ Population in the Magnetic Field.** The steady-state populations of the excited states are shown using the position dependent Zeeman shifts in the magnetic trap.

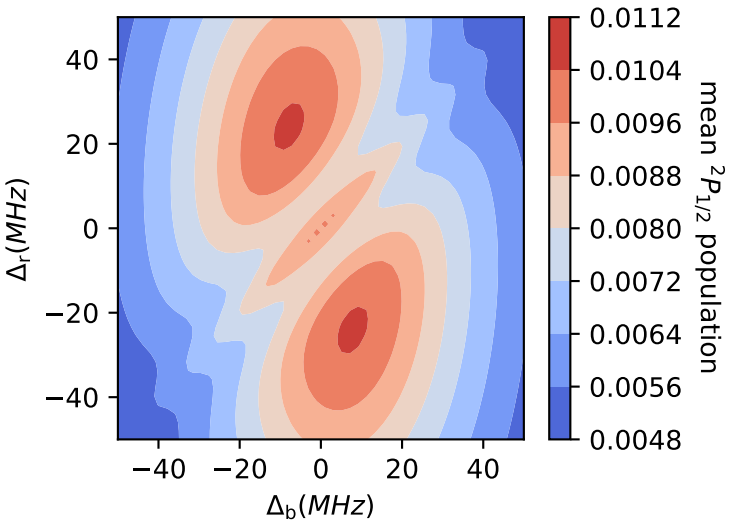

Fig. 4.2.5: **Average $^2P_{1/2}$ Population in the Magnetic Field.** The steady-state population of the excited state, averaged over a line along the Z-axis are shown for several detunings $\Delta_{r/b}$ of the laser frequencies.

4.2.5 Trajectory Calculation

A well established method for simulating laser cooling via the scattering force is to calculate the absorption and emission probability P_{ij} via the scattering rate as $\rho_{ii}\Gamma$, integrated for a time step, and compare this with a uniform random number γ to determine an occurrence of absorption or emission. The momenta of the photons and the particle are then added up [185, 186].

A similar method was implemented for the simulation using the 8-Level OBE formalism. An ion starts in the $^2S_{1/2}$ state, in the lower Zeeman state $|1\rangle$. The excitation probability is calculated for excited states of $|3\rangle$ and $|4\rangle$. If the random number γ for this time step is lower than the probability P_{13} to be excited to the state $|3\rangle$, the ion will end up in this state and a photon from the blue laser is absorbed. In the case of $P_{13} < \gamma \leq P_{14}$ the ion will be excited to state $|4\rangle$. From state $|3\rangle$ resp. $|4\rangle$ a possible outcome when respecting the selection rule of $\Delta m_J = 0, \pm 1$ is $|1\rangle, |2\rangle, |5\rangle, |6\rangle, |7\rangle$ and $|1\rangle, |2\rangle, |6\rangle, |7\rangle, |8\rangle$ respectively. The states are tracked and photons from the blue and the red laser are emitted and absorbed leading to changes in momentum and eventually cooling.

Fig. 4.2.6 shows the development of the temperature of a laser cooled $^{40}Ca^+$ ion for a weak homogeneous magnetic field and the magnetic field produced in the magnetic trap. The temperature is given as the kinetic energy averaged over one RF cycle and is shown for a Ca^+ ion in a homogeneous magnetic field of 1 G amplitude (black line) and a Ca^+ ion in the magnetic field in the magnetic trap (red line). In the case of the homogeneous magnetic field, the angles α and β between the laser polarization and the magnetic field vector were set to $\pi/2$ and the amplitude of the magnetic field was 1 G. The laser detunings $\Delta_{b/r}$ were both set to -10 MHz at a linewidth of 0.3 MHz. The saturation parameters were $S_b = 1$ and $S_r = 6$ corresponding to laser intensities of $I_b = 362$ mWcm^{-2} and $I_b = 86.8$ mWcm^{-2}. The ion trap parameters were set to an RF amplitude V_0 of 150 V, a RF frequency of 8.0 MHz and an endcap voltage U_{end} of 2 V.

The temperature development of the ion, in the case of a weak magnetic field reached half of the maximum value at around 3.5 ms and reached a final temperature of 25 mK at 50 ms. In the case of the magnetic trap, however, half of the maximum value is reached at around 25 ms and the final temperature after 600 ms is around 0.6 K. This difference is a consequence of the strong gradients in the magnetic field provided by the bar magnets. The presented calculations show the temperature development of a Ca^+ ion for one laser detuning. Improved cooling in gradient

fields could possibly achieved by a dynamic detuning of the laser frequencies, taking advantage of the fact that the ion spends most time around the turning points in the ion trap. The warm ion will experience a large Zeeman shift on average, but as the ion loses in kinetic energy and spends most time close to the trap center, the detuning could be lowered. However, this aspect of laser cooling is beyond the scope of the dissertation.

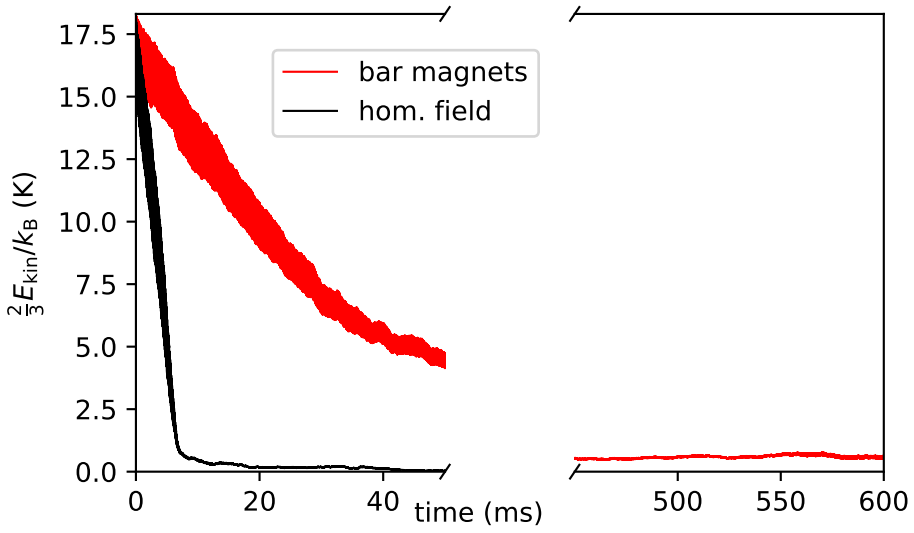

Fig. 4.2.6: **Laser Cooling of $^{40}Ca^+$ in a Magnetic Field.** The kinetic energy averaged over one RF cycle is shown for a Ca^+ ion in a homogeneous magnetic field of 1 G amplitude (black line) and the magnetic field in the magnetic trap (red line).

4.3 Collision Rate: Advantages of a Hybrid Trap

The main advantage of a hybrid trap over Stark decelerated molecular beam, coupled to an ion trap is the potential long interaction time between the two trapped species and therefore the ability to measure slow reactions. A quick comparison of the collision events in a hybrid trap experiment and a Stark decelerated molecular beam, coupled to an ion trap should give more insight into the advantages of the hybrid trap. Assuming a bimolecular reaction rate constant $k = 1 \times 10^{-9}$ cm^{3}s^{-1} for an ion-neutral reaction [27], which is on the order of typical rate constants using the Langevin model [187, 188]. For simplicity, we assume a spherical trapped ion crystal with a radius of 100 μm and a spherical cloud of trapped neutral molecules with a radius of 670 μm. Typical number densities in coulomb ion crystals are on the order of 1×10^9 cm^{-3} when assuming a distance of 10 μm between the ions and the density of Stark decelerated OH beams in our experiment is on the order of 1×10^7 cm^{-3} in the trap center. In an experiment where a Stark decelerated molecular beam with a velocity of 29 m/s is directed into an ion trap, this would lead to a reaction probability of less than 1×10^{-3} per experimental cycle. For this estimation the overlap volume of two spheres, including the expansion of the Stark decelerated beam during the free flight to the trap center was taken as the interaction volume. Our typical experimental repetition rate of the Stark decelerator was on the order of 10 Hz. In total this would result in about 0.86 collisions in 60 s. An experimental cycle could in principle be on the order of 250 Hz as the total deceleration cycle has a duration of around 4 ms. Thus the upper limit would be around 22 collisions in 60 s. For the hybrid trap we assume an exponential decay of the trapped molecular density with a 1/e lifetime of 30 s, which is on the order of the results achieved in this thesis. Furthermore, the initial neutral molecule density is about half the density of the decelerated molecular beam, since magnetic high-field seekers are lost. Integrating the collisions over 60 s under these circumstances leads to about 543 collisions. This results in higher collisions over measurement time of a factor of 25 in the hybrid trap experiment, compared to a Stark decelerated beam coupled to an ion trap.

4.4 Conclusion and Outlook

This chapter described the procedure for how to superimpose the centers of the magnetic trap and the ion trap. A cryogenic motor translates the magnet holder along the shared Z-axis of the traps. A method of finding a reference position of the magnets along the translation axis was designed and tested with success. The operation of the transport, however, still needs to be improved. The main problem lies in the thermal contraction of the materials which lowers the efficiency of the presented design. As the thermal load on the cryogenic stage should be as small as possible a cryogenic motor with a small heat load was chosen. This, however limits the strength of the motor. We found this to be a limit as the magnets stuck under cryogenic conditions. As the repetition rate of future experiments will be on the order of 0.1 Hz or lower, the heating by the cryogenic motor is a negligible problem. We thus decided to use a stronger motor and currently work on improving the transporting mechanism (VSS 25.200.1,2-UHVC1-4Lp, Phytron).
The laser cooling of Ca^+ in a magnetic field was analyzed by using an 8-level model. The efficiency of laser cooling was found to be about one order of magnitude lower in the magnetic trap compared to a weak homogeneous field of 1 G, which could potentially be improved using a dynamic laser detuning. But as this hybrid trap allows the transport of the magnetic trap, the ions can be trapped and laser cooled before a collision experiment. Then the traps can be superimposed which will lower the cooling efficiency. Further research and optimization of the laser cooling will be required.
Additionally to the challenges of laser cooling in the strong magnetic field gradients, the neutral molecules could potentially undergo spin-flips at points in the trap, where the magnetic field $\mathbf{B}$ is orthogonal to the electric field $\mathbf{E}$ from the ion trap [135, 136, 138]. In our hybrid trap setup, these points occur mostly close to the Z-axis. As a result of a spin-flip transition, the molecules end up in non-trappable states and are attracted by the magnets. This problem, however, can be resolved e.g. by applying a homogeneous magnetic offset field [136]. In our case, magnetic fields $\mathbf{B} = B(1, 1, 0)^T$ with $B = 0.1$ T can reduce this problem from the points close to the Z-axis to one point in the trap center.
With working cryogenic magnetic and ion traps, the presented design of hybrid trap to confine neutral molecules and molecular ions paves the way to studying cold chemistry of these species.

Chapter 5

Conclusion and Outlook

A cryogenic molecular ion-neutral molecule hybrid trap was designed and developed. A magnetic trap was built, using two permanent magnets. The trap assembly used four wires and the bar magnets as electrodes to shape a last deceleration potential. The trap was cooled down to 17 K and shielded from ambient room temperature BBR using cryogenic shields. The shielding and the improved vacuum conditions in the cryogenic environment allowed the trapping of OH radicals for about 40 s, which was an improvement of a factor of ≈57 compared to the trapping lifetimes under room temperature conditions. A rate equation model was developed and applied to gain further insight into the limitations of the trapping times. By constructing an effective BBR spectral energy density, taking into account all the apertures in the cryogenic shields, a BBR limited 1/e lifetime of 81 s was estimated. The model indicated that both, improved vacuum conditions and better cryogenic shielding from BBR could potentially improve the lifetimes of trapped OH in the magnetic trap.

Furthermore, a cryogenic ion trap was built and set up from cooling laser setup over a calcium source and the ionization laser setup. The trap consisted of four thin wires and two hollow tubes as endcaps. The thin wires served as RF electrodes, providing radial confinement and the endcaps served as DC electrodes for the axial confinement of ions in the trap and allowing a future transport of trapped OH molecules into the ion trap through the hollow structure. A electrostatic shielding of the ion trap from the high voltages pulsed in the neutral trap assembly was designed and numerically analyzed. The trap geometry was analyzed and compared to the ideal linear Paul trap. Geometric parameters were extracted by comparing the potentials from FEM to the potentials in an ideal Paul trap. The parameters were verified by comparing trajectory simulations of trapped Ca^+ ions with experimental fluorescence images.

The next experiments with the ion trap will include sympathetic cooling of molecules such as N_2^+.

A method for transporting the trapped neutral molecules into the ion trap was developed. The holder of the permanent magnets in the magnetic trap was built to be movable. Using a cryogenic motor, the magnets could be moved towards the ion trap, allowing one to superimpose both trap centers. The mechanism was shown to work but still leaves some room for improvement. A stronger motor and small improvements on the ball screw should suffice to allow for a reliable operation for long-term measurements.

The challenge of laser-cooling in the hybrid trap was analyzed. The biggest obstacle comes from the wide range of Zeeman shifts in the cooling transitions in the trap region, due to the large gradients in the magnetic field. Modeling the laser cooling via 8-level optical Bloch equations showed that laser-cooling is in principle still possible but less efficient. A compensation of the Zeeman shift via dynamic laser detunings was proposed, depending on the temperature of the ion. However, as the magnetic trap can be moved away from the ions, they can in principle be cooled before superimposing both traps and separated after some interaction time, to allow an analysis of the fluorescence image from the trapped Coulomb crystal.

The presented work paves the way to studying cold chemistry of these species. The knowledge and experience gained lead to the design of an optimized hybrid trap, which is already being developed by C. Mangeng. The challenge of working with high-voltage pulses in a small assembly is omitted by replacing the HV stopping part with pulsed electromagnets, similar to the trap in reference [139]. Improvements on the detection of radicals are planned to be achieved by adding additional observables. OH radicals are planned to be ionized via REMPI and detected with a TOF mass spectrometer [140] on a microchannel plate detector (MCP). The mass spectrometer can then not only be used to detect OH but also to detect future reaction products from cold collisions in a hybrid trap.

Chapter 6

Acknowledgment

First of all, I thank Stefan Willitsch for giving me the opportunity to work in his group on such an exciting and ambitious research project. His excellent guidance was one of the most important factors leading to the success of this project.
I want to thank Dongdong Zhang for the supervision of the first three years during my PhD. His inputs during the development of the cryogenic magnetic trap were invaluable.
Furthermore, special thanks goes to both Dongdong Zhang and Dominik Haas for the pleasant atmosphere. Both developed the source of cold OH radicals from valve over decelerator to the detection. Together with both, Dongdong and Dominik, we designed the cryogenic magnetic trap including the mechanism for the displacement of the magnets as well as the first iterations of the ion trap and collected the experimental results for the long-term trapping of OH radicals in a cryogenic magnetic trap.
Thomas Kierspel joined the team for the last two years of my PhD. He brought fresh wind into the project and lead to improving the experimental apparatus. His exemplary way of attacking and solving problems, questioning every decision as well as communication skills brought to the experiment to another level. Thank you for your patience and for the excellent guidance both scientifically and personally.
I want to acknowledge Georg Tanner for the support on the development of the ion trap during his project in our group. His work on simulations pointed out problems in the geometry of the ion trap and has directly influenced the final design.
For the support in the development of the electronics for the ion trap and for many pleasant discussions I want to thank Gregor Hegi.
The most important contribution towards all these experimental results comes form the work shop in the physical chemistry. Thank you Philipp Knöpfel and Grischa

Martin for transforming our wild ideas into CAD drawings and physical objects leading to the hybrid trap setup as it is now. Thank you Georg Holderied for building the electronics in our setup and the support. The lasers would not have worked if it weren't for Anatoly Johnson, thank you.
I also want to thank Christian Mangeng for the pleasant atmosphere in the lab and the office. I wish him all the best and success in improving the hybrid trap system with his new design.
Thank you Ian Rouse for the simulation codes for the ion trap, for showing me that I can't drink a lot. A big thank you to the cold ions research group especially Tomislav, Panos, Uxía, Pascal for the great time.
But I am mostly grateful to my parents Yvonne and Andreas, my brothers Marcello and Moreno, my sisters Sandra, Anina and Celina and my love Sagana for everything.

Bibliography

[1] T. Rosenband, D. B. Hume, P. O. Schmidt, C. W. Chou, A. Brusch, L. Lorini, W. H. Oskay, R. E. Drullinger, T. M. Fortier, J. E. Stalnaker, S. A. Diddams, W. C. Swann, N. R. Newbury, W. M. Itano, D. J. Wineland, and J. C. Bergquist, *Science*, 2008, **319**, 1808–1812.

[2] M. Sinhal, Z. Meir, K. Najafian, G. Hegi, and S. Willitsch, *Science*, 2020, **367**, 1213–1218.

[3] H. L. Bethlem and W. Ubachs, *Faraday Discuss.*, 2009, **142**, 25–36.

[4] K. Mølhave and M. Drewsen, *Phys. Rev. A*, 2000, **62**, 011401.

[5] H. Kimble, *Nature*, 2008, **453**, 1023–1030.

[6] S. Wehner, D. Elkouss, and R. Hanson, *Science*, 2018, **362**.

[7] M. T. Bell, A. D. Gingell, J. M. Oldham, T. P. Softley, and S. Willitsch, *Faraday Discuss.*, 2009, **142**, 73–91.

[8] M. T. Bell and T. P. Softley, *Mol. Phys.*, 2009, **107**, 99–132.

[9] R. V. Krems, *Phys. Chem. Chem. Phys.*, 2008, **10**, 4079–4092.

[10] S. Willitsch, M. T. Bell, A. D. Gingell, S. R. Procter, and T. P. Softley, *Phys. Rev. Lett.*, 2008, **100**, 043203.

[11] B. R. Heazlewood, *Mol. Phys.*, 2019, **117**, 1934–1941.

[12] A. B. Henson, S. Gersten, Y. Shagam, J. Narevicius, and E. Narevicius, *Science*, 2012, **338**, 234–238.

[13] S. Chefdeville, Y. Kalugina, S. Y. T. van de Meerakker, m. Naulin, F. Lique, and M. Costes, *Science*, 2013, **341**, 1094–1096.

[14] D. Bhattacharya, M. Pawlak, A. Ben-Asher, A. Landau, I. Haritan, E. Narevicius, and N. Moiseyev, *J. Chem. Phys. Lett.*, 2019, **10**, 855–863.

[15] A. Klein, Y. Shagam, W. Skomorowski, P. S. Żuchowski, M. Pawlak, L. M. C. Janssen, N. Moiseyev, S. Y. T. van de Meerakker, A. van der Avoird, C. P. Koch, and E. Narevicius, *Natu. Phys.*, 2017, **13**, 35–38.

[16] J. Toscano, H. J. Lewandowski, and B. R. Heazlewood, *Phys. Chem. Chem. Phys.*, 2020, **22**, 9180–9194.

[17] S. Y. T. van de Meerakker, H. L. Bethlem, N. Vanhaecke, and G. Meijer, *Chem. Rev.*, 2012, **112**, 4828–4878.

[18] D. Haas, S. Scherb, D. Zhang, and S. Willitsch, *EPJ Tech. Instr.*, 2017, **4**, 6.

[19] J. Toscano, L. Y. Wu, M. Hejduk, and B. R. Heazlewood, *J. Phys. Chem. A*, 2019, **123**, 5388–5394.

[20] S. D. Hogan, M. Motsch, and F. Merkt, *Phys. Chem. Chem. Phys.*, 2011, **13**, 18705–18723.

[21] S. A. Rangwala, T. Junglen, T. Rieger, P. W. H. Pinkse, and G. Rempe, *Phys. Rev. A*, 2003, **67**, 043406.

[22] D. McCarron, *J. Phys. B*, 2018, **51**, 212001.

[23] L. Anderegg, B. L. Augenbraun, Y. Bao, S. Burchesky, L. Cheuk, and J. M. Ketterle, W. amd Doyle, *Nat. Phys.*, 2018, **14**, 890–893.

[24] D. Chakraborty, J. Hazra, and B. Deb, *J. Phys. B*, 2011, **44**, 095201.

[25] C. Chin, R. Grimm, P. Julienne, and E. Tiesinga, *Rev. Mod. Phys.*, 2010, **82**, 1225–1286.

[26] A. Kilaj, H. Gao, D. Rösch, U. Rivero, J. Küpper, and S. Willitsch, *Nat. Commun.*, 2018, **9**, 2096.

[27] L. S. Petralia, A. Tsikritea, J. Loreau, T. P. Softley, and B. R. Heazlewood, *Nat. Commun.*, 2020, **11**, 173.

[28] B. Yan, P. F. H. Claus, B. G. M. von Oorschot, L. Gerritsen, A. T. J. B. Eppnik, S. Y. T. van de Meerakker, and D. H. Parker, *Rev. Sci. Instr.*, 2013, **84**, 023102.

[29] L. Ploenes, D. Haas, D. Zhang, S. Y. T. van de Meerakker, and S. Willitsch, *Rev. Sci. Instr.*, 2016, **87**, 053305.

[30] B. K. Stuhl, M. Yeo, M. T. Hummon, and J. Ye, *Mol. Phys.*, 2013, **111**, 1798–1804.

[31] Y. Fang, F. Liu, V. P. Barber, S. J. Klippenstein, A. B. McCoy, and M. I. Lester, *J. Chem. Phys.*, 2016, **144**, 061102.

[32] K. Acharyya, E. Herbst, R. Caravan, R. Shannon, M. Blitz, and D. Heard, *Mol. Phys.*, 2015, **113**, 2243–2254.

[33] R. J. Shannon, M. A. Blitz, A. Goddard, and D. E. Heard, *Nat. Chem.*, 2013, **5**, 745–749.

[34] B. J. Robinson and R. X. McGee, *Ann. Rev. Astronomy and Astrophysics*, 1967, **5**, 183–212.

[35] S. Hoekstra, J. J. Gilijamse, B. Sartakov, N. Vanhaecke, L. Scharfenberg, S. Y. T. van de Meerakker, and G. Meijer, *Phys. Rev. Lett.*, 2007, **98**, 133001.

[36] S. Gulde, D. Rotter, S. Barton, F. Schmit-Kaler, R. Blatt, and W. Hogervorst, *Appl. Phys. B*, 2001, **73**, 861–863.

[37] D. M. Lucas, A. Ramso, J. P. Home, M. J. McDonnell, S. Nakayama, J.-P. Stacey, S. C. Webster, D. N. Stacey, and A. M. Steane, *Phys. Rev. A*, 2004, **69**, 1–13.

[38] H. Oberst, Resonance fluorescence of single barium ions, 1999.

[39] A. D. Gingell, M. T. Bell, J. M. Oldham, T. P. Softley, and J. N. Harvey, *J. Chem. Phys. Lett.*, 2010, **133**, 194302.

[40] F. H. J. Hall, M. Aymar, M. Raoult, O. Dulieu, and S. Willitsch, *Mol. Phys.*, 2013, **111**, 1684–1690.

[41] F. H. J. Hall, P. Eberle, G. Hegi, M. Raoult, M. Aymar, O. Dulieu, and S. Willitsch, *Mol. Phys.*, 2013, **111**, 2020–2030.

[42] L. D. Carr, D. DeMille, R. V. Krems, and J. Ye, *New J. Phys.*, 2009, **11**, 055049.

[43] S. Willitsch, *Int. Rev. Phys. Chem.*, 2012, **31**, 175–199.

[44] M. Lemeshko, R. V. Krems, J. M. Doyle, and S. Kais, *Mol. Phys.*, 2013, **111**, 1648–1682.

[45] S. A. Moses, J. P. Covey, M. T. Miecnikowski, D. S. Jin, and J. Ye, *Nat. Phys.*, 2017, **13**, 13–20.

[46] S. Willitsch, *Adv. Chem. Phys.*, 2017, **162**, 307–340.

[47] E. R. Hudson, H. J. Lewandowski, B. C. Sawyer, and J. Ye, *Phys. Rev. Lett.*, 2006, **96**, 143004.

[48] H. L. Bethlem, M. Kajita, B. Sartakov, G. Meijer, and W. Ubachs, *Eur. Phys. J-Spec. Top.*, 2008, **163**, 55–69.

[49] S. Truppe, R. Hendricks, S. Tokunaga, H. Lewandowski, M. Kozlov, C. Henkel, E. Hinds, and M. Tarbutt, *Nat. Commun.*, 2013, **4**, 2600.

[50] J. Baron, W. C. Campbell, D. DeMille, J. M. Doyle, G. Gabrielse, Y. V. Gurevich, P. W. Hess, N. R. Hutzler, E. Kirilov, I. Kozyryev, B. R. O'Leary, C. D. Panda, M. F. Parsons, E. S. Petrik, B. Spaun, A. C. Vutha, and A. D. West, *Science*, 2014, **343**, 269–272.

[51] S. Borri and G. Santambrogio, *Adv. Phys.: X*, 2016, **1**, 368–386.

[52] I. Kozyryev, L. Baum, K. Matsuda, B. L. Augenbraun, L. Anderegg, A. P. Sedlack, and J. M. Doyle, *Phys. Rev. Lett.*, 2017, **118**, 173201.

[53] J. Lim, J. R. Almond, M. A. Trigatzis, J. A. Devlin, N. J. Fitch, B. E. Sauer, M. R. Tarbutt, and E. A. Hinds, *Phys. Rev. Lett.*, 2018, **120**, 123201.

[54] S. Ospelkaus, K.-K. Ni, D. Wang, M. H. G. de Miranda, B. Neyenhuis, G. Quéméner, P. S. Julienne, J. L. Bohn, D. S. Jin, and J. Ye, *Science*, 2010, **327**, 853–857.

[55] F. Hall and S. Willitsch, *Phys. Rev. Lett.*, 2012, **109**, 233202.

[56] B. Yan, S. A. Moses, B. Gadway, J. P. Covey, K. R. A. Hazzard, A. M. Rey, D. S. Jin, and J. Ye, *Nature*, 2013, **501**, 521–525.

[57] S. N. Vogels, J. Onvlee, S. Chefdeville, A. van der Avoird, G. C. Groenenboom, and S. Y. T. van de Meerakker, *Science*, 2015, **350**, 787–790.

[58] X. Wu, T. Gantner, M. Koller, M. Zeppenfeld, S. Chervenkov, and G. Rempe, *Science*, 2017, **358**, 645–648.

[59] S. N. Vogels, T. Karman, J. Kłos, M. Besemer, J. Onvlee, A. van der Avoird, G. C. Groenenboom, and S. Y. T. van de Meerakker, *Nat. Chem.*, 2018, **10**, 435–440.

[60] L. P. Parazzoli, N. J. Fitch, P. S. Żuchowski, J. M. Hutson, and H. J. Lewandowski, *Phys. Rev. Lett.*, 2011, **106**, 193201.

[61] A. Micheli, G. K. Brennen, and P. Zoller, *Nat. Phys.*, 2006, **2**, 341–347.

[62] J. A. Blackmore, L. Caldwell, P. D. Gregory, E. M. Bridge, R. Sawant, J. Aldegunde, J. Mur-Petit, D. Jaksch, J. M. Hutson, B. E. Sauer, M. R. Tarbutt, and S. L. Cornish, *Quant. Sci. Tech.*, 2018, **4**, 014010.

[63] D. DeMille, *Phys. Rev. Lett.*, 2002, **88**, 067901.

[64] S. F. Yelin, K. Kirby, and R. Côté, *Phys. Rev. A*, 2006, **74**, 050301.

[65] S. Y. T. van de Meerakker, P. H. M. Smeets, N. Vanhaecke, R. T. Jongma, and G. Meijer, *Phys. Rev. Lett.*, 2005, **94**, 023004.

[66] M. Quintero-Pérez, P. Jansen, T. E. Wall, J. E. van den Berg, S. Hoekstra, and H. L. Bethlem, *Phys. Rev. Lett.*, 2013, **110**, 133003.

[67] B. G. U. Englert, M. Mielenz, C. Sommer, J. Bayerl, M. Motsch, P. W. H. Pinkse, G. Rempe, and M. Zeppenfeld, *Phys. Rev. Lett.*, 2011, **107**, 263003.

[68] C. Seiler, S. D. Hogan, and F. Merkt, *Phys. Chem. Chem. Phys.*, 2011, **13**, 19000–19012.

[69] M. Zeppenfeld, B. G. U. Englert, R. Glöckner, A. Prehn, M. Mielenz, C. Sommer, L. D. van Buuren, M. Motsch, and G. Rempe, *Nature*, 2012, **491**, 570–573.

[70] A. Prehn, M. Ibrügger, R. Glöckner, G. Rempe, and M. Zeppenfeld, *Phys. Rev. Lett.*, 2016, **116**, 063005.

[71] H.-I. Lu, I. Kozyryev, B. Hemmerling, J. Piskorski, and J. M. Doyle, *Phys. Rev. Lett.*, 2014, **112**, 113006.

[72] J. D. Weinstein, R. de Carvalho, T. Guillet, B. Friedrich, and J. M. Doyle, *Nature*, 1998, **395**, 148–150.

[73] J. S. Eardley, N. Warner, L. Z. Deng, D. Carty, and E. Wrede, *Phys. Chem. Chem. Phys.*, 2017, **19**, 8423–8427.

[74] Y. Liu, S. Zhou, W. Zhong, P. Djuricanin, and T. Momose, *Phys. Rev. A*, 2015, **91**, 021403.

[75] B. C. Sawyer, B. L. Lev, E. R. Hudson, B. K. Stuhl, M. Lara, J. L. Bohn, and J. Ye, *Phys. Rev. Lett.*, 2007, **98**, 253002.

[76] Y. Liu, M. Vashishta, P. Djuricanin, S. Zhou, W. Zhong, T. Mittertreiner, D. Carty, and T. Momose, *Phys. Rev. Lett.*, 2017, **118**, 093201.

[77] N. Akerman, M. Karpov, Y. Segev, N. Bibelnik, J. Narevicius, and E. Narevicius, *Phys. Rev. Lett.*, 2017, **119**, 073204.

[78] D. J. McCarron, M. H. Steinecker, Y. Zhu, and D. DeMille, *Phys. Rev. Lett.*, 2018, **121**, 013202.

[79] H. J. Williams, L. Caldwell, N. J. Fitch, S. Truppe, J. Rodewald, E. A. Hinds, B. E. Sauer, and M. R. Tarbutt, *Phys. Rev. Lett.*, 2018, **120**, 163201.

[80] J. Riedel, S. Hoekstra, W. Jäger, J. J. Gilijamse, S. Y. T. van de Meerakker, and G. Meijer, *Eur. Phys. J. D*, 2011, **65**, 161–166.

[81] Y. Segev, M. Pitzer, M. Karpov, N. Akerman, J. Narevicius, and E. Narevicius, *arxiv*, 2019, p. 1902.04549.

[82] T. Takekoshi, B. M. Patterson, and R. J. Knize, *Phys. Rev. Lett.*, 1998, **81**, 5105–5108.

[83] K.-K. Ni, S. Ospelkaus, M. H. G. de Miranda, A. Pe'er, B. Neyenhuis, J. J. Zirbel, S. Kotochigova, P. S. Julienne, D. S. Jin, and J. Ye, *Science*, 2008, **322**, 231–235.

[84] M. T. Hummon, M. Yeo, B. K. Stuhl, A. L. Collopy, Y. Xia, and J. Ye, *Phys. Rev. Lett.*, 2013, **110**, 143001.

[85] J. Barry, D. McCarron, E. Norrgard, M. Steinecker, and D. DeMille, *Nature*, 2014, **512**, 286–289.

[86] C. E. Wieman, D. E. Pritchard, and D. J. Wineland, *Rev. Mod. Phys.*, 1999, **71**, S253–S262.

[87] E. Tsikata, W. C. Campbell, M. T. Hummon, H.-I. Lu, and J. M. Doyle, *New J. Phys.*, 2010, **12**, 065028.

[88] L. M. C. Janssen, A. van der Avoird, and G. C. Groenenboom, *Phys. Rev. Lett.*, 2013, **110**, 063201.

[89] T. E. Wall, *J. Phys. B*, 2016, **49**, 243001.

[90] H. Häffner, C. F. Roos, and R. Blatt, *Phys. Rep.*, 2008, **469**, 155–203.

[91] G. Herzberg, *The Spectra and Structures of simple free Radicals. An Introduction to Molecular Spectroscopy.*, Dover Publications, Inc., New York, 1971.

[92] S. van de Meerakker *Deceleration and electrostatic trapping of OH radicals* PhD thesis, 2006.

[93] P. Atkins and R. Friedman, *Molecular Quantum Mechanics*, Oxford University Press, Oxford, 2011.

[94] J. M. Brown and A. Carrington, *Rotational Spectroscopy of Diatomic Molecules*, Cambridge Molecular Science, Cambridge University Press, 2003.

[95] R. N. Zare, *Understanding spatial aspects in chemistry and physics.*, Wiley, New York, 1988.

[96] G. H. Dieke and H. M. Crosswhite, *J. Quant. Spectrosc. Radiat. Transfer*, 1962, **2**, 97–199.

[97] T. D. Hain, M. A. Weibel, K. M. Backstrand, and T. J. Curtiss, *J. Phys. Chem. A*, 1997, **101**, 7674–7683.

[98] W. Meerts, *Chem. Phys. Lett.*, 1977, **46**, 24–28.

[99] P. F. Bernath, *Spectra of Atoms and Molecules* , Oxford University Press, Oxford, 2005.

[100] P. Andresen, N. Aristov, V. Beuhausen, D. Häusler, and H. W. Lülf, *J. Chem. Phys.*, 1991, **95**, 5763.

[101] D. M. Sonnenfroh, R. G. Macdonald, and K. Liu, *J. Chem. Phys.*, 1991, **94**, 6508.

[102] M. Alagia, N. Balucani, P. Casavecchia, D. Stranges, and G. G. Volpi, *J. Chem. Phys.*, 1993, **98**, 8341.

[103] M. C. van Beek and J. J. ter Meulen, *Chem. Phys. Lett.*, 2001, **337**, 237–242.

[104] H. J. Lewandowski, E. R. Hudson, J. R. Bochinski, and J. Ye, *Chem. Phys. Lett.*, 2004, **395**, 53–57.

[105] D. Haas *Towards Hybrid Trapping of Cold Molecules and Cold Molecular Ions* PhD thesis, 2019.

[106] G. Scoles, *Atomic and Molecular Beam Methods* , Oxford University Press, Oxford, 1988.

[107] G. Bethlem, Hendrick L.and Meijer, *Int. Rev. Phys. Chem.*, 2003, **22**, 73–128.

[108] M. Collard, P. Kerwin, and A. Hodgson, *Chem. Phys. Lett.*, 1991, **179**, 422–428.

[109] C. McRaven, J. Alnis, B. Furneaux, and N. Shafer-Ray, *J. Phys. Chem. A*, 2003, **107**, 7138–7141.

[110] D. R. Yarkony, *J. Chem. Phys. Lett.*, 1992, **97**, 1838–1849.

[111] B. C. Sawyer, B. K. Stuhl, D. Wang, M. Yeo, and J. Ye, *Phys. Rev. Lett.*, 2008, **101**, 203203.

[112] C. J. Rennick, J. Lam, W. G. Doherty, and T. P. Softley, *Phys. Rev. Lett.*, 2014, **112**, 023002.

[113] L. M. García, F. Bartolomé, and J. B. Goedkoop, *Phys. Rev. Lett.*, 2000, **85**, 429.

[114] F.-J. Börgermann, C. Brombacher, and K. Üstüner, *Proceedings of IPAC2014*, 2014, pp. 1238–1240.

[115] R. Engel-Herbert and T. Hesjedal, *J. Appl. Phys.*, 2005, **97**, 074504.

[116] D. Haas, C. von Planta, T. Kierspel, D. Zhang, and S. Willitsch, *Comm. Phys.*, 2019, **2**, 1–7.

[117] M. Abramson, C. Audet, G. Couture, J. Dennis, Jr., S. Le Digabel, and C. Tribes, The NOMAD project: Software available at `https://www.gerad.ca/nomad/`, 2019.

[118] S. Le Digabel, *ACM Trans. Math. Software*, 2011, **37**, 44:1–44:15.

[119] A. H. Beck, *Handbook of Vacuum Physics*, Vol. 3, Pergamon Press LTD., New York, 1964.

[120] A. H. Beck, *Handbook of Vacuum Physics*, Vol. 2, Pergamon Press LTD., New York, 1965.

[121] Macor® machinable glass ceramic for industrial applications. Corning, 2012.

[122] Aluminum nitride material properties. Accuratus, 2013.

[123] Shapal ™ hi-m soft machinable aluminium nitride ceramic. GoodFellow, 2019.

[124] 96% alumina material properties. Accuratus, 2013.

[125] H. Miller, *IEEE Trans. El. Ins.*, 1993, **28**, 512–527.

[126] H. Miller, *IEEE Trans. El. Ins.*, 2015, **22**, 3641–3657.

[127] P. Eberle, A. D. Dörfler, C. von Planta, K. Ravi, and S. Willitsch, *Chem. Phys. Chem.*, 2016, **17**, 3769–3775.

[128] J. S. Brooke, P. F. Bernath, C. M. Western, C. Sneden, M. Afşar, G. Li, and I. E. Gordon, *J. Quant. Spectr. Rad. Transfer*, 2016, **168**, 142–157.

[129] I. I. Sobelman, *Atomic Spectra and Radiative Transitions*, Springer, Berlin, 1979.

[130] K. Wang and R. Reeber, *High Temp. Mat. Sci.*, 1996, **35**, 181–186.

[131] B. M. E. Ltd, Characteristics of ndfeb magnets, 2020.

[132] Stainless 316, 316l, 317, 317l. United performance materials, 2020.

[133] C. Billington and P. Starkey, Python wrapper around the spincore pulseblaster api using ctypes, 2013.

[134] A. Khayar and J. Bonamy, *J. Quant. Spectrosc. Radiat. Transfer*, 1982, **28**, 199–212.

[135] M. Lara, B. L. Lev, and J. L. Bohn, *Phys. Rev. A*, 2008, **78**, 033433.

[136] D. Reens, H. Wu, T. Langen, and J. Ye, *Phys. Rev. A*, 2017, **96**, 063420.

[137] B. K. Stuhl, M. T. Hummon, M. Yeo, G. Quéméner, J. L. Bohn, and J. Ye, *Nature*, 2012, **492**, 396–400.

[138] G. Quéméner and J. L. Bohn, *Phys. Rev. A*, 2013, **88**, 012706.

[139] N. Akerman, M. Karpov, Y. Segev, N. Bibelnik, J. Narevicius, and E. Narevicius, *Phys. Rev. Lett.*, 2017, **119**, 073204.

[140] J. M. Gray, J. A. Bossert, Y. Shyur, and H. J. Lewandowski, *Phys. Rev. A*, 2017, **96**, 023416.

[141] S. Willitsch, M. T. Bell, A. D. Gingell, and T. P. Softley, *Phys. Chem. Chem. Phys.*, 2008, **10**, 7200–7210.

[142] S. Willitsch, *Int. Rev. Phys. Chem.*, 2012, **31**, 175–199.

[143] S. Schiller and V. Korobov, *Phys. Rev. A*, 2005, **71**, 032505.

[144] K. Beloy, M. G. Kozlov, A. Borschevsky, A. W. Hauser, V. V. Flambaum, and P. Schwerdtfeger, *Phys. Rev. A*, 2011, **83**, 062514.

[145] M. S. Safronova, D. Budker, D. DeMille, D. F. J. Kimball, A. Derevianko, and C. W. Clark, *Rev. Mod. Phys.*, 2018, **90**, 025008.

[146] M. Drewsen, I. Jensen, J. Lindballe, N. Nissen, R. Martinussen, A. Mortensen, P. Staanum, and D. Voigt, *Int. J. Mass Spec.*, 2003, **229**, 83–91.

[147] D. Rösch, S. Willitsch, Y.-P. Chang, and J. Küpper, *J. Chem. Phys. Lett.*, 2014, **140**, 124202.

[148] W. Neuhauser, M. Hohenstatt, P. Toschek, and H. Dehmelt, *Phys. Rev. Lett.*, 1978, **41**, 233–236.

[149] D. J. Larson, J. C. Bergquist, J. J. Bollinger, W. M. Itano, and D. J. Wineland, *Phys. Rev. Lett.*, 1986, **57**, 70–73.

[150] X. Tong, A. H. Winney, and S. Willitsch, *Phys. Rev. Lett.*, 2010, **105**, 143001.

[151] W. Paul, H. P. Reinhard, and U. von Zahn, *Zeitschrift für Physik*, 1958, **152**, 143–182.

[152] D. J. Griffiths, *Introduction to Electrodynamics*, Vol. 4, Oxford University Press, Pearson, 2013.

[153] C. J. Foot, *Atomic Physics*, Oxford University Press, Oxford, 2005.

[154] M. Drewsen and A. Brøner, *Phys. Rev. A*, 2000, **62**, 045401–1–045401–4.

[155] J. M. Heinrich *A Be^+ Ion Trap for H_2^+ Spectroscopy* PhD thesis, 2018.

[156] D. J. Berkeland, J. D. Miller, J. C. Bergquist, W. M. Itano, and D. J. Wineland, *J. Appl. Phys.*, 1998, **83**, 5025–5033.

[157] D. Gerlich, *Inhomogeneous RF Fields: A Versatile Tool for the Study of Processes with Slow Ions*, 2007.

[158] V. N. Major, F. G. amd Gheorghe and G. Werth, *Charged Particle Traps*, 2005.

[159] A. Mokhberi *Scalable Microchip Ion Traps and Guides for Cold Molecular Ions* PhD thesis, 2016.

[160] Alfavakuo e.u. www.alfavakuo.eu.

[161] N. Kjærgaard, L. Hornekaer, A. Thommesen, Z. Videsen, and M. Drewsen, *Appl. Phys. B*, 2000, **71**, 207–210.

[162] H. J. Metcalf and P. van der Straten, *Laser Cooling and Trapping*, 1999.

[163] D. J. Wineland, R. E. Drullinger, and F. L. Walls, *Phys. Rev. Lett.*, 1978, **40**, 1639–1642.

[164] S. Stenholm, *Rev. Mod. Phys.*, 1986, **58**, 699–739.

[165] M. S. Safronova and U. I. Safronova, *Phys. Rev. A*, 2011, **83**, 012503.

[166] E. L. Pollock and J. P. Hansen, *Phys. Rev. A*, 1973, **8**, 3110–3122.

[167] J. P. Schiffer, *Phys. Rev. Lett.*, 2002, **88**, 205003.

[168] Luca^{EM} R 604. Andor Technology, 2020.

[169] T. Ray, S. Jyothi, N. Bhargava Ram, and S. A. Rangwala, *App. Phys. B*, 2014, **114**, 267–273.

[170] J. Kleinert, C. Haimberger, P. J. Zabawa, and N. P. Bigelow, *Phys. Rev. Lett.*, 2007, **99**, 143002.

[171] M. Schwarz, O. O. Versolato, A. Windberger, F. R. Brunner, T. Ballance, S. N. Eberle, J. Ullrich, P. O. Schmidt, A. K. Hansen, A. D. Gingell, M. Drewsen, and J. R. C. López-Urrutia, *Rev. Sci. Instr.*, 2012, **83**, 083115.

[172] L. Schmöger, O. O. Versolato, M. Schwarz, M. Kohnen, A. Windberger, B. Piest, S. Feuchtenbeiner, J. Pedregosa-Gutierrez, T. Leopold, P. Micke, A. K. Hansen, T. M. Baumann, M. Drewsen, J. Ullrich, P. O. Schmidt, and J. R. C. López-Urrutia, *Science*, 2015, **347**, 1233–1236.

[173] A. K. Hansen, O. O. Versolato, L. Kłosowski, S. B. Kristensen, A. Gingell, M. Schwarz, A. Windberger, J. Ullrich, J. R. C. López-Urrutia, and M. Drewsen, *Nature*, 2014, **508**, 76–79.

[174] Comsol multiphysics© v. 5.3 www.comsol.com.

[175] D. R. Denison, *J. Vac. Sci. Tech.*, 1971, **8**, 266–269.

[176] R. M. Jones, D. Gerlich, and S. L. Anderson, *Rev. Sci. Instr.*, 1997, **68**, 3357–3362.

[177] L. S. Brown and G. Gabrielse, *Rev. Mod. Phys.*, 1986, **58**, 233–311.

[178] K. Koo, J. Sudbery, D. M. Segal, and R. C. Thompson, *Phys. Rev. A*, 2004, **69**, 043402.

[179] J. F. Goodwin, G. Stutter, R. C. Thompson, and D. M. Segal, *Phys. Rev. Lett.*, 2016, **116**, 143002.

[180] E. Paradis, S. Zigo, K. Z. Hu, and G. Raithel, *Phys. Rev. A*, 2012, **86**, 023416.

[181] Z. Andelkovic, R. Cazan, W. Nörtershäuser, S. Bharadia, D. M. Segal, R. C. Thompson, R. Jöhren, J. Vollbrecht, V. Hannen, and M. Vogel, *Phys. Rev. A*, 2013, **87**, 033423.

[182] K. Mølmer, Y. Castin, and J. Dalibard, *J. Opt. Soc. Am. B*, 1993, **10**, 524–538.

[183] B. E. A. Saleh and M. C. Teich, *Fundamentals of Photonics*, Vol. 2, Wiley, 2007.

[184] D. Reiß, A. Lindner, and R. Blatt, *Phys. Rev. A*, 1996, **54**, 5133–5140.

[185] I. J. Rouse *A miniaturised hybrid ion-atom chip trap and the non-equilibrium statistical mechanics of trapped ions* PhD thesis, 2018.

[186] C. von Planta, Numerical simulation of a shuttling rubidium atom cloud in a magneto-optical trap with optimized kinetic energy resolution, 2015.

[187] I. W. Smith, *Ann. Rev. Astronomy and Astrophysics*, 2011, **49**, 29–66.

[188] D. Zhang and S. Willitsch in *Cold Chemistry: Molecular Scattering and Reactivity Near Absolute Zero;* The Royal Society of Chemistry, 2018; pp. 496–536.

Claudio von Planta

19 December 1990
unmarried

Birkenstrasse 3
Allschwil, 4123

+4178 711 42 84

claudio@vplanta.ch

www.linkedin.com/in/claudio-von-planta-310159164

Computer Skills —

Python

Keras

TensorFlow

C/C++

Fortran

LabView

MatLab

Mathematica

Linux

OS X

Windows

LaTeX

Microsoft Word

Microsoft Excel

Microsoft Powerpoint

OpenCL ⋆ 3.0 Solidworks CAD⋆2.0
Comsol Multiphysics ⋆5.0
Inkscape⋆4.0 Bash Shell⋆3.0

(*)[The skill scale is from 0 (Fundamental Awareness) to 6 (Expert).]

Education

since 2015 — PhD in Chemistry — University of Basel
Cryogenic molecular ion-neutral hybridtrap

2013-2015 — M.Sc. in Chemistry — University of Basel
Master thesis: *Numerical Simulation of a Shuttling Rubidium Atom Cloud in a Magneto-Optical Trap with Optimized Kinetic Energy Resolution.*

2010-2013 — B.Sc. in Chemistry — University of Basel

2006-2010 — Matura — Gymnasium Kirschgarten, Basel
Specializing in biology/chemistry.

Experience

since 2015 — Research Assistant — University of Basel
Department of Chemistry, Group of Prof. Dr. Stefan Willitsch.
- Software development for data analysis
(Python, Numpy, Pandas, Scikit-learn, Mathematica).
- Software development for data acquisition from and automation of experimental apparatus
(Python, QT5, LabView, Cython, C/C++, Ctypes).
- Design, simulation, optimization and assembly of cryogenic experimental apparatus.
(COMSOL, MatLab, SolidWorks, Fortran, high voltage, radio-frequency electronics, ultrahigh vacuum, cryogenics, laser technology and optics).
- Project planning, scientific writing, experimental atomic- and molecular physics.

2015-2019 — Teaching Assistant — University of Basel
Tutor and substitute lecturer in: Physical Chemistry II: Introduction to Quantum Mechanics and Physical Chemistry III: Molecular Quantum Mechanics.

Certificates

2020 — Deep Learning Specialization. (Coursera, deeplearning.ai)
2020 — Sequence Models. (Coursera, deeplearning.ai)
2019 — Structuring Machine Learning Projects. (Coursera, deeplearning.ai)
2019 — Improving Deep Neural Networks: Hyperparameter tuning, Regularization and Optimization. (Coursera, deeplearning.ai)
2019 — Neural Networks and Deep Learning. (Coursera, deeplearning.ai)

Peer-reviewed Publications

2019 — D. Haas*, C. von Planta* et al., *Long-term trapping of Stark-decelerated molecules*, Communications Physics, 2.
(* These authors contributed equally)

2019 — S. Thamboo, A. Najer, A. Belluati, C. von Planta et al., *Mimicking Cellular Signaling Pathways within Synthetic Multicompartment Vesicles with Triggered Enzyme Activity and Induced Ion Channel Recruitment*, Advanced Functional Materials, 29.

2016 — P. Eberle, A.D. Dörfler, C. von Planta et al., *A Dynamic Ion–Atom Hybrid Trap for High-Resolution Cold-Collision Studies*, ChemPhysChem, 17.

2015 — P. Eberle, A.D. Dörfler, C. von Planta et al., *Ion-Atom and Ion-Molecule Hybrid Systems: Ion-Neutral Chemistry at Ultralow Energies*, Journal of Physics: Conference Series, 635.

Languages

German

English

French

(*)[The skill scale is from 0 (Fundamental Awareness) to 6 (Expert).]

Conference Contributions

2019	DMC 27, Big Sky (USA), Dynamics of Molecular Collisions.
2018	MOLEC 2018, Dinard (FR), European Conference on the Dynamics of Molecular Systems.
2017	SCS Fall meeting, Bern (CH), Fall Meeting of the Swiss Chemical Society.
2016	MolecXXI, Toledo (ESP), European Conference on the Dynamics of Molecular Systems.
2016	CoCo IRTG 2027, Mittelwihr (FR), Summer School on Cold Controlled Ensembles in Physics and Chemistry.

Hobbies

- Powerlifting, Schwerathletik Beider Basel.
- Snowboarding (J&S teacher).